University of Glasgow

MOVPE Growth for GaAs-Based Photonic Crystal Surface Emitting Lasers

Adam F. McKenzie

Submitted in fulfilment of the requirements for the

Degree of Doctor on Philosophy

James Watt School of Engineering

College of Science and Engineering

University of Glasgow

November 2022

Author's Declaration

"I declare that, except where explicit reference is made to the contribution of others, that this thesis is the result of my own work and has not been submitted for any other degree at the University of Glasgow or any other institution."

Name: _____

Signature: _____

The design and testing of devices discussed in Chapter 3 was performed by Dr Ben King with fabrication carried out by Dr Katie Hill, both of the University of Glasgow. Dr Neil Gerrard assisted in the development of the epitaxial regrowth process.

The substrates discussed in Chapter 4 where patterned and processed by Aye Mon Kyaw and Dr Katie Hill, both of the University of Glasgow. Dr Sam McFadzean and Dr Donald MacLaren assisted in the collection of the STEM images.

The samples discussed in Chapter 5 were processed by Dr Katie Hill, and photoluminescence and optical profilometry measurements carried out by Xingyu Zhao, both of the University of Glasgow.

The work in this thesis has been published in the journal articles listed on page v.

Abstract

Photonic crystal surface emitting lasers (PCSELs) have emerged recently as class of laser diode that are of great commercial interest, offering high-power, single-mode surface emission across a wide range of wavelengths. The optical and electrical characteristics of PCSELs are intrinsically linked to the nanoscale structure of the two-dimensional photonic crystal (PC) grating layer that is embedded within the device structure by metalorganic vapour phase epitaxy (MOVPE) regrowth. In this regard, an understanding of, and the ability to influence, the formation of crystallographic voids within the PC during epitaxial regrowth is one of the key aspects for achieving optimised designs and device performance.

This thesis presents a number of studies related to the application of MOVPE in the fabrication of GaAs-based PCSELs, with a particular focus on epitaxial regrowth and the engineering of voids. The mechanism of void formation and the factors dictating the extent of grating infill are investigated by electron microscopy-based structural analysis of regrown PC structures and correlated with device results.

Initially, AlAs/GaAs PCSELs are presented for which the morphology of the initial PC grating pits has been modified by controlling the degree of mass-transport of material during the pre-growth temperature ramp within the MOVPE reactor. It is shown that void formation is the result of low adatom surface mobility and self-shadowing effects which drive rapid lateral growth of the upper pit surface. The growth kinetics associated with the crystal planes of the underlying grating pits are shown to greatly impact the size and shape of the voids, with vastly different geometries observed in each of the devices.

Following this, the role of adatom mobility in driving grating infill is demonstrated in PC structures for which the composition of the regrowth material is varied. It is shown that void formation is favoured when aluminium-containing layers are used, for which the inherent adatom mobility is low, and that complete grating infill is promoted in the case of higher-mobility GaAs. Analysis of the three-dimensional void shape in AlAs- and AlGaAs-regrown structures reveals that natural

asymmetries emerge in the shape of voids even when symmetric, circular grating pits are used, owing to the differing polarities and growth kinetics of high-Miller index crystal planes in III-V materials. It is shown that the in-plane asymmetry of void shape can be greatly enhance by the use of $(311)B$ orientated substrates, and that voids in these PCs display an additional out-of-plane asymmetry compared to those in the conventional (100) orientated structures.

In addition to the PC regrowth studies described above, an initial investigation into the use selective area growth (SAG) as a method for realising multicolour PCSEL arrays is presented. It is shown that the growth rate enhancement and wavelength tuning associated with SAG is effective for InGaAs/GaAs multi-quantum well structures deposited in masked growth windows with dimensions up to 300 x 300 μm^2. For selected features, it is shown that large areas of material with uniform emission wavelengths up to 100 x 100 μm^2 in size can be achieved, being appropriate for the fabrication of monolithically integrated devices in the future.

Acknowledgements

First and foremost, I need to thank my supervisor, Professor Richard Hogg, for taking me on this mad journey and for being a good friend, critic, and mentor throughout. I'll never forget everything you've done for me in these past five years.

Thank you to everyone in the Photonic Devices and Systems group, past and present, who have helped and supported me along the way, especially Dave, Ben, Zijun, Katie, Aye, Daehyun, Xingyu, and Adam. And thanks to the "World's Leading Expert in the Physics of Green", Richard Taylor, for being a good mate; and for San Francisco.

My deepest thanks go to Dr Donald MacLaren for his steadying and reassuring presence throughout the mad times, and for putting up with me for another four-and-a-bit years. And thanks too to Billy, Colin, and Sam for their assistance and patience in developing my skills as a microscopist.

To the "Epi Dream Team", without whom I wouldn't be half to grower I am today, and to whom I will be forever indebted. To Neil, Jono, and Matt, for teaching me everything I know about MOCVD and characterisation of III-Vs, and to the "OG Operator", Marie, for your constant belief (and all the biscuits), thank you.

To everyone at Sivers Photonics who helped me along the way, I will be eternally grateful: to Andy for giving me a chance as a random undergrad all those years ago; to Neil and Euan for taking the gamble that I was a decent engineer; to Sharon for championing me throughout; to Elissa, Kirsty, Kaitlyn, Marianne, Martin, Olek, and Paul for all the free therapy; and to Graeme, for understanding and for having my back when things were difficult.

None of this would have been possible without the support of the Royal Commission for the Exhibition of 1851. Thank you to everyone who made the decision to fund me, and for giving me opportunities I never dreamed I would have.

Finally, to my family, for your unwavering and unconditional support… "thank you" just doesn't feel like enough; I wouldn't be here without you.

Research Outcomes

Journal Articles:

[1] Z. Bian, K. J. Rae, **A. F. McKenzie**, B. C. King, N. Babazadeh, G. Li, J. R. Orchard, N. D. Gerrard, S. Thoms, D. A. MacLaren, R. J. E. Taylor, D. T. D. Childs, and R. A. Hogg, "1.5 μm photonic crystal surface emitting laser", *IEEE Photon. Technol. Lett.*, **32** (24), 1531-1534 (2020)

[2] B. C. King, K. J. Rae, **A. F. McKenzie**, A. Boldin, D-H. Kim, N. D. Gerrard, G. Li, K. Nishi, K. Takemasa, M. Sugawara, R. J. E. Taylor, D. T. D. Childs, and R. A. Hogg, "Coherent power scaling in photonic crystal surface emitting laser arrays", *AIP* Advances, **11**, 015017 (2021)

[3] **A. F. McKenzie**, B. C. King, K. J. Rae, S. Thoms, N. D. Gerrard, J. R. Orchard, K. Nishi, K. Takemasa, M. Sugawara, R. J. E. Taylor, D. T. D. Childs, D. A. MacLaren, and R. A Hogg, "Void engineering in epitaxially regrown GaAs-based photonic crystal surface emitting lasers by grating profile design", *Appl. Phys. Lett.*, **118**, 021109 (2021)

[4] Z. Bian, K. J. Rae, B. C. King, D-H. Kim, G. Li, S. Thoms, D. T. D. Childs, N. D. Gerrard, N. Babazadeh, P. Reynolds, J. Grant, **A. F. McKenzie**, J. R. Orchard, R. J. E. Taylor, and R. A. Hogg, "Comparative analysis of void-containing and all-semiconductor 1.5 μm InP-based photonic crystal surface emitting laser diodes", *AIP Advances*, **11**, 065315 (2021)

[5] **A. F. McKenzie**, A. M. Kyaw, N. D. Gerrard, D. A. MacLaren, and R. A. Hogg, "Kinetic influences on void formation in epitaxially regrown GaAs-based PCSELs", *J. Cryst. Growth*, **602**, 126969 (2023)

[6] X. Zhao, **A. F. McKenzie**, C. W. Munro, K. J. Hill, D-H. Kim, S. L. Bayliss, N. D. Gerrard, D. A. MacLaren, and R. A. Hogg, "Large-area 2D selective area growth for photonic-crystal surface emitting lasers", *J. Cryst. Growth*, **603,** 127036 (2023)

Conference Presentations:

[1] **A. F. McKenzie**, J. R. Orchard, N. D. Gerrard, O. Kowalski, A. McKee, Z. Bian, R. J. E. Taylor, D. T. D. Childs, D. A. MacLaren, and R. A. Hogg, "Developments in InP-Based Epitaxial Regrowth", *UK Semiconductor Conference*, B-O-13, Sheffield, UK, July 2019 (Oral Presentation)

[2] **A. F. McKenzie**, B. C, King, Z. Bian, K. J. Rae, G. Li, N. D. Gerrard, J. R. Orchard, R. J. E. Taylor, D. T. D. Childs, D. A. MacLaren, and R. A. Hogg, "Advances in regrown all-semiconductor photonic crystal surface-emitting lasers", *Photonics West Conference*, 11301-32, San Francisco, CA, February 2020 (Oral Presentation)

[3] B. C. King, **A. F. McKenzie**, A. Boldin, D-H. Kim, R. J. E. Taylor, K. J. Rae, N. Babazadeh, P. Ivanov, J. R. Orchard, N. D. Gerrard, D. T. D. Childs, and R. A. Hogg, "Properties of laterally coupled photonic crystal surface-emitting laser two-dimensional arrays", *Photonics West Conference*, 11301-31, San Francisco, CA, February 2020 (Oral Presentation)

[4] B. C. King, K. J. Rae, **A. F. McKenzie**, A. Boldin, D-H. Kim, N. D. Gerrard, G. Li, K. Nishi, K. Takemasa, M. Sugawara, R. J. E. Taylor, D. T. D. Childs, and R. A. Hogg, "Power scaling in photonic crystal surface emitting laser arrays", *Solid State Devices and Materials 2020 Conference*, E-1-01, Virtual Conference, Japan, September 2020 (Oral Presentation)

[5] Z. Bian, K. J. Rae, **A. F. McKenzie**, B. C. King, N. Babazadeh, G. Li, J. R. Orchard, N. D. Gerrard, S. Thoms, D. A. MacLaren, R. J. E. Taylor, D. T. D. Childs, and R. A. Hogg, "1.5 μm photonic crystal surface emitting laser diode", *Solid State Devices and Materials 2020 Conference*, E-1-02, Virtual Conference, Japan, September 2020 (Oral Presentation)

[6] **A. F. McKenzie**, B. C. King, K. J. Rae, N. D. Gerrard, J. R. Orchard, K. Nishi, K. Takemasa, M. Sugawara, R. J. E. Taylor, D. T. D. Childs, D. A. MacLaren, and R. A. Hogg, "Void engineering in epitaxially regrown photonic crystal surface emitting lasers", *Solid State Devices and Materials 2020 Conference*, E-2-03, Virtual Conference, Japan, September 2020 (Oral Presentation)

[7] C. Hill, J. R. Orchard, I. Javed, C. W. Munro, D-H. Kim, Z. Bian, **A. F. McKenzie**, N. D. Gerrard, K. J. Rae, P. Ivanov, R. J. E. Taylor, R. A. Hogg, and D. T. D. Childs, "Monolithic all-semiconductor PCSELs emitting at 1.3 μm", *27th International Semiconductor Laser Conference*, WP3.4, Potsdam, Germany, October 2021 (Oral Presentation)

[8] **A. F. McKenzie**, X. Zhao, S. L. Bayliss, K. J. Hill, D-H. Kim, and R. A. Hogg, "Large-Area 2D Selective Area Growth for Photonic Crystal Surface Emitting Lasers", *20th International Conference on Metalorganic Vapour Phase Epitaxy*, Th B3.2, Fellbach, Germany, July 2022 (Oral Presentation)

[9] **A. F. McKenzie**, A. M. Kyaw, N. D. Gerrard, D. A. MacLaren, and R. A. Hogg, "Kinetic Influences on Void Formation in Epitaxially Regrown GaAs-Based PCSELs", *20th International Conference on Metalorganic Vapour Phase Epitaxy*, P38, Fellbach, Germany, July 2022 (Poster Presentation)

[10] **A. F. McKenzie**, A. M. Kyaw, B. C. King, N. D. Gerrard, K. Nishi, K. Takemasa, M. Sugawara, C. H. Hill, D. T. D. Childs, R. J. E. Taylor, D. A. MacLaren, and R. A. Hogg, "Development of Epitaxial Regrowth for GaAs-Based Quantum Dot PCSELs", *Solid State Devices and Materials 2022 Conference*, A-6-08, Chiba, Japan, September 2022 (Oral Presentation)

[11] Z. Bian, X. Zhao, K. J. Rae, A. M. Kyaw, **A. F. McKenzie**, B. C. King, J. Liu, S. Thoms, P. Reynolds, J. R. Orchard, C. H. Hill, C. W. Munro, P. Ivanov, D. T. D. Childs, R. J. E. Taylor, and R. A. Hogg, "Resonator Embedded Photonic Crystal Surface Emitting Lasers", *28th International Semiconductor Laser Conference*, MB-06, Matsue, Japan, October 2022 (Oral Presentation)

[12] A. M. Kyaw, B. C. King, **A. F. McKenzie**, N. D. Gerrard, Z. Bian, D-H. Kim, J. Liu, X. Zhao, K. Nishi, K. Takemasa, M. Sugawara, D. T. D. Childs, C. Hill, R. J. E. Taylor, and R. A. Hogg, "Epitaxially Regrown Quantum Dot Photonic Crystal Surface Emitting Lasers", *28th International Semiconductor Laser Conference*, WA-05, Matsue, Japan, October 2022 (Oral Presentation)

Awards and Grants:

Industrial Fellowship (ERA Foundation Fellowship) – Royal Commission for the Exhibition of 1851 & The ERA Foundation (2018)

PhD Equipment Access Grant – Henry Royce Institute (2019)

PGR Mobility Grant – University of Glasgow (2020)

IET Postgraduate Prize – Institution of Engineering and Technology (IET) (2020)

IET Travel Award – Institution of Engineering and Technology (IET) (2022)

Table of Contents

Chapter 1 |

Introduction

In the past two decades, the photonic crystal surface emitting laser (PCSEL) has emerged as new class of laser diode that is of great research and commercial interest owing to an attractive combination of device characteristics that are not typically available for contemporary edge- or surface-emitting devices [1]. Since the first report of an electrically injected device in InP in 1999 [2], there has been a proliferation of publications reporting devices that display high-power, single-mode surface emission [3], high-optical beam quality and extremely low far-field divergence [4], and the ability to control both the far-field beam shape [5] and polarisation [6]. In addition to this, the flexibility of design has allowed for the fabrication of devices in many materials systems including GaN [7], GaAs [3-5,8], InP [2,5,19], and GaSb [10]. As a result, the wavelength range accessible to PCSELs extends from 400 – 9000 nm [11,12], thus making them promising candidates for use in applications ranging from tele- and data-coms, to additive manufacturing, automotive LIDAR, and chemical spectroscopy and sensing [1].

Lasing action in PCSELs is realised through the incorporation of a photonic crystal (PC) grating layer within the epitaxial structure of the device, adjacent to the active region. The PC grating introduces a two-dimensional (2D), periodic variation in refractive index based on a repeated unit cell that is composed of a matrix material with index n_1 into which a region of material, or PC "atom", with index n_2 is introduced [13]. Light which couples to the grating undergoes Bragg scattering and is coherently scattered within the plane of the PC layer, forming a 2D resonant cavity that supports large-area laser oscillation [14]. The feedback and emission planes in a PCSEL are decoupled, with surface emission being produced by the second-order scattering of light out-of-plane across the entire surface of the device, offering the potential for area-scalable output powers without the degradation of optical mode quality [15].

The optical and electrical characteristics of PCSELs are intrinsically related to the nanoscale structure of the PC layer. Control over the fill factor of the PC atom is crucial in maximising the coupling coefficients of the grating and reducing in-plane losses, which is necessary for achieving low threshold current densities [16]. In addition, the shape of the atom [17,18], particularly it's asymmetry with respect to the axes of the PC, and the thickness of the PC layer [19] have been shown to be critical in maximising the output power of the devices by reducing the confinement of light within the layer and minimising destructive interference of the light scattered vertically out-of-plane. Recently, optimised unit cell design has allowed for room temperature continuous-wave operation at multi-Watt output powers for GaAs-based devices with emission areas greater than 500 x 500 μm^2 [20].

Whilst originally realised through wafer bonding [2,13,15], the rapid improvements in the performance of PCSELs have been driven, in part, by the development of an all-metalorganic vapour phase epitaxy (MOVPE)-based approach, which has become the preferred method for fabricating high-performance devices through a two-stage growth process [1,3,4,7,8,9,20]. In the first stage, the base epitaxial material including the lower *n*-doped cladding layers, the active region of the device, and the *p*-doped matrix layer of the PC grating is grown as for conventional devices. In subsequent processing steps, involving electron beam lithography and reactive ion etching, the grating layer is patterned with an array of etched pits that define the atoms of the PC. Then, in the second growth stage known as epitaxial regrowth, the etched pits are infilled and planarised, and the upper *p*-doped layers of the device structure deposited.

MOVPE regrowth allows for an additional degree of freedom in the design of PCSELs through the ability to realise both all-semiconductor [21,22] and void-containing PC structures [1,3,4,7,8,9,20]. In all-semiconductor PCs, the grating pits entirely infill during regrowth and the refractive index contrast is between two semiconductor materials. In this case, the characteristics of the device are determined by the geometry of the unit cell as it was designed and fabricated. In void-containing structures, on the other hand, the refractive index is produced by crystallographic air-voids that are encapsulated within the semiconductor matrix during regrowth. In this PC system, which is by far the most widely reported in the literature, the device characteristics are dominated by the size and shape of the voids rather than those of the underlying grating pits, which now essentially act as a seeding layer for void encapsulation.

The challenge facing the design of an optimised regrowth process for PCSELs lies in understanding the kinetic influences affecting growth within the grating pits, and the ability to control the extent of pit infilling in order to realise an optimised PC geometry. Analysis of the regrowth process is achieved by direct observation of the buried PC layer by electron microscopy, allowing the relationship between growth conditions, adatom diffusion, crystal plane kinetics, and void shape to be inferred [22-25]. In this regard, the increased resolution and elemental sensitivity associated with scanning transmission electron microscopy (STEM) has the potential to reveal information that was previously overlooked or missing in conventional scanning (SEM) or transmission electron microscopy (TEM)-based approach, greatly enhancing our understanding of the mechanisms of regrowth and void formation [26].

To date, there have been few reports in the PCSEL literature that have explicitly studied the epitaxial regrowth process, and our current understanding of the extent to which void engineering can be achieved in different materials systems is limited. Whilst studies of GaAs/GaInP [22] and InP [23] PC structures have investigated the role of regrowth conditions and adatom mobility in tuning the extent of pit infilling, no similar reports have been published for the AlGaAs/GaAs system. A detailed study of the regrowth process which explores the relationship between growth kinetics and PC geometry for this material system is therefore timely.

1.1. In This Thesis

The focus of this thesis is the role of MOVPE-based epitaxial growth in the development of GaAs-based PCSELs. Attention is given to both epitaxial growth processes required for device fabrication: regrowth of the PC grating and the engineering of voids in these structures, and the growth of multi-quantum well (MQW) active elements by selective area growth (SAG). Chapter 2 provides the background theory behind key concepts including MOVPE growth technology and growth on non-planar substrates, design considerations for optimum PC geometries and previous work regarding epitaxial regrowth of PCSELs, and the use of electron microscope-based techniques in studying buried structures in semiconductor devices.

Chapter 3 presents a correlative structural and parametric investigation of two PCSELs containing different void geometries. The devices are nominally identical in terms of epitaxial structure, PC grating etch, and post-regrowth fabrication, and differ only in the pre-growth temperature ramp time used at the start of the regrowth process. Through cross-sectional STEM imaging of the regrown PC layer, it is shown that the choice of ramp time is crucial in controlling the extent of mass-transport in the PC pits, an important factor in retaining the optimal grating design. Use of a short, three-minute ramp time allows for the retention of the as-etched $\{111\}$ sidewall pit profile, whilst a longer six-minute ramp leads to significant diffusion-related surface restructuring within the grating pits, greatly changing their crystallography through the introduction of high-Miller index $\{311\}$ sidewalls planes. Analysis of grating infill dynamics is enabled by use of an AlAs/GaAs superlattice structure during regrowth, which provides time-resolved snapshots revealing the evolution of the growth front. It is shown that the voids are encapsulated due to lateral growth of the upper pit

surfaces across the pit opening, and that this lateral growth is driven primarily by low adatom surface mobility and exacerbated by self-shadowing effects. The size and shape of the voids in each device is dictated by the underlying pit geometry, with $\{111\}$ sidewall planes resulting in much larger voids compared to the high-growth rate $\{311\}$. The LIV characteristics of the devices are analysed in terms of the observed void geometry and their expected coupling strengths, with the lager voids resulting in a reduced threshold current density and higher output power, in line with stronger coupling.

Chapter 4 details regrowth studies that further explore different influences on void formation in the (Al)(Ga)As/GaAs PC system. Initially, the effect of adatom surface mobility is investigated by varying the composition of the grating infill layer across three test structures on (100) orientated substrates. It is shown that complete infilling of the pits can be achieved using GaAs, whilst void formation is favoured where low-surface mobility aluminium-containing AlAs and AlGaAs are used. In the case of AlGaAs, the voids are much smaller in terms of height and diameter owing to the presence of higher-mobility gallium, which promotes greater diffusion of material into the pits. Through cross-sectional STEM analysis along both axes of the PC, it is shown that voids display an in-plane asymmetry in their shape which arises naturally when circular grating pits are used, and that the degree of asymmetry is greater for AlAs-regrown material because of lower adatom mobility. This asymmetry is attributed to the different crystal plane growth kinetics associated with the *A*- and *B*-type polarities of high-Miller index crystal planes in III-V materials. Following this, void size tuning is explored for three AlGaAs-regrown samples in which the grating pit diameter and depth are varied. Trends in the measured void dimensions are used

to predict initial grating designs required to achieve voids with optimum geometries for maximum coupling. Finally, it is shown that the in-plane asymmetry in void shape can be greatly enhanced, and an additional out-of-plane asymmetry achieved, using $\{311\}B$ orientated substrates which have a reduced crystal symmetry and more complex growth dynamics compared with the conventional (100) surface.

Lastly, Chapter 5 describes an initial investigation into the use of SAG as a technique for achieving monolithically integrated, multicolour PCSEL arrays through the controlled on-wafer variation of MQW emission wavelength. In this study, an InGaAs/GaAs MQW structure is deposited on a wafer patterned with an array of large, two-dimensional, masked growth windows with dimension up to 300 x 300 μm^2, chosen to reflect the unique device geometry associated with PCSELs. Through analysis of the QW emission wavelength and thickness at the centre point of each of the SAG windows, it is shown that the enhanced growth rate associated with SAG is effective in these very large features. A wavelength tuning range of up to 86 nm can be achieved across all sites, depending on the width of the dielectric mask used. Additionally, by extending the initial point analysis to the entirety of the growth window for selected features, it shown that large areas of material with isotropic emission wavelengths varying, within ± 2 nm, are obtained at the centre of the growth windows. In some cases, the dimensions of these regions are shown to be on the order of 100 x 100 μm^2, the minimum area required for the fabrication of functioning devices, indicating the suitability of SAG in the future development of PCSEL arrays.

1.2. References

[1] K. Ishizaki, M. De Zoysa, and S. Noda, “Progress in photonic-crystal surface-emitting lasers”, Photonics, 6, 96 (2019)

[2] M. Imada, S. Noda, A. Chutinan, M. Murata, and G. Sasaki, “Semiconductor lasers with one- and two-dimensional air/semiconductor gratings embedded by wafer fusion technique”, *IEEE J. Select. Topics Quant. Electron*, **5**(3), 158 (1999)

[3] K. Hirose, Y. Liang, Y. Kurosaka, A. Watanae, T. Sugiyama, and S. Noda, “Watt-class high-power, high-bem-quality photonic-crystal lasers”, Nature Photon., 8, 406-411 (2014)

[4] R. Sakata, K. Ishizaki, M. DeZoysa, S. Fukuhara, T. Inoue, Y. Tanaka, K. Iwata, R. Hatsuda, M. Yoshida, J. Gelleta, and S. Noda, “Dually modulated photonic crystals enabling high-power high-beam-quality two-dimensional beam scanning lasers”, *Nature Commun.*, **11**, 3487 (2020)

[5] E. Miyai, K. Sakai, T. Okano, W. Kunishi, D. Ohmishi, and S. Noda, “Lasers producing tailored beams”, *Nature*, **44**, 946 (2006)

[6] S. Noda, M. Yokoyama, M. Imada, A. Chutinan, M. Mochizuki, “Polarization mode control of two-dimensional photonic crystal laser by unit cell structure design”, *Science*, **293**, 1123 (2001)

[7] K. Emoto, T. Koizumi, M. Hirose, M. Jutori, T. Inoue, K. Ishizaki, M. De Zoysa, H. Togwa, and S. Noda, “Wide-bandgap GaN-based watt-class photonic-crystal lasers”, *Commun. Mater.*, **3**, 72 (2022)

[8] B. C. King, K. J. Rae, A. F. McKenzie, A. Boldin, D-H. Kim, N. D. Gerrard, G. Li, K. Nishi, K. Takemasa, M. Sugawara, R. J. E. Taylor, D. T. D. Childs, and R. A. Hogg, "Coherent power scaling in photonic crystal surface emitting laser arrays", AIP Advances, 11, 015017 (2021)

[9] Z. Bian, K. J. Rae, A. F. McKenzie, B. C. King, N. Babazadeh, G. Li, J. R. Orchard, N. D. Gerrard, S. Thoms, D. A. MacLaren, R. J. E. Taylor, D. T. D. Childs, and R. A. Hogg, "1.5 μm epitaxially regrown photonic crystak surface emitting laser diode", IEEE Photon. Technol. Lett., 22(24), 1531 (2020)

[10] Y-H. Huang, Z-X. Yang, S-L. Cheng, C-H. Lin, G. Lin, K-W. Sun, and C-P. Lee, "Effect of hole shift on threshold characteristics of GaSb-based double-hole photonic-crystal surface-emitting lasers", Micromachines, 12, 468 (2021)

[11] T-C. Lu, S-W. Chen. T-T. Kao, and T-W. Liu, "Characteristics of GaN-based photonic crystal surface emitting lasers", Appl. Phys. Lett., 93, 111111, (2008)

[12] Z. Wang, Y. Liang, B. Meng, Y-T. Sun, G. Omanakuttan, E. Gini, M. Beck, I. Sergachev, S. Lourdudoss,J. Faist, and G. Scalari, "Large area photonic crystal quantum cascade laser with 5 W surface emitting power", *Optics Express*, **27**(16), 365213 (2019)

[13] M. Imada, S. Noda, A. Chutinan, T. tokuda, M. Murata, and G. Sasaki, "Coherent two-dimensional lasing action in surface-emitting laser with triangular-lattice photonic crystal structure", *Appl. Phys. Lett.*, **75**, 316 (1999)

[14] K. Sakai, E. Miyai, T. Sakaguchi, D. Onishi, T. Okano, and S. Noda, "Lasing band-edge identification for a surface emitting photonic crystal laser", *IEEE J. Select. Areas Commun.*, **23**(7), 1335 (2005)

[15] M. Imada, A. Chutinan, S. Noda, and M. Mochizuki, "Multidirectionally distributed feedback photonic crystal lasers", *Phys. Rev. B*, **65**, 195306 (2002)

[16] R. J. E. Taylor, D. M. Williams, J. R. Orchard, D. T. D. Childs, S. Khamas, and R. A. Hogg, "Band structure and waveguide modelling of epitaxially regrown photonic crystal surface-emitting lasers", J. Phys. D: Appl. Phys., 46(26) 264005 (2013)

[17] Y. Kurosaka, K. Sakai, E. Miyai, and S. Noda, "Controlling vertical optical confinement in two-dimensional surface-emitting photonic-crystal lasers by shape of air holes", Opt. Express, 16(22), 18485 (2008)

[18] C. Peng, Y. Liang, K. Sakai, S. Iwahashi, and S. Noda, "Coupled-wave analysis for photonic crystal surface emitting lasers on air holes with arbitrary sidewalls", Opt. Express, 19(24), 24672 (2011)

[19] S. Iwahashi, K. Sakai, Y. Kurosaka, and S. Noda, "Air-hole design in a vertical direction for high-power two-dimensional photonic-crystal surface-emitting lasers", J. Opt. Soc. Am. B, 27(6), 1204-1207 (2010)

[20] M. Yoshida, M. De Zoysa, K. Ishizaki, Y. Tanaka, M. Kawasaki, R. Hatsuda, B. Song, J. Gelleta, and S. Noda, "Double-lattice photonic-crystal resonators enabling high-brightness semiconductor lasers with symmetric narrow-divergence beams", *Nature Mater.*, **18**, 121 (2019)

[21] D. M. Williams, K. M. Groom, B. J. Stevens, D. T. D. Childs, R. J. E. Taylor, S. Khamas, R. A. Hogg, N. Ikeda, and Y. Sugimoto, "Epitaxially regrown GaAs-based photonic crystal surface-emitting laser", IEEE Photon. Technol. Lett., 24(11), 966-968 (2012)

[22] R. J. E. Taylor, D. M. Williams, D. T. D. Childs, B. J. Stevens, L. P. Shepherd, S. Khamas, K. M. Groom, R. A. Hogg, N. Ikeda, and Y. Sugimoto, "All-semiconductor photonic crystal surface emitting lasers based on epitaxial regrowth", IEEE J, Sel. Top. Quant. Electron., 19(4), 4900407 (2013)

[23] C. Reuterskiöld Hedlund, J. M. De Pina, A. Kalapala, Z. Liu, W. Zhou, and M. Hammer, "Buried InP/airhole photonic-crystal surface-emitting lasers", Phys. Status Solidi A, 218, 2000416 (2021)

[24] M. Yoshida, M. Kawasaki, M. De Zoysa, K. Ishizaki, R. Hatsuda, and S. Noda, "Fabrication of photonic crystal structure by tertiary-butyl arsine-based metal-organic vapor-phase epitaxy for photonic crystal lasers", *Appl. Phys. Express*, **9**, 062702 (2016)

[25] L-R. Chen, K-B. Hong, K-C. Huang, C-L. Liu, W. Lin, and T-C. Lu, "Study of epitaxial regrowth process by MOCVD for photonic crystal surface emitting lasers", Cryst. Growth Des., 21(6), 3521 (2021)

[26] A. F. McKenzie, B. C. King, K. J. Rae, S. Thoms, N. D. Gerrard, J. R. Orchard, K. Nishi, K. Takemasa, M. Sugawara, R. J. E. Taylor, D. T. D. Childs, D. A. MacLaren, and R. A. Hogg, "Void engineering in epitaxially regrown GaAs-based photonic crystal surface emitting lasers by grating profile analysis", Appl. Phys. Lett., 118, 021109 (2021)

Chapter 2 |

Background

This chapter presents an overview of the theory behind the key concepts and experimental techniques discussed in this thesis. Initially, metalorganic vapour phase epitaxy (MOVPE) is introduced as the main growth method used throughout the experimental sections. The reactor design is discussed, and the reaction mechanism explored in the context of planar growth. Following this, the more complex kinetics associated with growth of non-planar structure on patterned substrates are outlined. The principles of photonic crystal surface emitting laser (PCSEL) operation and important photonic crystal (PC) grating design parameters are then described, and previous work on epitaxial regrowth of devices reviewed. Finally, the principles of scanning transmission electron microscopy (STEM) are introduced.

2.1. Metalorganic Vapour Phase Epitaxy

Since it was first demonstrated by Harold Manasevit in 1968 [1], metalorganic vapour phase epitaxy (MOVPE) has become a key technique for the growth of high-quality, high-purity III-V compound semiconductor materials. Modern reactor systems are designed for high-volume, high-uniformity growth of materials, making MOVPE the main growth technique in industrial manufacturing of III-V optoelectronic devices. Improvements in the manufacture of precursor materials, the use of computerised gas delivery systems, and optimised chamber design [2], allow for growth rates as high as tens of microns per hour to be realised, precise tuning of doping levels, and control over the abruptness of layer interfaces down to the monolayer level to be achieved [3].

MOVPE is a non-equilibrium growth technique whereby layers of material are deposited epitaxially on a substrate with a similar crystal structure through the high-temperature reaction of two or more gas-phase precursor molecules separately containing group-III (Al, Ga, In) and group-V (N, P, As, Sb) atoms [4]. The group-III precursors are organometallic compounds in which the metal atom is bound to a number of organic radical groups, most commonly methyl- and ethyl- groups, and are supplied as liquid sources in pressure and temperature-controlled containers, or “bubblers” [5]. Within the bubbler, a vapour phase exists in equilibrium with the liquid, the molar concentration of which is set by the temperature and pressure. The trimethyl-metal compounds (TMAl, TMGa, TMIn) are more widely used than their triethyl- equivalents due to their more favourable vapour pressures at room temperature, and their requirement for higher temperatures to fully pyrolyse (thermally dissociate) [6]. The vapour phase molecules are transferred from the gas

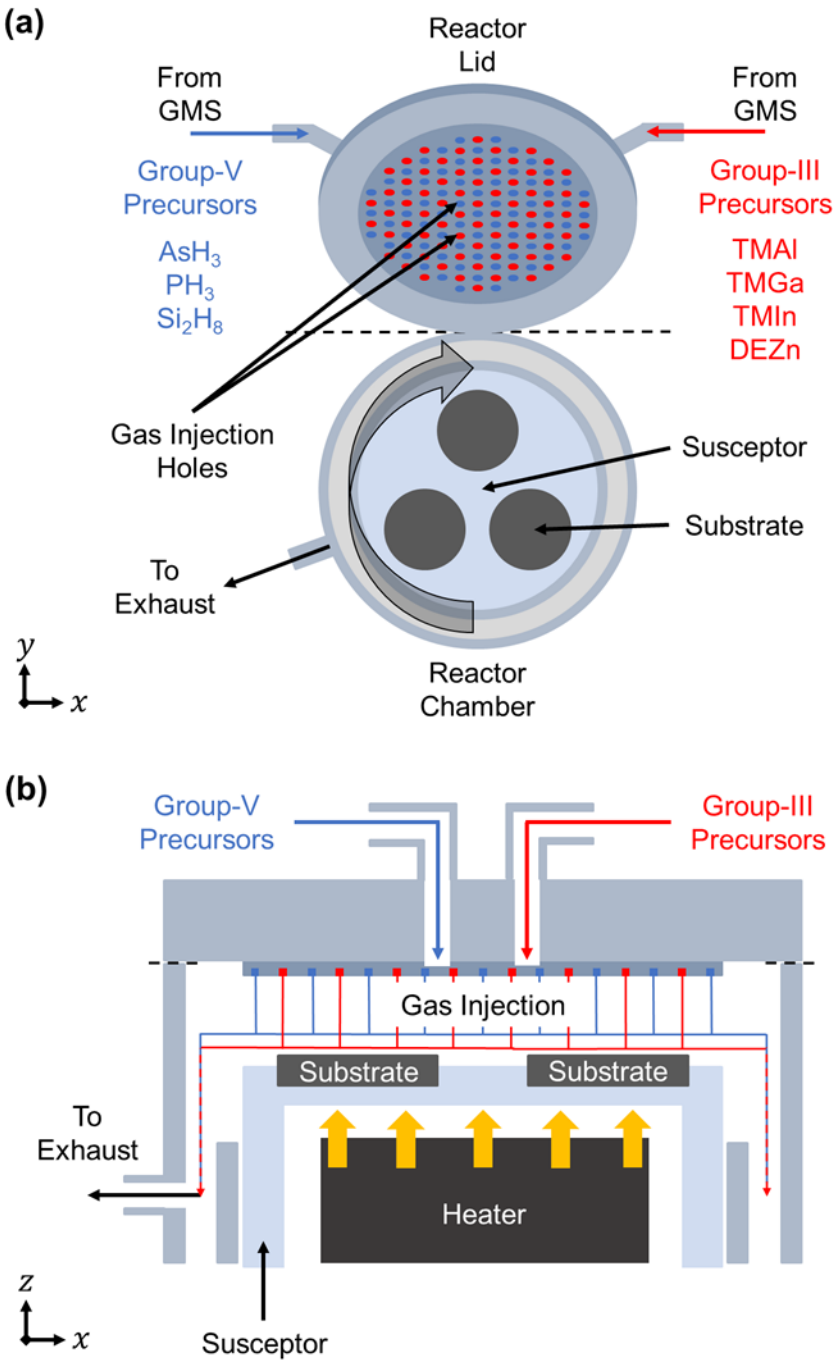

Figure 2.1. (a) Plan-view and (b) cross-sectional schematics illustrating the configuration of the close coupled showerhead design of MOVPE reactor. The substrate wafers are places on a rotating susceptor plate and heated to the growth temperature, typically 550 – 750 °C. At a chamber pressure of approximately 100 mbar, group-III and group-V precursor material are separately injected into the chamber through a series of holes in the reactor lid. As the gas flow is pulled laterally across the substrates towards the exhaust manifold, the source molecules thermally decompose, and reactive species diffuse towards the growth interface on the substrate where they are consumed.

mixing system (GMS) to the reactor chamber using a carrier gas, typically hydrogen (H_2), that is first passed through the bubblers, and then subsequently through a series of mass flow controllers (MFCs) that are used to precisely tune the molar flow (mol/min) of reactant species [7]. Common group-V sources are the hydrides, such as arsine (AsH_3) or phosphine (PH_3), which are supplied as high-purity gases that are flown directly into the reactor.

Schematic diagrams illustrating the chamber configuration for the close coupled showerhead (CCS) reactor design used in this thesis are shown in Figure 2.1. Prior to growth, the substrate wafer is loaded into a recess, or "pocket", in a susceptor plate that encloses a tungsten heating element. The reactor pressure is then reduced from atmospheric pressure to approximately 100 mbar and the chamber is heated to bring the surface temperature of the wafer to the growth temperature – this differs for different material systems but is typically in the range of 550 – 750°C for III-P and III-As compounds [4]. The group-III and group-V sources are the injected into the chamber separately through a series of holes in the reactor lid to ensure a uniform distribution, and the gas flow is pulled laterally outwards towards the chamber sidewalls and into the exhaust manifold. As the gas flow moves across the substrate, the precursor molecules undergo thermal decomposition into their reactive species, which diffuse from the laminar source flow towards the surface of the wafer. In order to maintain a uniform concentration of reactants at the growth interface, the wafers are rotated during deposition - if left stationary, the consumption of reactants would lead to a concentration gradient across the wafer as the gas flow passes over it, resulting in non-uniform layer thicknesses and compositions [8].

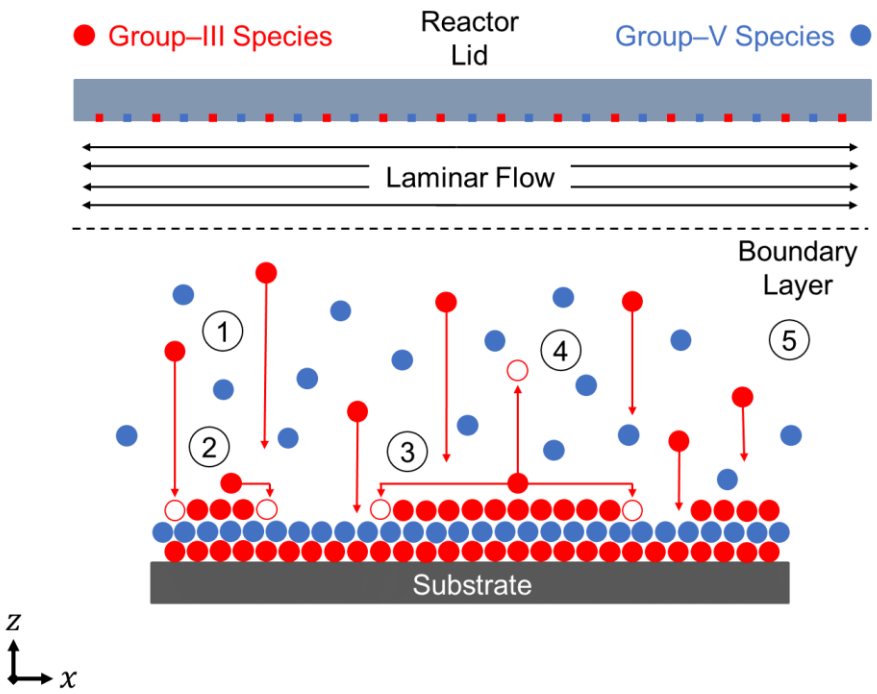

Figure 2.2. Schematic diagram illustrating the main stages of the epitaxial growth process. 1. Boundary layer diffusion. 2. Adsorption of reactive species. 3. Adatom diffusion and incorporation. 4. Desorption of excess reactant species. 5. Diffusion of reaction by-products into exhaust flow. As group-V species are present in a large excess, the growth rate in the mass-transport limited regime is determined by the diffusion of group-III species to the substrate, and is therefore directly proportional to the total group-III gas-phase concentration.

Consider the growth of binary GaAs on its native substrates using TMGa and AsH_3, for which the overall reaction is simplified to:

$$Ga(CH_3)_3 + AsH_3 \rightarrow GaAs + 3CH_4$$

The underlying growth mechanism in MOVPE is rather more complex, however, and can be broken into five main steps [9], which are illustrated in Figure 2.2. Initially, precursor molecules leave the laminar gas flow above the substrate and diffuse across a boundary layer towards the growth interface on the surface (step one). Here, AsH_3

"cracks" to produce arsenic and hydrogen, and the TMGa molecules decompose into reactive ion species and methyl radicals, as described below [4]:

$$Ga(CH_3)_3 \rightarrow Ga(CH_3)_2^{\circ} + CH_3^{\circ}$$

$$CH_3^{\circ} + H_2 \rightarrow CH_4 + H^+$$

$$H^+ + Ga(CH_3)_2^{\circ} \rightarrow Ga(CH_3)^{\circ} + CH_4$$

Once they arrive at the substrate, the reactive species adsorb to a site on the surface (step two), after which the adatoms diffuse to appropriate bonding sites at the step edges of the atomic monolayer and incorporate within the layer (step three). The surface reaction is given by:

$$Ga(CH_3)^{\circ} + AsH^{\circ} \rightarrow GaAs + CH_4$$

In the case of Frank-Van der Merwe growth, such as in the growth of conventional quantum well structures, deposition proceeds in a layer-by-layer manner, with a single atomic layer forming before the subsequent layer nucleates. If there is a large mismatch between the lattice constants of the epitaxial layer and substrate material, as in the growth of quantum dots, the strain in the layer results in three-dimensional island-like growth, in what is known as the Stranski-Krastanov mode [10]. Both modes are illustrated in Figure 2.3. Following incorporation, excess reactant species and reaction by-products desorb form the surface (step four), and then diffuse away from the growth front (step five), re-join the laminar gas flow, and are carried to the exhaust.

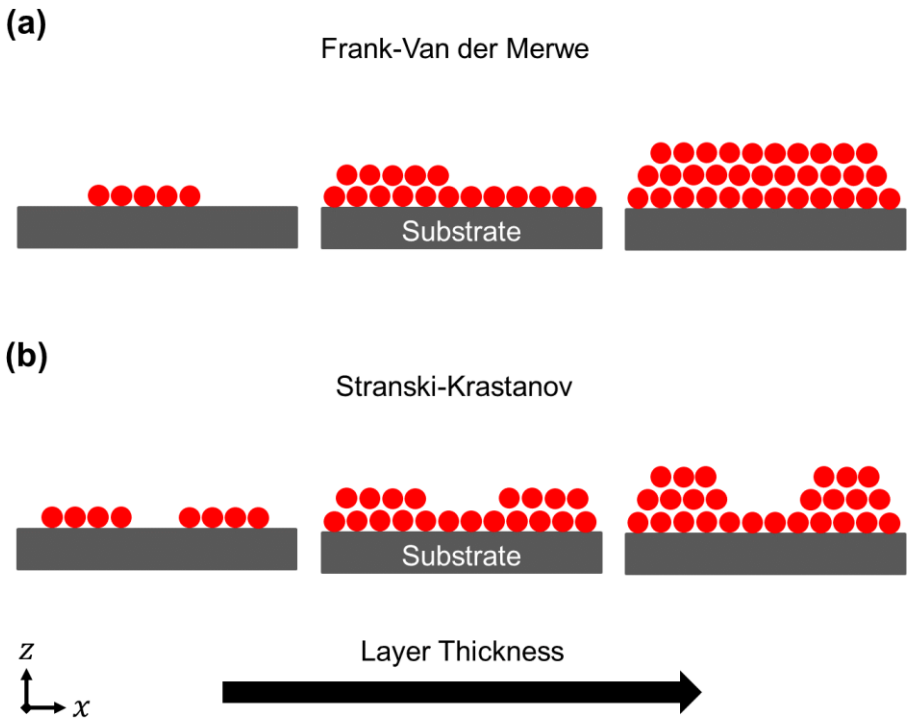

Figure 2.3. Schematic diagrams illustrating common growth modes in MOVPE of III-V materials. (a) In the Frank-Van der Merwe mode, growth proceeds in a 2D "layer-by-layer" manner where complete monolayers form before nucleation of the subsequent layer – the mechanism during growth of quantum wells (b) In the Stranski-Krastanov mode, high strain in the epi-layer promotes 3D growth and the formation of islands – the mechanism during growth of quantum dots.

In the temperature range typically employed for growth of III-V materials, 550 – 750°C, group-V species readily desorb from the wafer surface and so a large group-V overpressure is required to preserve the surface of the substrate and provide high-quality epi layers [11]. As such, the molar flow and gas-phase concentration of group-V precursor is typically in a large excess compared to the group-III – the ratio of these concentrations, the V/III ratio, is typically greater the 50, but varies from rector-to-reactor. The rate determining step in the surface reaction is the arrival of species at the growth interface and is limited by the diffusion of species across the boundary layer. In this mass-transport-limited growth regime, the growth rate is approximately

independent of temperature and is directly proportional to the total gas-phase group-III molar concentration, with a larger mol/min source flow resulting in higher growth rates and thicker layers [12]. At temperatures below 550°C, the reaction is kinetically limited by the dissociation of the organometallic molecules, whilst above 750°C it is thermodynamically limited due to the rapid desorption of group-III species from the wafer surface. Growth of ternary compounds such as $Al_xGa_{1-x}As$ or $In_xGa_{1-x}As$ (and indeed quaternary materials) is achieved simply by introducing multiple group-III precursors into the reactor chamber simultaneously, with the gas-phase ratio in the concentration of the metal species determining the solid composition of the layer [3].

2.2. Growth on Patterned Substrates

Whilst growth of III-V materials is typically conducted on planar (100)-orientated substrates, the integration of wavelength-selective grating elements into devices such as PCSELs requires the use of wafers that have been patterned to produce a non-planar, corrugated surface. Growth on patterned substrates is complicated by the presence of (potentially very many) crystallographic planes, which may exhibit very different chemical properties, and the diffusion of adatoms between planes which can result in complex, facet-dependent growth kinetics and a large variation in growth rate across the pattern [13]. Consequently, the conditions employed during deposition, such as the growth temperature, growth rate, and V/III ratio, must be carefully chosen to tune the surface mobility of adatoms in the system to achieve the desired growth profile [14].

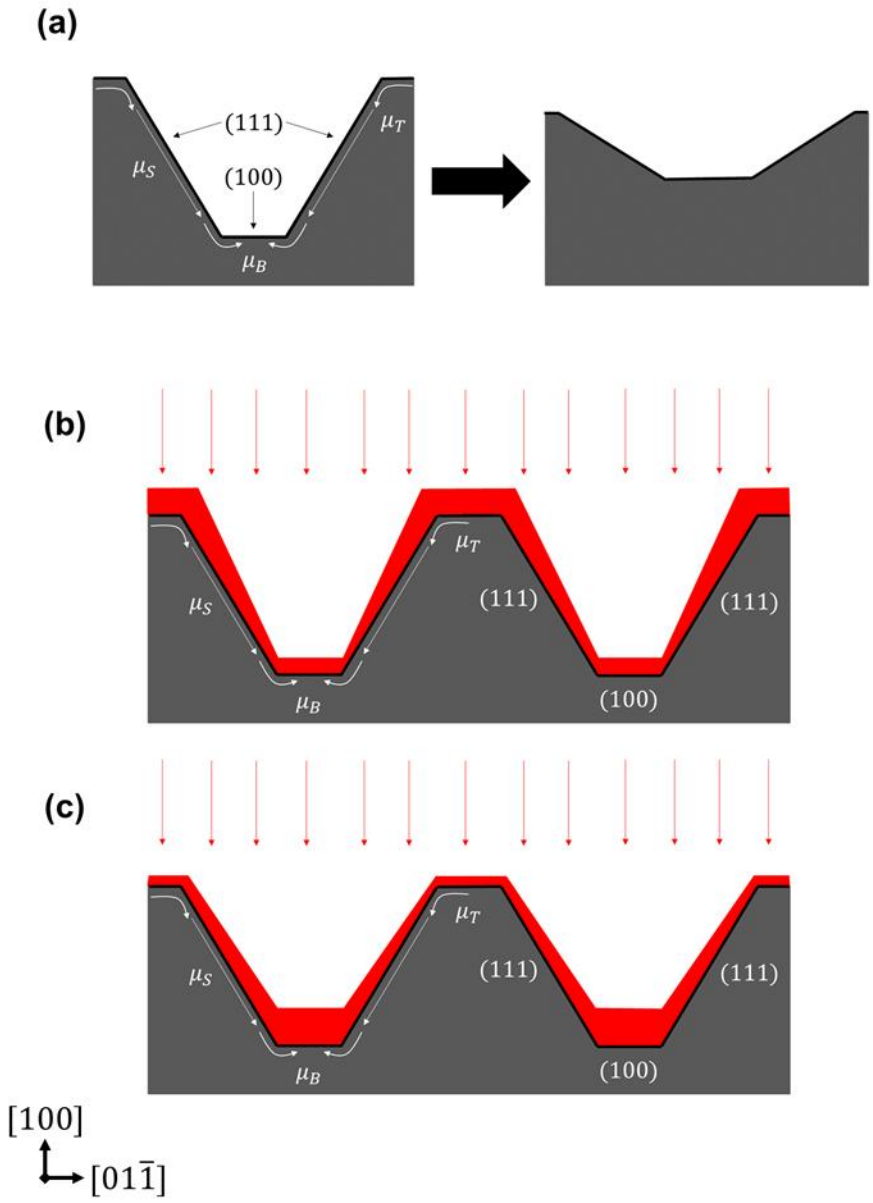

Figure 2.4. Schematic diagram illustrating growth on a substrate patterned with v-groove trenches consisting of top (T) and bottom (B) (100) surfaces and $\{111\}$ sidewall (S) planes. (a) At elevated temperatures, the gradient in chemical potential that exists across the trench, $\mu_T > \mu_S > \mu_B$, drives diffusion of atoms from the upper surfaces to the bottom of the pit (as indicated by white arrows). This process leads to infilling of the pit and, over time, would lead to re-planarisation of the surface. During deposition, growth and diffusion compete and the growth profile obtained is dependent on the local growth rates of the planes within the trench. Example growth profiles for the cases of (b) low and (c) high adatom surface mobilities are shown.

Consider, as an example, the case of a v-groove trench with inclined $\{111\}$ sidewall planes and (100) planes at the top and bottom of the pit, as shown in Figure 2.4. Such a trench can be fabricated though selective etching processes that exploit the low etch rates of the sidewall facets compared with the (100) plane [15]. By patterning the wafer, the stable bonding configuration of the surface atoms is disrupted and a non-uniform chemical potential, μ, is introduced across the trench, with the potential on the top surface and sidewalls being higher than that of the bottom surface due to reduced bonding coordination [13]. Consequently, at elevated temperatures, such as those used during MOVPE growth, the atoms have sufficient thermal energy and will be driven to diffuse from the upper surfaces towards the bottom of the trench in order to minimise the total surface energy of the system [16]. Over a sufficiently long timescale, this "mass-transport" of material from sites on concave surfaces to the more favourable bonding sites on convex surfaces leads to a re-planarisation of the wafer and the loss of the pattern, as illustrated in Figure 2.4(a). The role of mass-transport during regrowth of PCSELs is explored further in Chapter 3. (Whilst they share a similar nomenclature, this process of surface diffusion should not be confused with the mass-transport-limited growth regime described in Section 2.1. which also applies during growth on patterned substrates.)

The mass-transport process is quenched by deposition of the epi layer, however the capillary forces driving diffusion continue to impact adatom kinetics during growth and play a role in shaping the growth profile obtained. Ultimately, the growth profile is determined by the relative local growth rates on each of the crystal planes, which are a function of the inherent incorporation rates of the plane, the atomic flux incident on the facet from the vapour phase, and the net atomic flux to and from it

due to the migration of adatoms [13]. The incorporation rate of a facet is dependent on the atomic arrangement on the surface and the density of unoccupied bonding sites. A plane with a large number of dangling bonds has a high sticking probability for incoming reactive species, which consequently exhibit shorter diffusion lengths, resulting in a high growth rate [17]. Whereas the concentration of reactants in the vapour phase above a planar wafer is uniform and the incident atomic flux at each point on the surface is equal, the crystal planes in patterned system experience different reactant concentrations [18]. For facets at the bottom of the trench, the atomic flux is depleted compared with that at the top surfaces, and so these planes display a lower local growth rate. An example of a growth profile obtained in this case is illustrated in Figure 2.4(b). When the surface mobility and diffusion lengths of adatoms are sufficiently high, capillary forces dominate in the system and species diffuse away from the planes on which they initially adsorb [19]. As a result, the local growth rates on the upper surfaces of the pit are reduced relative to the low mobility case, and the rate on the lower planes is enhanced. An example of a growth profile obtained in this case is illustrated in Figure 2.4(c). It has been shown that the surface mobility of adatoms on patterned substrates are significantly impacted by the growth condition used, with higher growth temperatures and lower growth rates promoting high mobility and increased diffusion [17,19,20], thus providing a route for precise engineering of the growth kinetics in the system. The growth profiles obtained during regrowth of PCSELs, the kinetic factors affecting their evolution during deposition, and their relationship to the geometry of voids that form in these structures are investigated in Chapters 4 & 5.

2.3. Photonic Crystal Surface Emitting Lasers

The structural feature that distinguishes a photonic crystal surface emitting laser (PCSEL) from contemporary edge- and surface-emitting devices is the integration of a two-dimensional (2D), second-order Bragg grating layer within the epi stack, adjacent to the active region of the device [21]. The grating layer, or photonic crystal (PC), comprises a 2D, periodic variation in refractive index based on a repeated unit cell. The unit cell is composed of a matrix material with refractive index, n_1 into which a region of material with a different refractive index, n_2 , or PC "atom", is introduced [22]. The simplest PC geometry, and the one discussed throughout this thesis, is the square-lattice configuration with circular atoms, a schematic of which is show in Figure 2.5(a). The repeated unit cell, which is highlighted in the dashed box, is a square with a length, a, which defines the period of the PC.

Light emitted by the active region couples to the PC and proceeds to propagate within it, being scattered at the interface between the regions of different refractive index [23]. The scattering mechanism is described in Figure 2.5(a). Consider a wave, κ_i, that is incident on the central atom. When it encounters the change in refractive index at the boundary of the atom, the wave undergoes both 1D scattering in the forward in back directions, and 2D scattering in the orthogonal and oblique directions, towards the neighbouring atoms [24]. The relative strengths of the scattering are given by the respective 1D and 2D coupling coefficients, κ_3 and κ_1 , which are dependent on the design of the unit cell (as discussed further, below). In addition to this in-plane coupling, light is also coupled out-of-plane by second-order effects, producing the characteristic surface emission of PCSELs.

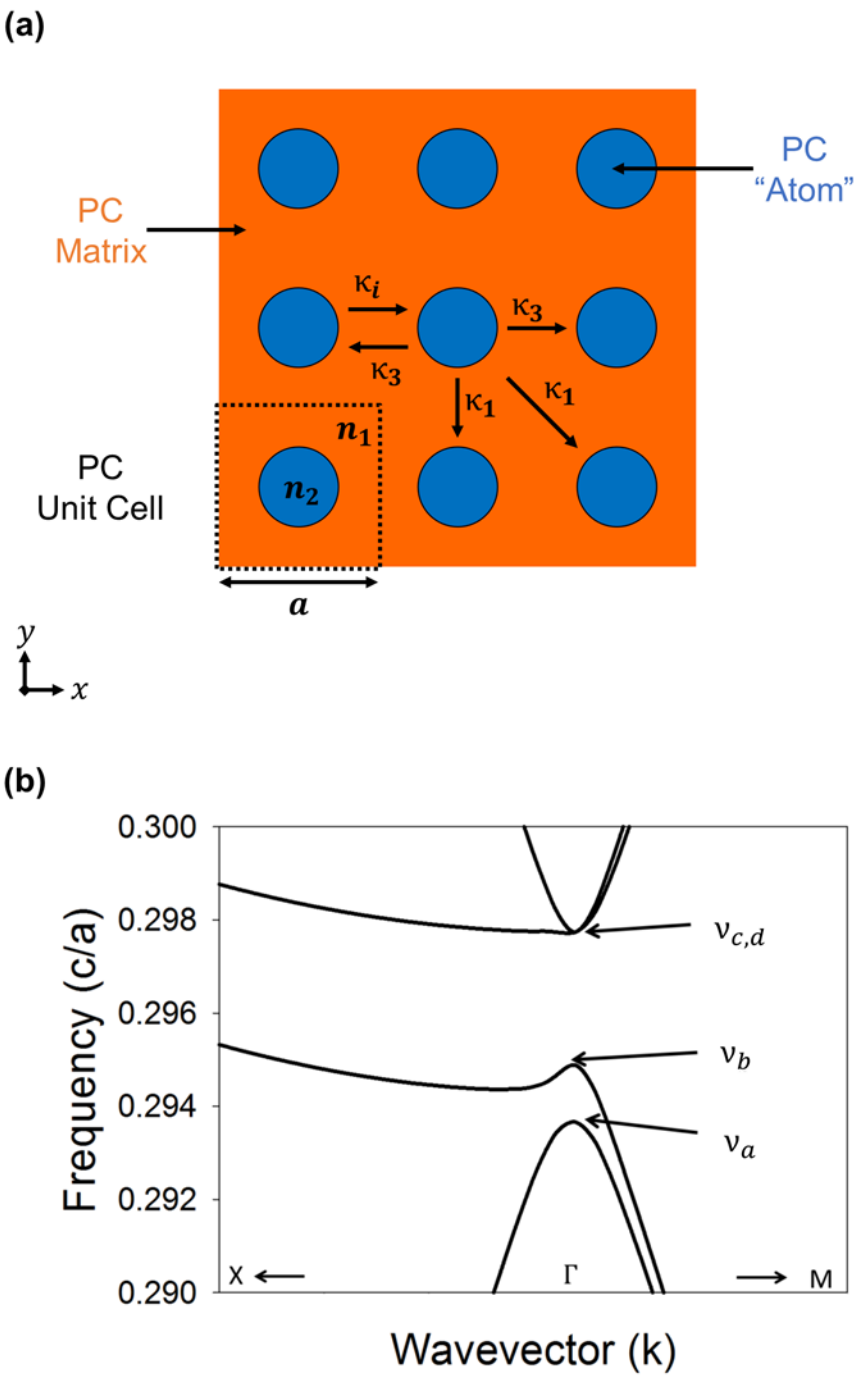

Figure 2.5. (a) Schematic diagram illustrating the coupling mechanism in a square-lattice PC. The unit cell is composed of a PC atom with refractive index, n_2, within a matrix material, n_1. A wave, κ_i, incident on the central atom undergoes 1D, κ_3, and 2D, κ_1, scattering towards the neighbouring atoms; light is also scattered out-of-plane by second-order effects. (b) Reduced photonic band structure for the square-lattice PCSEL [25]. At the Γ-point, the PC acts as 2D resonant cavity at each of the four band-edge frequencies, ν, supporting coherent laser oscillation and producing single-mode emission perpendicular to the device surface.

As a result of the complex nature of the scattering and interference of light within the grating, a PC can only support in-plane oscillation for modes with a small number of discrete frequencies, giving rise to a photonic band structure [24]. The reduced band structure for square-lattice PC, which has been modelled numerically elsewhere [25], is shown Figure 2.5(b) and describes the permitted band-edge frequencies, ν, as a function of wavevector, k. Here the wavevector describes the angular component of the vertically emitted light and is given by $k = \frac{2\pi}{a} sin\vartheta$ [26]. At the Γ-point, where light is scattered perpendicular to the surface of the device ($\vartheta = 0$), coherent 2D in-plane coupling of light occurs and a large-area standing wave is formed across the entire grating. For each of the four Γ-point frequencies of the band structure, the PC acts as a resonant cavity, providing distributed optical feedback for the mode, supporting in-plane laser oscillation [21]. The absolute values of the band-edge frequencies, ω, are given by the following equations:

$$\nu_a = \frac{c}{n_{av}}(\beta_0 + \kappa_3)(1 - \frac{8{\kappa_1}^2}{{\beta_0}^2 - {\kappa_3}^2})$$

$$\nu_b = \frac{c}{n_{av}}(\beta_0 - \kappa_3)$$

$$\nu_{c,d} = \frac{c}{n_{av}}(\beta_0 + \kappa_3)(1 - \frac{4{\kappa_1}^2}{{\beta_0}^2 - {\kappa_3}^2})$$

where c is the speed of light; κ_3 and κ_1 are the 1D and 2D coupling coefficients, respectively; $\beta_0 = \frac{2\pi}{a}$ for a PC with period, a; and n_{av} is the average refractive index of the unit cell [28]. By aligning the Γ-point frequencies of the band structure to the gain spectrum of the active region of the device, a single-mode, surface emitting

laser can be realised, with the emission wavelength corresponding to that of the mode with the lowest threshold gain.

The optical and electrical properties of a PCSEL are directly determined by the nanoscale structure of the PC layer and unit cell. Much of the research into PCSELs has focused the optimisation of the unit cell design to provide the highest possible in-plane coupling coefficients and maximizing the out-coupling of the vertically scattered light. In this regard, it is the properties of the PC atom that has largest impact on device performance. Whilst the work in this thesis does not explicitly focus on optimising the design of the PC grating or performance of devices, the size and shape of the void structures obtain during the regrowth experiments described in Chapters 3 and 4 are partially analysed in terms desirable PC atom geometries derived from simulation-based studies in the literature. As such a brief summary of the key design elements is presented below. For a more expansive discussion on PCSEL design the reader is directed to the excellent reviews published by Ishizaki *et al*. [21], Taylor [26], and King [29].

In the fabrication of high-performance devices, the largest possible coupling values are required in order to maintain coherent laser oscillation across large 2D PC areas and minimise the parasitic loss of light from the edges of the PC [21]. Optimisation of the coupling coefficients, κ_3 and κ_1, leads to a relative reduction in the threshold current density of the device and allows for extraction of light from the entire device surface, maximising the potential output power [30]. The most significant factor impacting the strength of the 1D and 2D coupling of the PC is the choice of grating infill. Owing to the large difference in refractive index between semiconductor ($n_1 \sim 3.2$) and air ($n_2 = 1$), void-containing PCSELs can display coupling

values that are three or four times larger than the equivalent all-semiconductor devices [29]. Consequently, void-containing devices typically show superior parametric performance; indeed, state-of-the-art devices exclusively utilise the void-containing PC system [31]. Another element affecting the strength of the grating is the fill factor of the PC atom. This is the relative volume that the atom occupies within the unit cell, and determines the average refractive index, n_{av}. In the case of a circular atom, a schematic of which is shown in Figure 2.6(a), the fill factor of the grating is conventionally referred to by its r/a value, which denotes the ratio of the atom radius, r, and the PC period, a. It has been shown through simulation that the in-plane the coupling strengths of the PC varies considerably with fill factor for both the void-containing and all-semiconductor systems and that, whilst the maximum coupling values of the two systems differ (being dependent on the extent of the refractive index contrast), the magnitudes of the κ_3 and κ_1 coefficients have local maxima for r/a = 0.2 and 0.4 in both cases [32], producing two regions of interest when considering PC design.

The geometry of the PC atom is also crucial in realising high-output power devices. Whilst circular grating pits represent one of the simplest structures to fabricate, their high geometric symmetry with respect to the axes of the PC results in relatively poor out-coupling of light and low-output powers [33]. One route to increasing the power of the device is to use atom shapes with reduced in-plane symmetry, which have been shown to display lower optical confinement factors and result in less destructive interference of vertically scattered light [34]. This principle was most notably demonstrated in the case of the first Watt-class PCSEL, which utilised a triangular atom (the unit cell of which is shown in Figure 2.6(a)) [31]. The

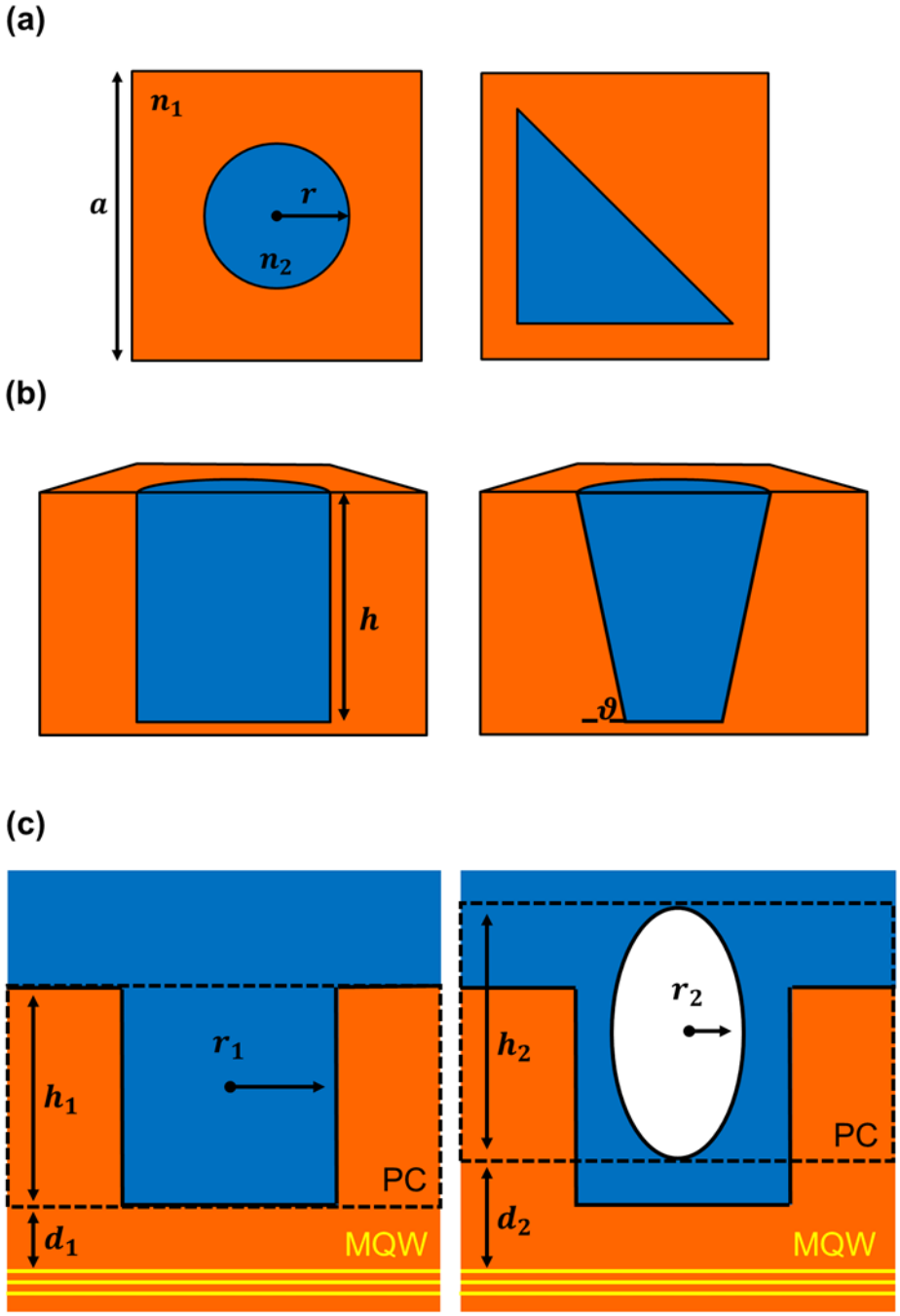

Figure 2.6. Schematic diagrams illustrating the key considerations for unit cell design. For a circular atom, the coupling strength varies with fill factor, and is maximised for $r/a = 0.2, 0.4$. (a) The out-coupling of light increases for atom shapes with reduced in-plane symmetry, such as a triangle. (b) Output power can also be increased by breaking the out-of-plane symmetry of the atom, for example, by introducing an angled sidewall profile. Destructive interference of vertically scattered light is minimised for an atom height, $h = 0.5a$ (c) For a void-containing PCSEL realised by MOVPE regrowth, the key PC dimensions will differ from those of an all-semiconductor structure obtained using the same grating pit geometry.

beneficial effects of reduced atom symmetry may also be extended to the out-of-plane direction (as illustrated Figure 2.6(b)), where the use of grating pits with sloped or tilted sidewalls has also been shown to result in reduced optical confinement and destructive interference compared with those with vertical sidewalls [35]. The final element that can be tuned to provide the largest out-coupling from the PC is the depth of the grating pit, or atom height, for which an optimum value of $h = 0.5a$ has been shown to minimise destructive interference and provide the maximum radiation constant [36].

2.4. Epitaxial Regrown of PCSELs

The elements of unit cell design outlined at the end of Section 2.3. provide key dimensions that should be targeted during fabrication and regrowth of the PC grating layer. For an all-semiconductor structure, where the grating pits are completely infilled, the properties of the PC are simply determined by the geometry of the as-etched pits, and are therefore relatively easy to tune. For void-containing PCSELs, however, the PC properties are less predictable. In this case, the grating layer acts as a template and the dynamics of grating infill typically result in voids with a radius, r, and height, h, which differ from those of the underlying pits. This is illustrated schematically in Figure 2.6(c); here, the location of the encapsulated PC layer is shifted with respect to the active region, and the change in separation, d, may result in reduced mode overlap with the grating [32]. Consequently, the epitaxial regrowth process must be designed so as to control the degree of grating infilling to either

eliminate or promote the formation of voids and, in the latter case, engineer their geometries for optimised device performance.

The first reported use of MOVPE-based methods for achieving embedded PC layers related to GaN-based devices, for which wafer bonding technology was not sufficiently mature at the time. In 2008, Matsubara *et al*. presented an "air-hole retained overgrowth" (AROG) method to demonstrate pulsed, room-temperature operation of a fully MOCVD grown device [37]. The principle of AROG exploited the unique crystal plane kinetics of GaN, in combination with SiO_2 deposited in the bottom of the grating pits, to promote lateral growth of the *n*-GaN cladding layer and encapsulate the voids without growth within the pits themselves.

Following this, in 2012 and 2013, Williams *et al*. presented a series of papers describing the first examples of an all-semiconductor PCSELs achieved by regrowth of a GaInP grating layer with GaAs [38,39]. It was reported that voids had formed during initial regrowth attempts using a set of conditions nominally optimised for regrowth of equivalent DFB grating structures [40,41]. The formation of voids in the first instance was attributed to the growth dynamics within the large-aspect ratio grating pits used for PCSELs compared with the much shallower gratings of the DFB, and it was surmised that it was necessary to increase the surface mobility of Ga adatoms in order to achieve complete infilling. As the regrowth process relied on a narrow temperature window in order to limit As/P exchange in the GaInP grating layer (605 °C), a reduced AsH_3 flow (i.e. lower V/III ratio) was employed in order to eliminate the voids.

The next major step in the progress of MOVPE-regrown PCSELs came in 2014, when Hirose *et al*. reported watt-class operation for a void-containing PCSEL utilising the AlGaAs/GaAs PC system [31]. In this case, the initial PC grating pits were right-angled triangular prisms which, when regrown with a *p*-AlGaAs layer, produced voids with a high degree of asymmetry both in the plane of the PC and in the vertical direction. This publication was followed by those of Yoshida *et al.*, which provided a more in-depth analysis of the regrowth process employed, and the subsequent void shape obtained with the triangular grating pits. Overall, the diameter of the voids was narrower than that of the initial pit (130 nm vs 180 nm), however their height was greater than the pit depth (280 nm vs 250 nm), indicating that, whilst encapsulation is driven by lateral growth of material at the top surface of the pit, a limited amount of deposition occurs within it [42]. It was shown that the asymmetric shape of the voids in the z-direction was the result of the non-uniform nature of the deposition on the vertical pit sidewalls, causing the diameter of the voids to narrow towards a point at the top of the voids. The in-plane asymmetry was attributed to the asymmetric shape of the triangular pits and the differing crystal plane kinetics associated with the $(01\bar{1})$, $(0\bar{1}\bar{1})$, and (001) crystal planes that bound it [43].

More recently, an important regrowth study presented by Reuterskiöld Hedlund *et al*. explored void engineering in the InP PC system [44], showing that the size of voids can be tuned significantly through the choice of regrowth conditions. Whilst large voids were produced at low growth temperatures (470 °C), the height of the voids decreased with increasing temperature (520 °C), and an all-semiconductor structure as ultimately achieved (560 °C). The trend in increased infilling with increasing temperature, which was attributed to a higher adatom surface mobility

and greater diffusion of material into the pits, was replicated at a reduced V/III ratio and growth rate, which also resulted in smaller voids being formed.

To date, the extent to which void size engineering can be achieved in the AlGaAs/GaAs PC system is an open question. There have been no reports thus far describing the role of growth conditions in tuning adatom mobility and grating infilling in this system, and it is unclear whether an all-semiconductor infill can be achieved and what conditions might promote this. Additionally, whilst there are examples in the literature describing void formation in AlGaAs/GaAs structures [42,43,45], these publications provided little detail of how the mechanism of void formation, and the growth kinetics driving it, influence the shape of the voids or what parameters may be leveraged to realise optimised geometries.

2.5. Electron Microscopy Analysis

The quality of planar epitaxial structures grown by MOVPE is conventionally assessed by a combination of photoluminescence (PL) spectroscopy and X-ray diffraction (XRD) measurements, which can provide information about the alloy composition and thickness of the individual layers of the material [46]. These techniques are not, however, suitable for the characterisation of nano-structured gratings within devices, which are typically buried below a micron or more of cladding material, do not produce a strong luminescence signal, and are usually lattice-matched to the surrounding layers, making them nearly indistinguishable by diffractive methods. Instead, analysis of these structures requires direct imaging of the grating layer and regrown material using electron microscopy [38,39,42-45].

Scanning electron microscopy (SEM) is a ubiquitous analytical tool that allows imaging of features at a practical resolution of a few tens of nanometers or less, with relatively large fields of view and sampling sizes [47]. Whilst this is more than adequate for studying the bulk properties of PC grating layers, such as the size and geometry of voids in these structures [42-44], SEM is limited in the ability to study the dynamics of the regrowth process in detail, or the kinetic factors that drive infilling. In this regard, the superior resolution and elemental contrast available in transmission electron microscopy (TEM) offers greater opportunity for understanding the underlying mechanisms associated with regrowth from a near atomistic perspective [48]. The power of TEM analysis in this regard has been readily demonstrated in similar systems involving the patterned growth of quantum wires, where it has been used to link adatom kinetics to the individual crystal planes of the grating layer, and infer how the growth front develops during formation of these structures [49,50].

TEM analysis requires a specimen that is transparent to the electron beam so that the accelerated electrons pass through it without undergoing multiple scattering events [48]. These lamellae, which are typically much less than 100 nm thick, are prepared using a dual-beam focused ion beam (FIB)-SEM system following well established “lift-out” protocols [51]. The FIB-SEM system, a schematic of which is shown in Figure 2.7., contain both an ion and electron column angled at 52° to each other, allowing for simultaneous milling (ion) and imaging (electron) of the sample; as such, the location of the specimen can be placed very accurately, enabling site specific lift-out specimens containing particular features of interest [52]. In addition to the small-volume milling associated with lamella preparation (the specimen

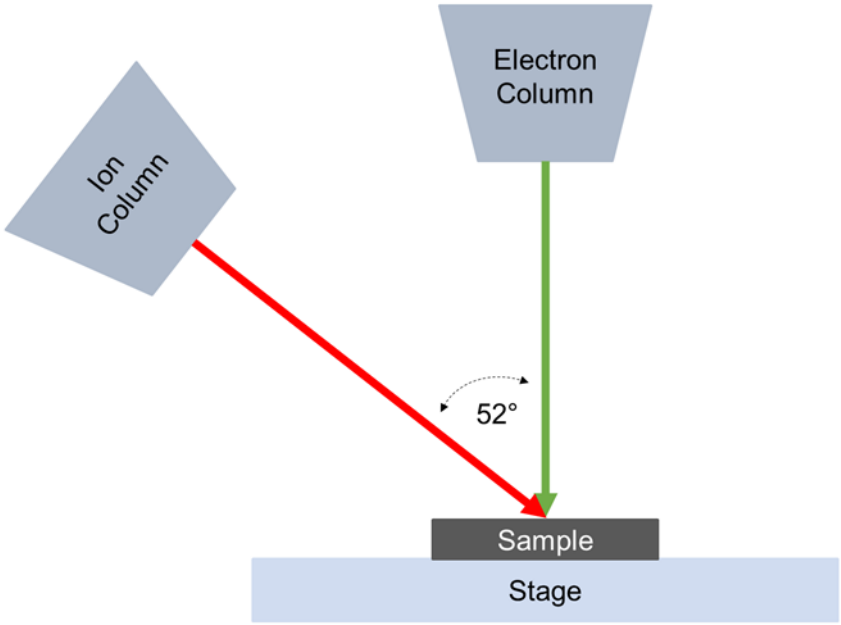

Figure 2.7. Schematic diagram illustrating the configuration of dual-beam FIB-SEM systems used for TEM lamella preparation. The system contains both an ion column for milling and an electron column for imaging, at an angle of 52° to each other. Simultaneous milling and imaging enables accurate, site-specific specimen preparation.

dimensions are typically on the order of 2 x 20 x 20 μm), the ion beam can be used to prepare large-area cross-sections through entire device structures, accessing buried features that may not be visible during standard plan-view imaging. The system used in this work utilise a xenon plasma ion source, rather than the traditional liquid Ga ion source, which provides higher milling rates that allow for more efficient sampling across large areas [53].

The configuration of the electron column of a TEM is shown in Figure 2.8(a). Electrons are produced by either thermionic or field emission processes in the electron gun and are accelerated by high-voltage anodes to an energy of 200 keV as they are extracted into the column [48]. At 200 keV, the de Broglie wavelength of

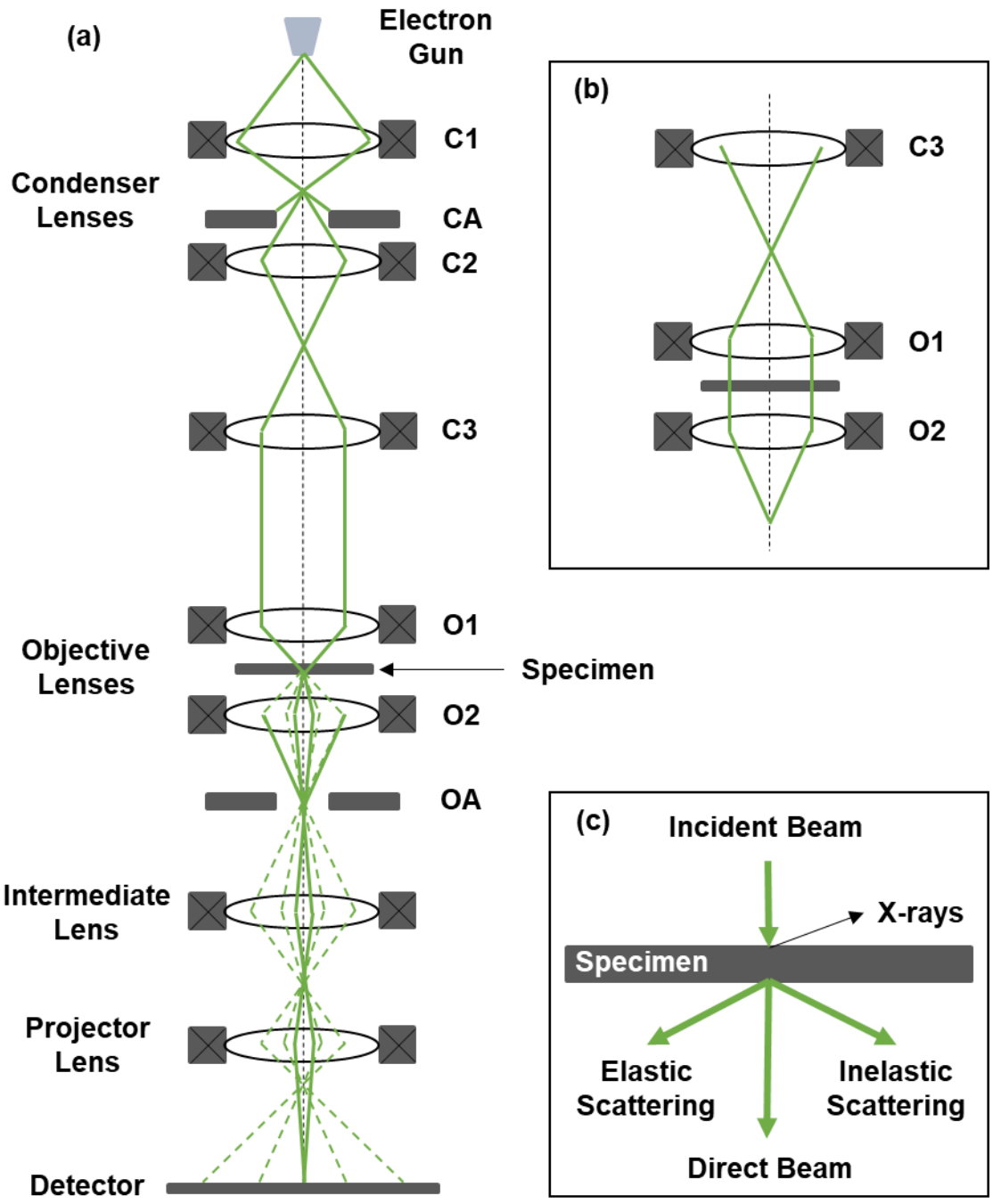

Figure 2.8. (a) Schematic diagram showing the configuration of the electron column in a transmission electron microscope, with the ray diagram (green) illustrating the path of the electron beam when operated in scanning (STEM) mode. In STEM the electron probe is focused to a point and rastered across the specimen surface, whilst in TEM (b) broad parallel illumination of the sample is used. (c) The interaction between the incident electron beam and the specimen produces many types of signals that can be accessed using different imaging modes and analytical techniques.

electrons is on the order of 2 pm, which is much smaller than the inter-atomic spacing in crystalline materials. While the ultimate resolution in TEM is limited by aberration in the magnetic lenses used to channel and focus the beam, sub-nanometer, and even sub-Ångström, resolution can be routinely achieved in modern microscopes utilising aberration corrected optics [54]. In the condenser system, three lenses are used to control the size of the beam and ensure uniform illumination of the specimen. The beam then passes into the objective system, which consists of two lenses above and below the specimen and provide the initial magnification of the image. In conventional TEM mode, the sample is illuminated by a parallel plane, as shown in Figure 2.8(b). In scanning (STEM) mode, however, the objective lens focuses the beam to a point on the sample which is then rastered across the surface to form an image, with the transmitted beam being detected at each point [55]. The image that is formed of the specimen is magnified by the intermediate lens (which, in reality, consists of multiple lenses) and is projected onto a viewing screen or detector.

The interaction between the incident electron beam and the specimen produces many types of signals that can be detected and assessed using different imaging modes and analytical techniques. A number of these signals are illustrated in Figure 2.8(c). In both TEM and STEM mode, bright-field (BF) imaging is performed using electrons from the directly transmitted beam [48]. The contrast mechanism in BF imaging is known as amplitude contrast and is the result of inelastic scattering of electrons as they pass through the specimen. Reduced signal intensity is recorded in regions of the sample that are thicker or contain heavier elements, which appear darker in images – consequently, this contrast mechanism is alternatively referred to as mass or thickness contrast. In STEM, the inelastically scattered electrons, which

scatter into different angles depending on the atomic species present in the specimen, are collected using an annular detector and are used to form annular dark field (ADF) images [56]. The contrast mechanism here is the same amplitude contrast as in BF, however the signal intensity is reversed, with denser regions producing larger signal and appearing lighter in images. In TEM, DF images are formed using elastically scattered electrons, which undergo Bragg scattering from the crystal lattice to produce diffraction patterns. The contrast mechanism here is referred to as diffraction contrast and can be enhanced by using an aperture in the back-focal-plane of the objective lens to select specific diffraction spots to construct the image. The diffraction patterns formed by these elastically scattered electrons can also be used to conduct nanoscale crystallographic analyses of the specimen in a similar way to conventional XRD. Finally, whilst not utilised in this work, the information contained within the X-ray and inelastically scattered electron signals can be extracted through powerful techniques such as energy-dispersive X-ray (EDS) and electron energy loss (EELS) spectroscopy, respectively, which can be used to perform quantitative elemental and chemical analysis [57].

2.6. References

[1] H. M. Manasevit, “Single-crystal gallium arsenide on insulating substrates”, Appl. Phys. Lett., 12(4), 156-159 (1968)

[2] J-P. Duchemin, “Low-pressure MOVPE: the time of the pioneers”, *J. Cryst. Growth*, **601**, 126939 (2023)

[3] J. J. Coleman, “Metalorganic chemical vapour deposition for optoelectronic devices”, Proc. IEEE, 85(11), 1715-1729 (1997)

[4] G. B. Stringfellow, Organometallic Vapour-Phase Epitaxy: Theory and Practice. San Diego, CA, USA: Academic Press, Inc. (1989)

[5] M. J. Ludowise, “Metalorganic chemical vapour deposition of III-V semiconductors”, *J. Appl. Phys.*, **58**, R31 (1985)

[6] A. C. Jones, “Metalorganic precursors for vapour phase epitaxy”, J. Crystal. Growth, 129, 728-773 (1993)

[7] M. Razeghi, The MOCVD Challenge. Volume 1: A Survey of GaInAsP-InP for Photonic and Electronic Applications. Bristol, UK: IOP Publishing Ltd. (1989)

[8] M. Razeghi, *Technology of Quantum Devices*, New York, NY, USA: Springer (2010)

[9] J. E. Ayers, Heteroepitaxy of Semiconductors: Theory, Growth, and Characterisation. Boca Raton, FL, USA: CRC Press (2007)

[10] J. J. Coleman, J. D. Young, and A. Garg, “Semiconductor quantum dot lasers: a tutorial”, *J. Lightwave. Technol.*, **29**(4), 499 (2011)

[11] G. B. Stringfellow, “Thermodynamic aspects of organometallic vapor phase epitaxy”, *J. Crystal. Growth.*, **62**, 225 (1983)

[12] D. H. Reep and S. K. Ghandhi, “Deposition of GaAs epitaxial layers by organometallic CVD”, *J. Electrochem. Soc.*, **130**(3), 675 (1983)

[13] E. Pelucchi, S. T. Moroni, V. Dimastrodonato, and D. D. Vvedensky, “Self-ordered nanostructure on patterned substrates”, J. Mater. Sci.: Mater. Electron., 29, 952-967 (2018)

[14] R. Bhat, E. Kapon, D. M. Hwang, M. A. Koza, and C. P. Yun, “Patterned quantum well heterostructures grown by OMCVD on non-planar substrates: applications to extremely narrow SQW lasers”, *J. Cryst. Growth*, **93**, 850 (1988)

[15] E. Kapon, S. Simhony, R. Bhat, and D. M. Hwang, “Single quantum wire semiconductor laser”, *Appl. Phys. Lett.*, **55**, 2715 (1989)

[16] Z. L. Liau and H. J. Zeiger, “Surface-energy-induced mass-transport phenomenon in annealing of etched compound semiconductor structure: theoretical modelling and experimental confirmation”, *J. Appl. Phys.*, **67**, 2434 (1990)

[17] M-S. Kim, Y. Kim, M-S. Lee, Y. J. Park, S-I. Kim, and S.K. Min, “Growth behaviour on V-grooved high Miller index GaAs substrates by metalorganic chemical vapour deposition”, J. Cryst. Growth, 146, 482-488 (1995)

[18] L. Buydens, P. Demeester, M. van Ackere, A. Ackaert, and P. van Daele, “Thickness variations during MOVPE growth on patterned substrates”, J. Electron. Mater., 19(4), 317-321 (1990)

[19] L. Hofmann, A. Knauer, I. Rechenberg, M. Weyers, and W. Stolz, “Patterned growth of (AlGa)As using metalorganic vapor-phase epitaxy”, J. Cryst. Growth, 206, 255 (1999)

[20] G. Vermeire, I. Moerman, Z. Q. Yu, F. Vermaerke, P. van Daele, and P. Demeester, “Atmospheric and low pressure metalorganic vapor phase epitaxial growth of vertical quantum wells and quantum well wires on submicron gratings”, J. Electon. Mater., 23(2), 121-124 (1994)

[21] K. Ishizaki, M. De Zoysa, and S. Noda, “Progress in photonic-crystal surface-emitting lasers”, Photonics, 6, 96 (2019)

[22] M. Imada, S. Noda, A. Chutinan, T. tokuda, M. Murata, and G. Sasaki, “Coherent two-dimensional lasing action in surface-emitting laser with triangular-lattice photonic crystal structure”, *Appl. Phys. Lett.*, **75**, 316 (1999)

[23] H. Kogelnik and C. V. Shank, “Coupled-wave theory of distributed feedback lasers”, *J. Appl. Phys.*, **43**, 2327 (1972)

[24] M. Imada, A. Chutinan, S. Noda, and M. Mochizuki, “Multidirectionally distributed feedback photonic crystal lasers”, *Phys. Rev. B*, **65**, 195306 (2002)

[25] S. Noda, M. Imada, A. Chutinan, and N. Yamamoto, “III-V based-semiconductor photonic crystals”, *Opt. Quant. Electron.*, **34**, 727 (2002)

[26] R. J. E. Taylor, “Design of photonic crystal surface emitting lasers and the realisation of coherently coupled arrays”, PhD Thesis, University of Sheffield (2015)

[27] K. Sakai, E. Miyai, T. Sakaguchi, D. Onishi, T. Okano, and S. Noda, “Lasing band-edge identification for a surface emitting photonic crystal laser”, *IEEE J. Select. Areas Commun.*, **23**(7), 1335 (2005)

[28] K. Sakai, E. Miyai, and S. Noda, “Coupled-wave model for square-lattice two-dimensional photonic crystal with transvers-electric-like mode”, *Appl. Phys. Lett.*, **89**, 021101 (2006)

[29] B. C. King, “Gallium arsenide based photonic crystal surface emitting lasers”, PhD Thesis, University of Glasgow (2021)

[30] T. Inoue, M. Yoshida, J. Gelleta, K. Izumi. K. Yoshida, K. Ishizaki, M. De Zoysa, and S. Noda, “General recipe to realize photonic-crystal surface-emitting lasers with 100-W-to-1-kW single-mode operation”, *Nature Commun.*, **13**, 3262 (2022)

[31] K. Hirose, Y. Liang, Y. Kurisaka, A. Watanabe, T. Sugiyama, and S. Noda, “Watt-class high-power, high-bean quality photonic-crystal lasers”, Nature Photon., 8, 406-411 (2014)

[32] R. J. E. Taylor, D. M. Williams, J. R. Orchard, D. T. D. Childs, S. Khamas, and R. A. Hogg, “Band structure and waveguide modelling of epitaxially regrown photonic crystal surface-emitting lasers”, J. Phys. D: Appl. Phys., 46(26) 264005 (2013)

[33] W. Kunishi, D. Ohnishi, E. Miyai, K. Sakai, and S. Noda, “High-power single-lobed surface emitting photonic crystal laser”, *2006 Conference on Lasers and Electro-Optics and 2006 Quantum Electronics and Laser Science Conference*, CMKK1 (2006)

[34] Y. Kurosaka, K. Sakai, E. Miyai, and S. Noda, “Controlling vertical optical confinement in two-dimensional surface-emitting photonic-crystal lasers by shape of air holes”, Opt. Express, 16(22), 18485 (2008)

[35] C. Peng, Y. Liang, K. Sakai, S. Iwahashi, and S. Noda, “Coupled-wave analysis for photonic crystal surface emitting lasers on air holes with arbitrary sidewalls”, Opt. Express, 19(24), 24672 (2011)

[36] S. Iwahashi, K. Sakai, Y. Kurosaka, and S. Noda, “Air-hole design in a vertical direction for high-power two-dimensional photonic-crystal surface-emitting lasers”, J. Opt. Soc. Am. B, 27(6), 1204-1207 (2010)

[37] H. Matsubara, S, Yoshimoto, H. Saito, Y. Jianglin, Y. Tanaka, and S. Noda, “GaN photonic-crystal surface emitting blue-violet wavelengths”, Science, 319, 445-447 (2008)

[38] D. M. Williams, K. M. Groom, B. J. Stevens, D. T. D. Childs, R. J. E. Taylor, S. Khamas, R. A. Hogg, N. Ikeda, and Y. Sugimoto, “Epitaxially regrown GaAs-based photonic crystal surface emitting laser”, IEEE Photon. Technol. Lett., 24(11), 966-968 (2012)

[39] R. J. E. Taylor, D. M. Williams, D. T. D. Childs, B. J. Stevens, L. R. Shepherd, S. Khamas, K. M. Grrom, R. A. Hogg, N. Ikeda, and Y. Sugimoto, “All-semiconductor photonic crystal surface-emitting lasers based on epitaxial regrowth”, IEEE J. Select. Topics Quant. Electron., 19(4), 4900407 (2013)

[40] B. J. Stevens, K. M. Groom, J. S. Roberts, P. W. Fry, D. T. D. Childs, and R. A. Hogg, “Distributed feedback laser employing buried GaAs/InGaP index-coupled grating”, Electron. Lett., 46(15) (2010)

[41] K. M. Groom, B. J. Stevens, P. J. Assamoi, J. S. Roberts, M. Hughes, D. T. D. Childs, R. R. Alexander, M. Hopkinson, A. S. Helmy, and R. A. Hogg, “Quantum well and dot self-aligned stripe lasers utilizing and InGaP optoelectronic

confinement layer", IEEE J. Select. Topics Quant. Electron., 15(3), 819-826 (2009)

[42] M. Yoshida, M. Kawasaki, M. De Zoysa, K. Ishizaki, R. Hatsuda, and S. Noda, "Fabrication of photonic crystal structures by tertiary-butly arsine-based metal-organic vapor-phase epitaxy for photonic crystal lasers", Appl. Phys. Express, 9, 062702 (2016)

[43] M. De Zoysa, M. Yoshida, M. Kawasaki, R. Hatsuda, Y. Tanaka, and S. Noda, "Photonic crystal lasers fabricated by MOVPE based on organic arsenic source", IEEE Photon. Technol. Lett., 29(20), 1739-1742 (2017)

[44] C. Reuterskiöld Hedlund, J. M. De Pina, A. Kalapala, Z. Liu, W. Zhou, and M. Hammer, "Buried InP/airhole photonic-crystal surface-emitting lasers", Phys. Status Solidi A, 218, 2000416 (2021)

[45] L-R. Chen, K-B. Hong, K-C. Huang, C-L. Liu, W. Lin, and T-C. Lu, "Study of epitaxial regrowth process by MOCVD for photonic crystal surface emitting lasers", Cryst. Growth Des., 21(6), 3521 (2021)

[46] M. Razeghi, *Fundamentals of Solid State Engineering*, New York, NY, USA: Springer (2019)

[47] J. I. Goldstein, D. E. Newbury, J. R. Michael, N. W. M. Ritchie, J. H. J. Scott, D. C. Joy, *Scanning Electron Microscopy and X-Ray Microanalysis*, New York, NY, USA: Springer (2018)

[48] D. B. Williams and C. B. Carter, *Transmission Electron Microscopy*, Boston, MA, USA: Springer US (2009)

[49] E. Kapon, F. Reinhardt, G. Biasiol, and A. Gustafsson, “Surface and interface properties of quantum nanostructures grown on nonplanar substrates”, Appl. Surf. Sci., 123, 674 (1998)

[50] G. Biasiol, F. Reinhardt, A. Gustafsson, and E. Kapon, “Self-limiting growth of GaAs surfaces on nonplanar substrates”, Appl. Phys. Lett., 71, 1831 (1997)

[51] M. Schaffer, B. Schaffer, and Q. Ramasse, “Sample preparation for atomic-resolution STEM and low voltages by FIB”, Ultramicroscopy, 114, 62-71 (2012)

[52] L. A. Giannuzzi and F. A. Stevie (Eds.), *Introduction to Focused Ion Beams*, New York, NY, USA: Springer (2005)

[53] J. E. Halpin, R. W. H. Webster, H. Gardner, M. P. Moody, P. A. J. Bagot, and D. A. MacLaren, “An in-situ approach for preparing atom probe tomography specimens by xenon plasma-focussed ion beam”, *Ultramicroscopy*, **202**, 121-127 (2019)

[54] P. E. Batson, N. Dellby, and O. L. Krivanek, “Sub-ångstrom resolution using aberration corrected electron optics”, *Nature*, **418**, 617 (2002)

[55] S. J. Pennycook and P. D. Nellist (Eds.), *Scanning Transmission Electron Microscopy,* New York, NY, USA: Springer (2011)

[56] P. D. Nellist and S. J. Pennycook, “The principles and interpretation of annular dark-field Z-contrast imaging”, *Advances in Imaging and Electron Physics*, **113**, 147 (2000)

[57] R. F. Egeerton, “Electron energy-loss spectroscopy in the TEM”, *Rep. Prog. Phys.*, **72**, 016502 (2009)

Chapter 3 |

Structural Analysis of Epitaxially Regrown AlAs/GaAs PCSELs

This chapter presents a correlative structural and parametric study of GaAs-based photonic crystal surface emitting lasers (PCSELs) containing void/semiconductor photonic crystal (PC) structures embedded by metalorganic vapour-phase epitaxial (MOVPE) regrowth [1,2].

Two devices are presented which, apart from an *in-situ* pre-regrowth thermal processing step, are nominally identical in terms of device structure, photonic crystal definition and fabrication. Two temperature ramp times were investigated in order to find a favourable condition for the retention of the as-etched profile of the PC grating pit. Scanning transmission electron microscope (STEM)-based analysis reveals the extent of mass-transport-induced surface restructuring of the grating pits for each of the ramp conditions. The morphological changes observed point towards a free-energy-minimisation pathway for the initial pit geometry that favours the

formation on low-energy high-Miller index crystal planes, agreeing closely with the results predicted by theoretical modelling of diffusion kinetics for similar systems.

The use of an AlAs/GaAs superlattice (SL) structure during the early stages of regrowth provides time-resolved snapshots of the evolving growth front during photonic crystal infill by providing a strong mass-contrast mechanism in STEM imaging and allows the relationship between differences in local grating crystallography and the geometry of the resulting crystallographic voids to be inferred. Ultimately, void formation is understood to be the result of limited Al mobility under the growth conditions used, crystal-plane-dependent growth and surface diffusion kinetics, and self-shadowing of the growth front from the incident atomic flux as the aspect ratio of the evolving grating aperture increases and the void becomes encapsulated.

The performance of the devices is characterised in terms of the unique void shape obtained in each case, with the device containing larger voids displaying improved threshold current and increased output power. These observations are compared with the results of previous simulation-based studies of PCSELs which predict increased grating coupling strengths and lower optical confinement factors for voids with optimum diameter and height, providing a direct experimental confirmation of the reported trends.

3.1. Motivation

As discussed in Chapter 2, MOVPE-based regrowth represents the ideal method for fabricating PCSELs as it provides additional degrees of freedom in the design of the PC layer. Not only does it offer greater flexibility in terms of material systems than

the wafer bonding techniques previously employed, but it also allows for the realisation of both void-containing and all-semiconductor structures, with GaAs-based devices containing AlGaAs-Void-GaAs [3,4] and GaAs-InGaP [5,6] PCs having been demonstrated previously. In the context of all-semiconductor PCs, use of AlAs as the grating infill material is of interest for high-power applications, as it would provide the largest possible refractive index contrast versus GaAs ($n_{AlAs} = 2.94$, $n_{GaAs} = 3.45$), thereby producing the strongest grating coupling coefficients outside of the Void-GaAs system [7]. To date, however, there have been no reports of devices utilising an AlAs infill in either of the available PC systems. Regardless of whether the desired PC contains voids or not, an understanding of, and control over, the regrowth process is crucial in optimising device performance as properties such as grating coupling strengths, lasing threshold, and output power are dependent on the nano-scale geometry of the PC unit cell [8-12].

An important aspect that must be considered when designing a regrowth process for PCSELs, or any other device with wavelength-selective grating element, is the ability to control the geometry and profile of the PC grating pits, which are designed so as to provide optimal grating coupling values. However, surface restructuring and dimensional changes can occur through mass transport of material caused by thermally promoted diffusion of surface species during pre-growth temperature cycling within the MOVPE reactor [13]. In order to preserve the grating, deposition should begin as soon as the reactor temperature has reached the necessary growth temperature, which should be carefully chosen along with the group-V overpressure and ramp rate in order to minimise diffusion during the temperature ramp [14]. Once deposition has begun, growth conditions such as temperature, growth rate, and V:III

ratio must be chosen to tune the surface mobility of the infill material and achieve the desired degree of grating infill, or control the size and shape of any voids that form [15].

Use of AlAs as the infill material for the PC layer presents a number of possible challenges for device fabrication. Firstly, a growth temperature of 650 °C or higher is generally required for the growth of good quality aluminium-containing layers [16]. This is much greater than the temperature at which mass-transport and diffusion effects are known to affect patterned GaAs materials, typically thought to start between 550 and 600 °C [17]. Currently, it is unknown to what extent mass-transport-induced restructuring will affect the profile of the grating pits at these elevated temperatures, and a strategy for minimising this effect must be developed. Consequently, the initial growth temperature used for deposition must necessarily be limited to the lower bounds of the range for aluminium-containing material in order to minimise pre-growth mass-transport effects. Whilst previous studies have investigated aspects of void-shape engineering during regrowth in the AlGaAs-GaAs PC system [17-19], no similar reports have been made for AlAs and it is unknown to what extent grating infill can be manipulated in this system. Additionally, there is no known baseline set of regrowth conditions for realising epitaxially regrown PCSELs with an embedded AlAs-GaAs PC layer.

This work presents the first investigation of PCSELs utilising AlAs as the PC infill material. In order to assess the effects of mass-transport in this system and find a favourable condition for retention of the as-etched grating profile, two nominally identical devices are presented for which only the pre-growth temperature ramp time is varied, with the growth temperature being reached in either 3 or 6 minutes. The

restructuring of the pits and its subsequent impact on the grating infill process is studied by cross-sectional STEM imaging of the regrown PC layer. An AlAs/GaAs SL structure is used to illustrate the evolution of the growth front during regrowth, and allow for the relationship between the crystallographic geometry of the patterned grating and the mechanism of grating infill to be inferred. The LIV-characteristics and performance of the devices is compared and correlated to the structural analysis of the PC layer in each. This investigation is intended to present a baseline regrowth process against which future device optimisation efforts can be assessed.

	Material	Thickness (nm)	Doping (cm^{-3})	Repeats	
Regrowth	GaAs	100	Zn : 1e19	-	
	$Al_{0.41}GaAs$	750	Zn : 1e18	-	
	$Al_{0.41}GaAs$	750	Zn : 5e17	-	
	GaAs	9	Zn : 5e17	12	PC Layer
	AlAs	1	Zn : 5e17		
	GaAs	5	Zn : 5e17	-	
Base Epitaxy	GaAs	158	Be : 4e17	-	
	GaAs	30	i	-	
	GaAs	31.5	i	3	AR
	$In_{0.265}GaAs$	6.5	i		
	GaAs	60	i	-	
	$Al_{0.2}GaAs$	20	Si : 6e17	-	
	$Al_{0.4}GaAs$	1400	Si : 6e17	-	
	$Al_{0.2}GaAs$	20	Si : 6e17	-	
	GaAs	300	Si : 1e18	-	
	(100) GaAs 2 ° --> (1-10)		Si : 3e18	-	

Figure 3.1. Epitaxial structure of fabricated devices. The base epitaxial material includes an active region (AR) composed of three $In_{0.265}GaAs$/GaAs quantum wells tuned to emit at 1070 nm, and an upper *p*-type GaAs layer which is patterned with the PC grating structure. The PC layer is formed by regrowth with a 12 period AlAs/GaAs superlattice structure, followed by the upper *p*-$Al_{0.41}GaAs$ cladding layer and *p*+-GaAs contact layer.

3.2. Device Design, Regrowth, and Fabrication

The base epitaxial material used for device fabrication was purchased from QD Laser Inc. The base device structure, which is shown in Figure 3.1, was grown by MBE on (100) GaAs wafers with a 2 ° offcut towards $(1\bar{1}0)$ and includes an active region (AR) composed of three $In_{0.265}Ga_{0.735}As$/GaAs quantum wells tuned to emit at 1070 nm, and a top *p*-GaAs layer which forms the basis of the PC [2] The use of substrates with a small-angle offcut in the surface orientation is commonplace in MOVPE in order to increase the density of atomic steps on the wafer surface and promote good-quality growth. The 2° offcut used here is not expected to significantly affect the surface diffusion kinetics over the patterned substrate, nor greatly alter the analysis presented below.

Having been spun with a 1 μm-thick layer of PMMA photoresist, the top GaAs layer was patterned with a square lattice of circular holes using electron beam lithography (EBL) and reactive ion etching (RIE). The PC was designed so as to provide optimal overlap with the emission wavelength of the AR assuming PC atoms composed entirely of AlAs. The total PC area was 150 x 150 μm with the period of the lattice, *a,* set at 320 nm. The holes were etched with a nominal diameter, *2r,* of 256 nm, corresponding to an r/a of 0.4, the value for which the theoretical coupling strength of the PC grating is at a local maximum [9]. The resulting depth, *h,* was approximately 150 nm. Plan-view and cross-sectional SEM images of the as-etched PC layer, shown in Figure 3.2, reveal that the shape of the holes is an inverted truncated cone with sloped sidewalls arising from the use of the PMMA as a soft etch mask [20]. The angle of the sidewalls relative to the bottom of the grating is approximately 55°, indicating that the hole is bounded by a set of $\{111\}$ crystal planes. Full details of the PC grating

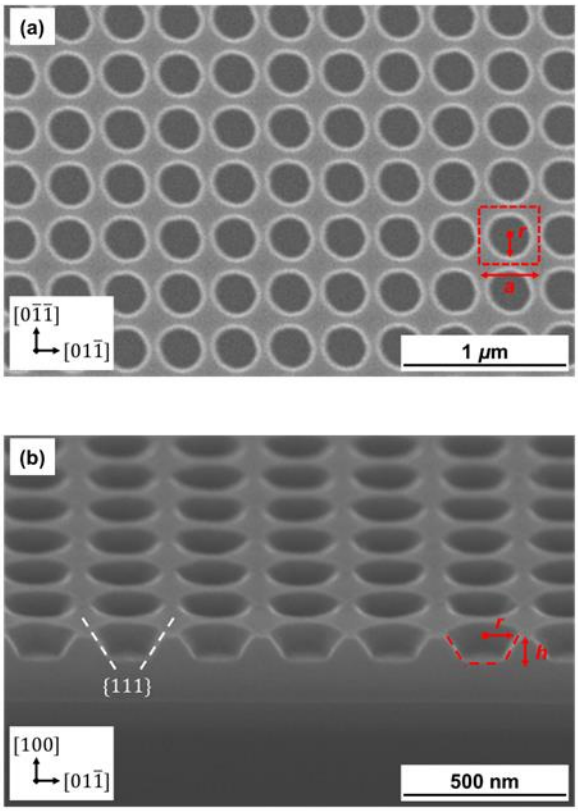

Figure 3.2. Representative (a) plan-view and (b) cross-sectional SEM images of the as-etched PC grating layer prior to regrowth, as viewed along the $[0\bar{1}\bar{1}]$ crystal direction. The PC is composed of a square lattice of circular pits realised by electron beam lithography and reactive ion etching. Unit cell dimensions are labelled in red: a = 320 nm, $2r$ = 256 nm , r/a = 0.4, h = 150 nm. The $\{111\}$ sidewall planes of the pit are highlighted in white in panel b.

fabrication process, including conditions used during the ELB write and RIE processes were unavailable at the time of writing.

Following the etch of the PC grating layer, wafers were prepared for MOVPE overgrowth by UV/ozone cleaning and a one minute etch in a 10:1 buffered HF solution. Regrowth was performed in a Thomas Swan close-coupled showerhead MOVPE reactor operating at a pressure of 100 mbar with hydrogen (H_2) as the carrier gas. Trimethylaluminium (TMAl) and trimethylgallium (TMGa) were utilised as group-

III precursors, with arsine (AsH_3) as the group-V precursor and dimethylzinc (DMZn) as the *p*-dopant source.

As discussed above, the rate of the pre-growth temperature ramp cycle experienced by the wafers prior to the start of regrowth is investigated here in order to assess the extent of thermally promoted mass-transport and grating deformation for this system. As this process is also used as a thermal cleaning and native-oxide desorption step, a condition must be found whereby deformation of the grating is minimized whilst ensuring high-quality growth is still possible. For Device A the ramp was performed over 6 minutes, in line with the standard ramp condition used for growth of planar device structures in this MOVPE reactor, whereas the time was halved to 3 minutes for Device B, with the aim of reducing the extent of any mass-transport present in the system. For both devices, the surface temperature of the wafer was ramped linearly from 330°C to 650°C under a constant AsH_3 flow of 100 sccm. As discussed in Section 3.1 above, a temperature of 650°C was chosen to minimise the effects of mass-transport whilst still ensuring the growth of high-quality AlAs, whilst the large group-V overpressure provided by this AsH_3 flow rate is intended to aid both in the preservation of the grating and in the removal of surface contaminants [13].

In order to illustrate the evolution of the growth front during the PC infill, and to aid in structural analysis, the patterned GaAs layer was first overgrown with 120 nm of an AlAs/GaAs superlattice (SL) structure consisting of 12 periods of alternating layers of AlAs and GaAs with nominal thicknesses of 9 nm and 1 nm, respectively. The inclusion of the thin GaAs layers at well-defined thickness intervals within the infill layer provides a source of mass-contrast when viewed with STEM imaging, allowing

the surface contours during deposition to be seen and the evolution of the growth front to be inferred without significantly altering the AlAs growth kinetics. The growth temperature used was 650 °C, the V:III ratio was 700, and the growth rate was nominally 6 nm/min on the planar (100) surface. Following this, the device structure was completed by the growth of a 1.5 μm thick *p*-$Al_{0.41}GaAs$ cladding layer and a 100 nm thick *p*+-GaAs contact layer, both at a higher growth rate of 18 nm/min.

A schematic of the final device design is shown in Figure 3.3. Following MOVPE regrowth, device fabrication was completed by defining a 100 x 100 μm square mesa in the highly doped *p*+-GaAs contact layer, etched to a depth of 300 nm using a

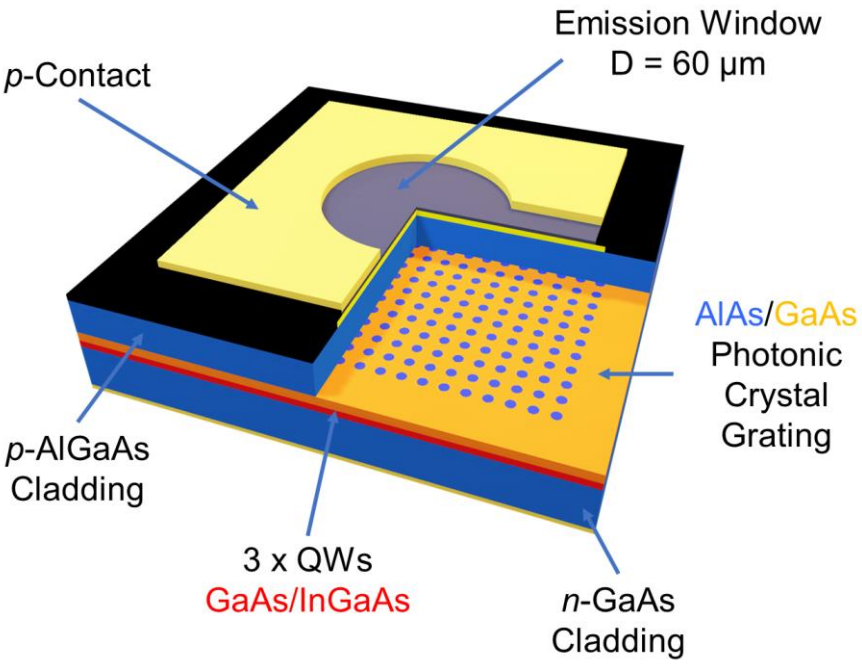

Figure 3.3. Schematic diagram of fabricated devices, with cut-out section showing the location and geometry of the PC grating layer. A 60 μm diameter circular emission window is defined in the 100 x 100 μm^2 *p*-type metal contact.

solution of hydrogen peroxide and orthophosphoric acid. The device surface was then passivated with a 200 nm thick SiO_2 layer and a contact window opened above the mesa using a CHF3/Ar RIE, into which a *p*-type Ti/Pt/Au contact was deposited. A 60 μm diameter circular emission window was defined in the contact by a standard lift off process, and Ti/Au bond pads deposited on the surface. Finally, an *n*-type Ni/Au/Ge/Ni/Au contact was deposited on the backside of the devices.

3.3. Structural Analysis of PC Layer

Following device fabrication and testing, the structure and quality of the regrown PC layers were assessed by scanning transmission electron microscopy (STEM) analysis. Cross-sectional STEM specimens were prepared by a standard lamella lift-out procedure [21] using a Thermo Fisher Helios Xe-plasma dual-beam focused ion beam (PFIB) system equipped with an Easy Lift micromanipulator. The Xe-plasma system was preferred over the more conventional Ga-ion FIB systems in this case so as to avoid the creation of artifacts during sample preparation associated with interactions between the GaAs-based PC system and the Ga-ion beam [22].

STEM specimen preparation was complicated in this case due to the two dimensional and periodic nature of the PC grating, and the absence of morphological features on the surface of the devices post-regrowth that can act as a guide during preparation. For the analysis of regrowth and the grating infill to be accurate, the cross-section should be taken as central to the grating pit as possible. Issues in ensuring a central “cut” are exacerbated by the somewhat random nature in the positioning of the lift-out site. In order to overcome these issues, the cross-sections

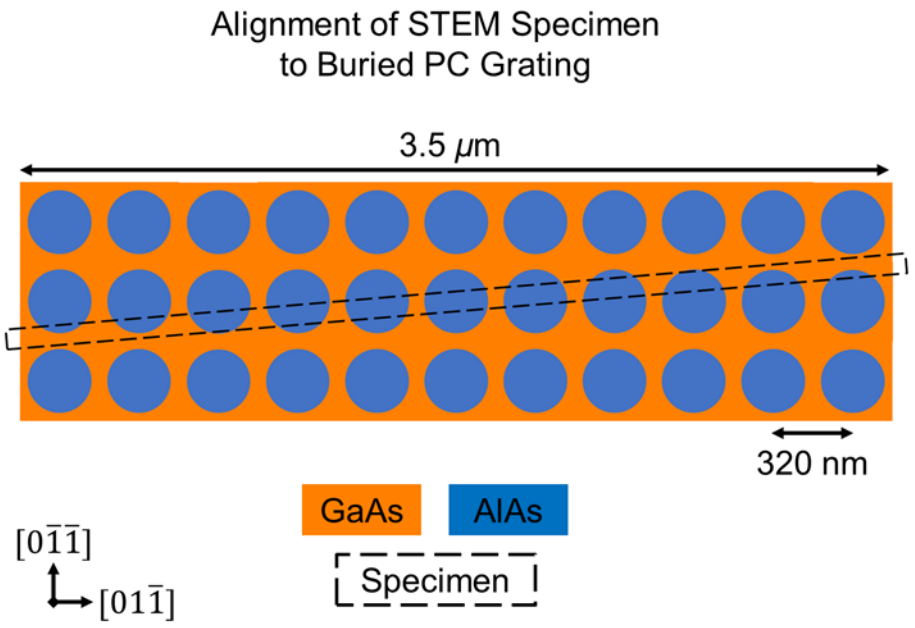

Figure 3.4. Schematic diagram showing the orientation of the STEM lift-out specimen in relation to the underlying PC grating. In order to ensure that the centre point of one or more of the buried grating pits is bisected, the lamella is prepared at an angle of 4.8 ° relative to the in-plane axes of the PC.

were purposely defined at a shallow angle (approximately 4.8 °) relative to the in-plane axes of the PC, as shown in the schematic in Figure 3.4. This creates a "stepping" effect whereby, in an electron transparent section that is 3.5 μm long (approximately 11 PC periods), adjacent grating holes are cut at different positions, with at least one intersecting the near-mid-point of the grating.

Bright field (BF-)TEM and STEM imaging of specimens were performed using a JEOL ARM200cF system operating at 200 kV. Figure 3.5 and Figure 3.6 show cross-sectional (a) BF-TEM, and (b) high-angle annular dark-field (HAADF)-STEM micrographs showing the regrown PC layers of Devices A and B, respectively. Cross-sections are viewed along the [0$\bar{1}\bar{1}$] crystal direction. BF-TEM images show three

periods of the PC, where the intentional stepping effect cause by the method of specimen preparation can clearly be seen – the diffuse nature of the voids on either side of the central feature indicates that these pits have been intersected at a less central position. Contrast in BF-TEM imaging is determined by the intensity of unscattered electrons transmitted through the sample. In this case, the void appear white as there is no material in that region to obstruct the incident beam, so the transmitted intensity is high. The intensity decreases as the atomic mass increases, with the GaAs grating layer appearing darker than the AlAs infill layer. HAADF images show the central void in the BF-TEM images at higher magnifications. In HAADF imaging, signal intensity is dependent on scattered electrons and is approximately proportional to the effective atomic number squared for a given layer with heavier atoms scattering more electrons to higher angles, resulting in a reversal of contrast compared with BF-TEM [23]. The approximately Z^2-dependence of HAADF signal intensity results in greater definition of the now light grey GaAs layers of the SL structure, compared with BF imaging, providing a clear time-resolved snapshot of the growth front as it evolves during infill of the grating pit; this concept is explored further in the sections below.

Importantly, all micrographs show the formation of crystallographic voids in both devices during regrowth of the patterned photonic crystal grating, encapsulated within the SL structure (the central white/black feature in BF/HAADF images, respectively). These voids are present above each of the grating holes and therefore form the basis of the PC in each device owing to the large difference in refractive index between vacuum (n = 1) and semiconductor compared with that between AlAs (n = 2.94) and GaAs (n = 3.45). In the case of Device A, the voids have a cylindrical

"pill"-like shape, are bound by near-vertical $\{011\}$ sidewalls, and have a diameter, *2r'* and height, *h'* of approximately 50 nm and 120 nm, respectively. As such, the PC for this device is defined by an r/a of 0.08, compared to the designed 0.4 r/a of the as-etch grating. In contrast, the voids in Device B are elliptical, or "egg"-shaped, and significantly larger, with a diameter of approximately 110 nm at the widest point, and a height of 155 nm; the nominal r/a for the PC in this case is 0.17. As is explained below, the differences in void geometry seen here are a direct consequence of mass-transport-induced changes in grating profile caused by the different pre-growth temperature ramp conditions used for each device, and the subsequent changes to the dynamics of grating infill.

Additionally, micrographs of both devices reveal the absence of regrowth related defects (such as threading dislocations) emanating from the initial interface at the surface of the GaAs grating layer. This indicates that the substrate surfaces were not adversely affected by excess roughness or contamination following PC definition and hard mask removal, highlighting the quality of the PC etch and pre-MOVPE wafer cleaning processes. Furthermore, the absence of defects at this interface suggests that the effectiveness of the *in-situ* thermal cleaning process experienced by the wafer during the pre-regrowth temperature ramp was not negatively impacted by the use of rapid ramp rates used in this case, confirming that both conditions were sufficient for the removal of native oxide from the wafer surface and the growth of high-quality AlAs infill layers.

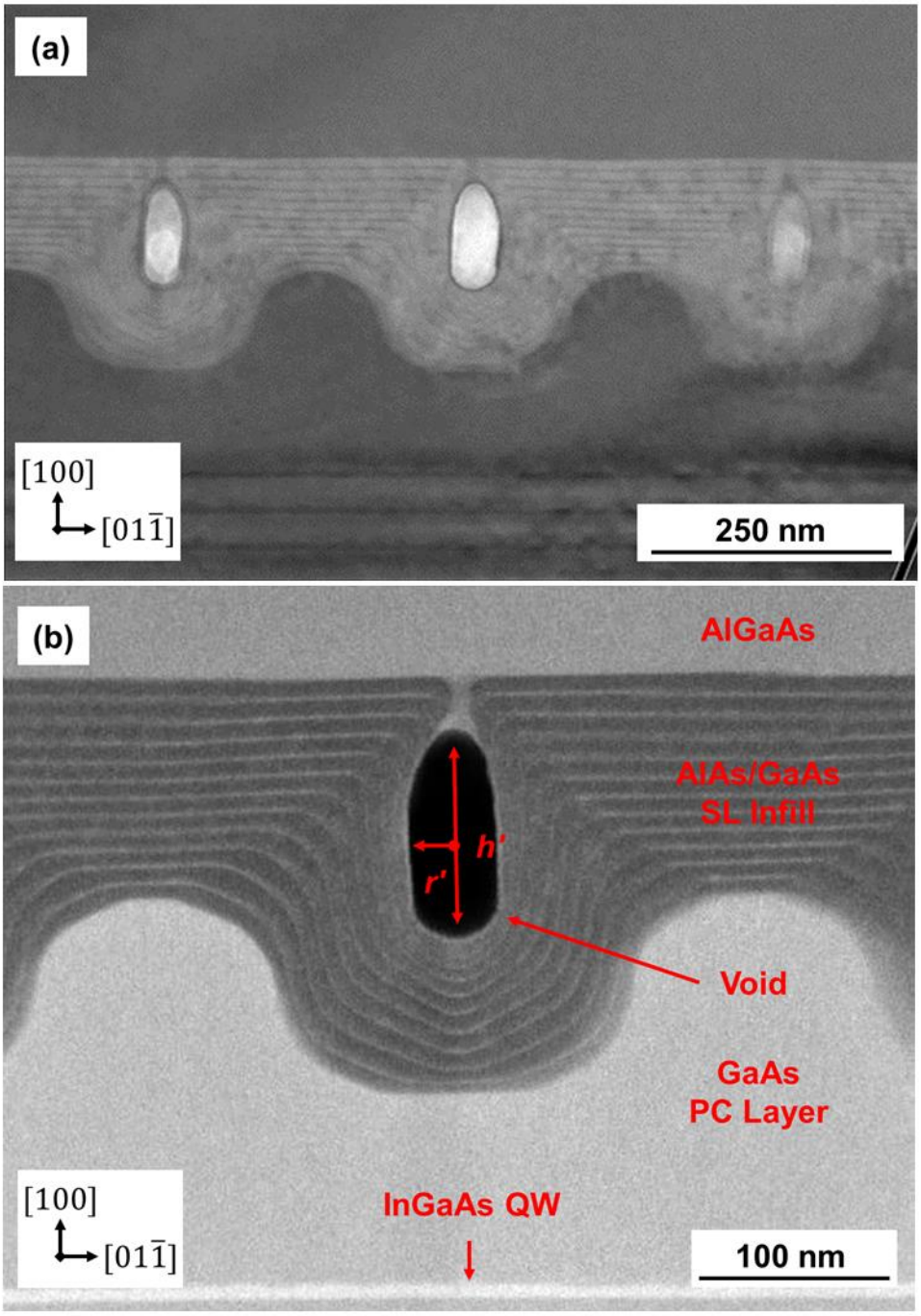

Figure 3.5. Cross-sectional (a) C-TEM and (b) HAADF-STEM images of the regrown PC layer of Device A (6-minute temperature ramp), as viewed along the $[0\bar{1}\bar{1}]$ crystal direction. Crystallographic voids have formed above each of the grating pits during epitaxial regrowth of the patterned GaAs PC layer. The AlAs/GaAs SL structure of the infill layer appears as alternating bands of dark/light material, providing time-resolved snapshots of the growth front as it evolves during deposition. Void dimensions: $2r'$ = 50 nm, r/a = 0.08, h' = 120 nm.

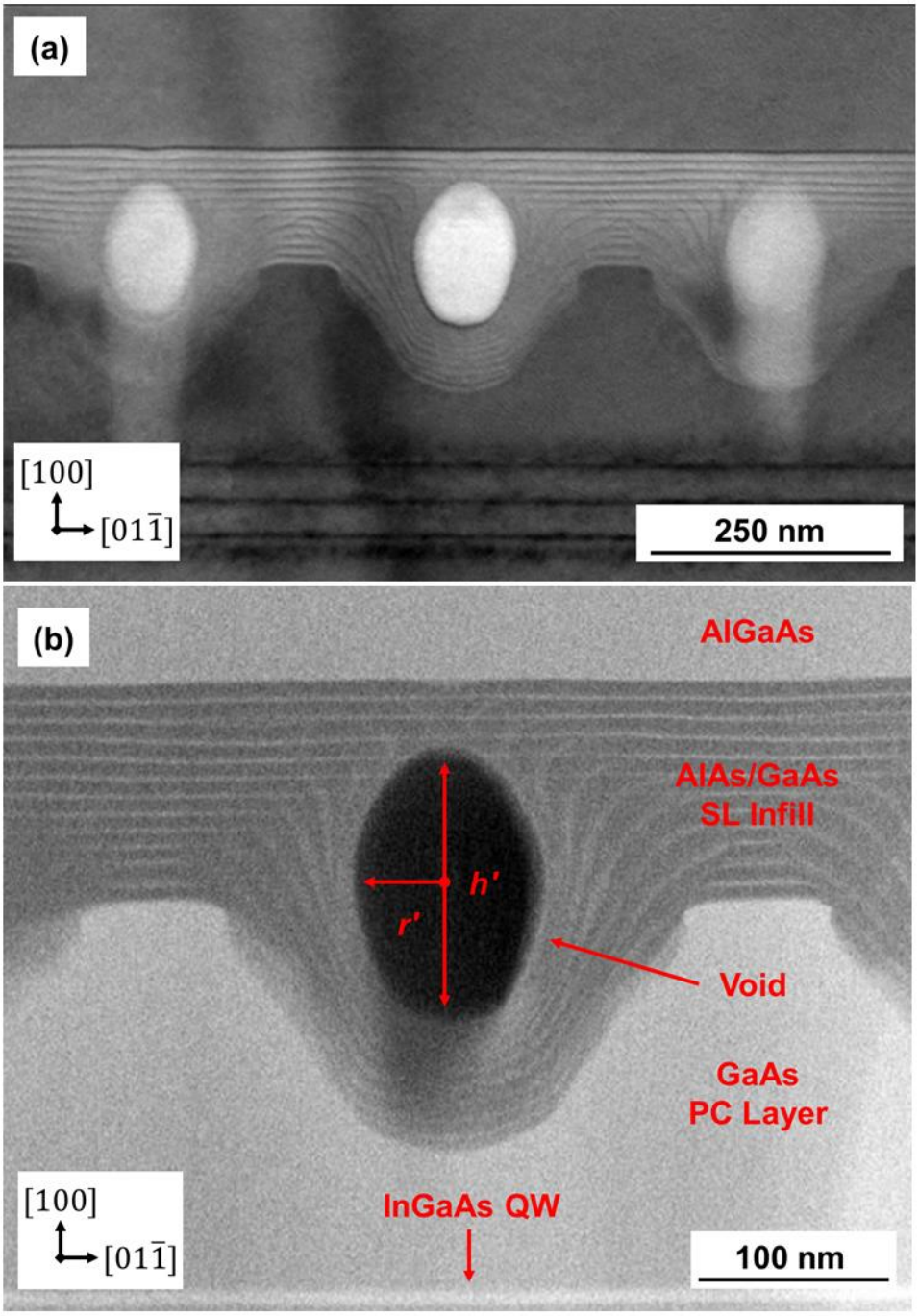

Figure 3.6. Cross-sectional (a) C-TEM and (b) HAADF-STEM images of the regrown PC layer of Device B (3-minute temperature ramp), as viewed along the $[0\bar{1}\bar{1}]$ crystal direction. Crystallographic voids have formed above each of the grating pits during epitaxial regrowth of the patterned GaAs PC layer. The AlAs/GaAs SL structure of the infill layer appears as alternating bands of dark/light material, providing time-resolved snapshots of the growth front as it evolves during deposition. Void dimensions: $2r'$ = 110 nm, r/a = 0.17, h' = 155 nm.

3.4. Effects Pre-Growth Mass Transport

Despite undergoing nominally identical patterning processes at the point of PC etch, it is clear from Figures 3.5 and 3.6 that the grating profiles at the start of regrowth are significantly different for the two devices. The profiles for each device, along with the as-etched profile, are illustrated in the schematic diagram shown in Figure 3.7. The schematic was constructed from the measured pit dimensions in the corresponding HAADF images of the regrown structures and SEM image of the as-etched PC (Figure 3.2(b)), with the Miller indices for each of the planes assigned based on the angle at which they intersect the (100) surface. It follows that these changes are the result of mass-transport within the MOVPE reactor during the temperature ramp stage prior to regrowth. Here the nanometer-scale gradients in chemical potential that are introduced to the wafer by patterning and the exposure of different crystal planes result in thermally activated diffusion of Ga as the system attempts to minimize its surface energy [24].

Whilst the as-etched profile (Figure 3.7, black line) consists of top and bottom (100) planes connected by $\{111\}$-like sidewalls, mass-transport during annealing substantially smooths those seen in the regrown devices. The extent of the diffusion increases with anneal time and is greatest for Device A, which underwent a six-minute temperature ramp. The grating in Device A (Figure 3.7, blue line) is characterized by a reduction in pit depth and overall increase in pit width, which is consistent with a net transfer of material from the sharp, convex edges bounding to upper rim of the grating pits towards the (concave) bottom of the holes. By using the active region as a fiducial marker for measurements we see that the thickness of the GaAs grating layer has not changed, confirming that changes in pit dimensions are

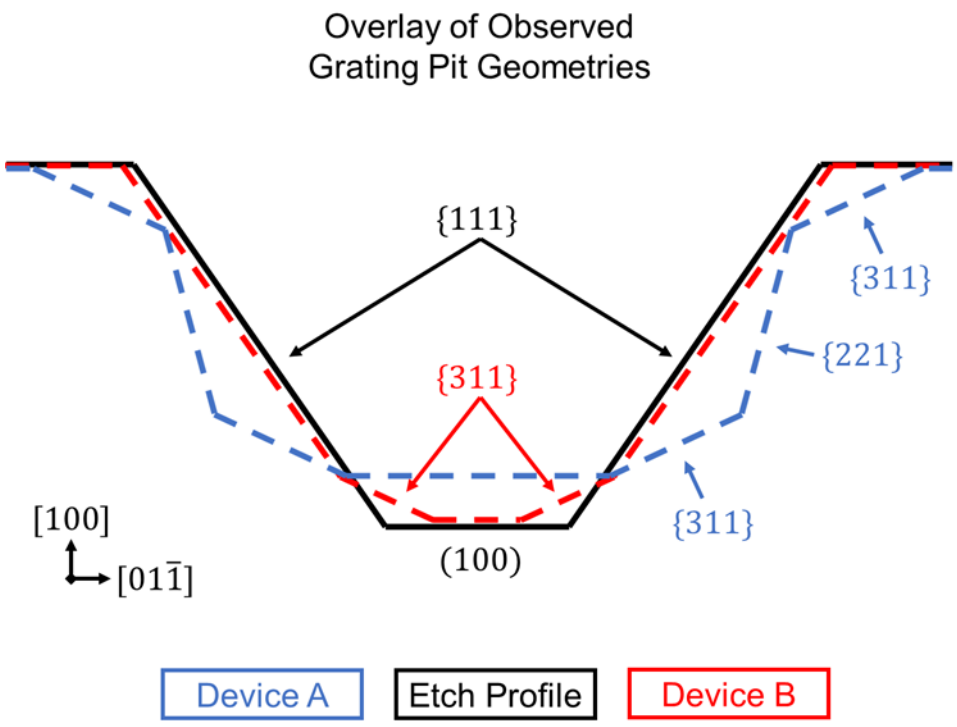

Figure 3.7. Schematic diagram showing the post-temperature ramp PC pit profiles for both devices as observed in STEM images, overlain on the as-etched pre-growth profile (black trace). In Device A (blue trace, six-minute ramp), thermally induced diffusion of material from the convex upper surfaces to the lower concave surfaces of the pit resulted in significant restructuring. The as-etched {111} sidewall planes transition to high-Miller index {311} facets joined by connecting {221} planes, as part of a free-energy minimisation pathway. In Device B (red trace, three-minute ramp), the reduced ramp time was successful in minimising the extent of mass transport, allowing for the retention of the as-etched {111} sidewalls and the introduction of only sort {311} planes at the bottom of the pit.

driven only by a redistribution of material within individual pits. The change in dimensions is accompanied by a significant change in the local crystallography within the hole, with the formation of new planes adjacent to the top and bottom (100) surfaces and the introduction of short connecting sidewalls. On the basis of the STEM analysis (Figure 3.5(b)), the angles at which they intersect the (100) plane are consistent with {311} and {221}-like planes, respectively. The reduced ramp time used for Device B (three minutes), by comparison, resulted in much less diffusion and

only minimal smoothing, characterised by a slight reduction in hole depth and the formation of only short {311}-like planes in the bottom corners of the hole (Figure 3.7, red line).

As is explored more fully in the section below, the introduction of the {311} planes to the pit profile is key in driving the differences in grating infill dynamics for the two devices during regrowth. {311} planes are high-Miller index planes and are therefore more reactive than either {111} planes or the (100) surface owing to a larger density of surface dangling bonds, increasing the sticking probability for arriving species and reducing the diffusion rate of adsorbed species [25].

The morphological changes in grating shape described above share similar characteristics to those seen for regrowth of structures containing V-grooved grating layers. In a similar manner to our case, mass-transport of material from the sharp convex edges at the top of grating to the concave interface between the {111} sidewall panes has been shown to result in significant rounding at the top of the grating layer and the formation of a lower-surface energy (100) plane at the bottom of the groove [26]. It has been shown elsewhere that the degree of mass-transport and smoothing of V-grooves can be reduced, and the formation of the (100) plane prevented, by fast ramping of the reactor temperature in a large group-V overpressure, as was achieved in our experiment [14].

Taken together, the grating profiles seen in our regrown devices can be thought of as forming part of a surface-energy-minimisation pathway which would ultimately lead to complete planarization if not quenched by the subsequent deposition. Whilst, to the best of our knowledge, the crystal plane configurations observed across our

devices have not been previously reported experimentally in the GaAs (or other III-V) system, similar observations have been made in studies of etched pits in (100) Si surfaces. Phase-field computational simulations of thermally-promoted diffusion in this system, in which the pits have a similar starting geometry to our PC grating, have predicted a similar sequence of pit geometries in the early stages of mass-transport, with $\{311\}$ planes emerging as low-energy intermediary sidewall planes facilitating the pathway to complete planarisation [27]. The existence of a potentially predictable sequence of pit geometries for the GaAs PC system raises the interesting possibility for the use of controllable *in-situ* modification as an additional degree of freedom in the design of PCSEL gratings. Whilst, as explained below, the effects of excess mass-transport are, ultimately, detrimental to the performance of devices in the case, it is not unreasonable to assume that exploiting mass-transport could provide a route to accessing more optimal grating geometries where a different initial design is used.

3.5. Growth Front Evolution and Void Encapsulation

As described in Section 3.2, the devices were initially regrown with an AlAs/GaAs SL structure in order to aid structural analysis and highlight the evolution of the growth front during PC infill. This effect is illustrated in the STEM images in Figure 3.5 & 3.6, where the strong mass-contrast provided by successive light-grey GaAs layers of the SL highlights the contours of the growth front and provides a series of time-resolved snapshots as the deposition process proceeds. This allows us to infer information

about the mechanism of void formation and the dynamics of grating infill, and explain the void geometry seen for each device.

It is clear from Figure 3.5(b) that the growth front in Device A evolves through substantial lateral growth of the top (100) plane, with an accompanying reorientation and lengthening of the pit sidewalls toward the vertical $\{011\}$ facets which bound the void. This mechanism contrasts with that seen during the growth of V-groove quantum wires [28] and pyramidal quantum dots [29] in which the original etch profile is retained by subsequent layers in what is termed "self-limited" growth. In the case of AlGaAs/GaAs quantum wires, the nanostructures derive from an enhanced growth rate on the trench sidewalls driven by diffusion of species from the (100) surface plane, allowing for the complete planarization of the patterned area without the formation of voids [30]. In contrast, we attribute the dynamic evolution of the growth front and void formation in the PC system to restricted diffusion of adsorbed species from the upper surfaces of the pit, and a reduced local growth rate on planes at the bottom of the pit.

In the case of Device A, aluminium adatoms diffusing from the upper (100) surface into the pit encounter higher-Miller index $\{311\}$ planes. These planes have a more open bonding structure with a greater density of atomic steps and terraces than the (100) surface, resulting in a higher sticking probability and lower adatom diffusion lengths [31]. This leads to an accumulation of species, and hence apparently thicker SL periods on the slow diffusion bounding facets. It is known that aluminium has an inherently lower mobility compared to GaAs or AlGaAs [32], and lower diffusion lengths on more open, higher Miller index surfaces is expected, preventing adatoms from fully diffusing to the lower facets of the pit. The limited surface

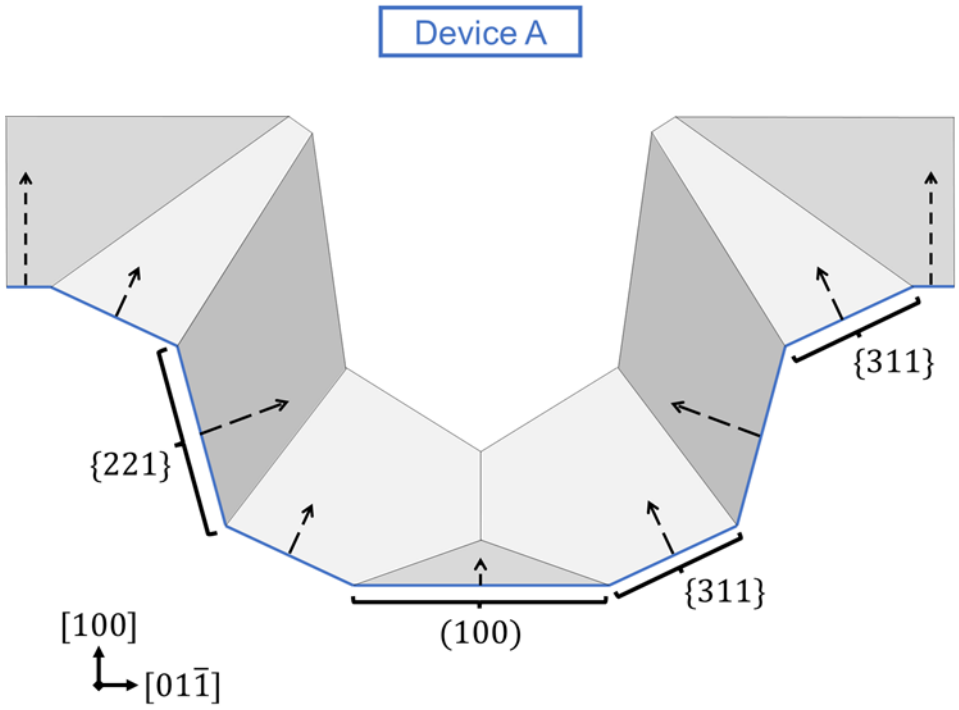

Figure 3.8. Schematic diagram showing the evolving growth front in Device A during the initial stages of grating infill. The first seven GaAs SL layers seen in the corresponding STEM image were used as a guide to the shape of the front. A single domain emanates from each crystal plane of the initial pit profile (blue line); arrows point in plane direction. The evolution is characterised by substantial lateral growth of the upper (100) surface, accompanied by a reorientation of the $\{221\}$ sidewall planes towards the vertical $\{011\}$ facets that bound the void in this case. This reorientation is mediated by the high growth rate upper $\{311\}$ planes which shrink over time and are eliminated from the growth front before the void is encapsulated.

mobility is further suppressed by the use of a relatively low growth temperature and large V/III ratio, which have been shown to impede the diffusion of group-III species across similarly patterned substrates [33].

The evolving growth front seen in Device A is illustrated in the cross-sectional schematic shown in Figure 3.8. This diagram was constructed from the STEM image in Figure 3.5(b) using the seventh GaAs SL layer as a guide to the shape of the growth front after approximately 12 minutes of deposition, before the voids were fully

encapsulated. It is intended to more clearly detail the influences of the initial pit profile on the regrowth dynamics. The growth front has been simplified to remove the curved interfaces between planes, and a single domain emanating from each of the crystal planes that form the underlying pit (blue line) is highlighted; dashed arrows indicate the surface normal for each plane. Here we see that the lateral growth of the top (100) surface and sidewall re-orientation are accompanied by shrinkage, and eventual elimination, of the upper $\{311\}$ planes, which is a well-observed characteristic of high-growth rate crystal planes at the convex contours in patterned systems [34]. The individual SL layers seen in the STEM image of Device A are clearly resolved, allowing for direct measurement of individual layer thicknesses. Measurements of the relative growth thicknesses normal to each plane, shown in Figure 3.9, reveal substantially thicker layers on $\{311\}$ facets compared to the adjacent (100) surface. In addition, a significantly reduced layer thickness is observed for the lower compared with upper $\{311\}$ planes. This supports our assessment that whilst diffusion of material from the (100) surface into the pit is occurring in this system, it is limited by the short diffusion lengths on $\{311\}$ planes, preventing it from reaching the lower surfaces of the pit.

The difference in growth rate between the upper and lower $\{311\}$ planes is what drives the reorientation and lengthening of the $\{221\}$ pit sidewall planes towards the $\{011\}$ facets that bound the void. The difference is exacerbated by additional two factors. The first of these is natural self-shadowing effects, whereby the surfaces at the bottom of the pit experience a reduced atomic flux impinging on them from the vapour phase, reducing their effective local growth rate compared with the upper surfaces [35]. This is demonstrated in Figure 3.10. which shows the relative thickness

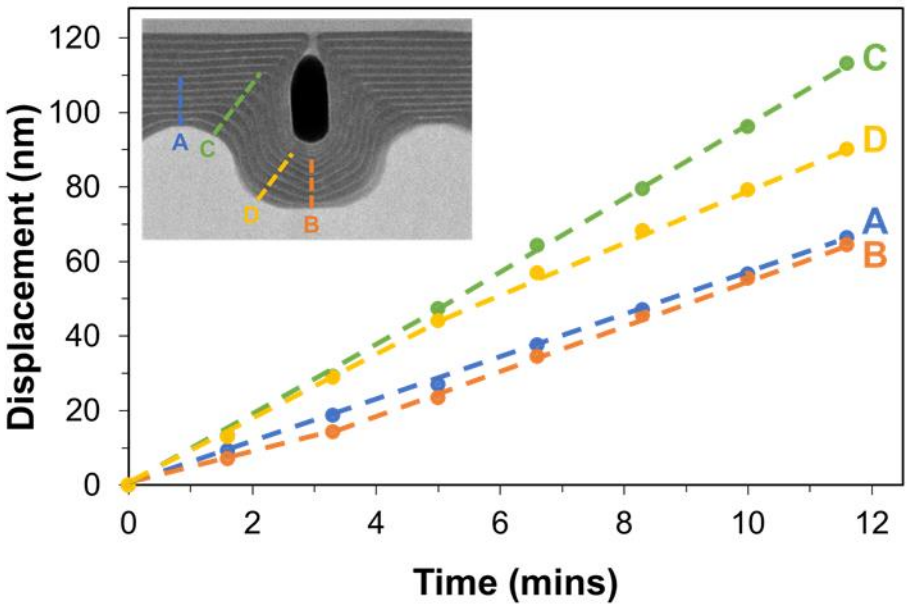

Figure 3.9. Displacement of the growth front normal to the (upper/lower) (100) (A/B) and $\{311\}$ (C/D) planes in Device A during the first seven periods of the SL infill structure. The $\{311\}$ planes display a larger effective growth rate compared to the adjacent (100) surfaces, indicating a net diffusion of material onto these planes. Additionally, the effective growth rate of the upper $\{311\}$ planes is significantly higher than the lower, indicating that there is limited diffusion of material from the upper to lower planes.

of deposition on the upper and lower (100) surfaces across the entire void encapsulation process. In the first instance, there is little divergence in the growth rates of the upper and lower surfaces; however, following the elimination of the $\{311\}$ planes from the growth front and the introduction of the bounding $\{011\}$ facets, there is a sharp drop in the amount of material deposited in the bottom on the pit. At this point, the aspect ratio of the aperture through which the incident atomic flux passes is large and vapour-phase deposition on the lower surfaces is effectively eliminated. The second factor compounding the difference in growth rate is the

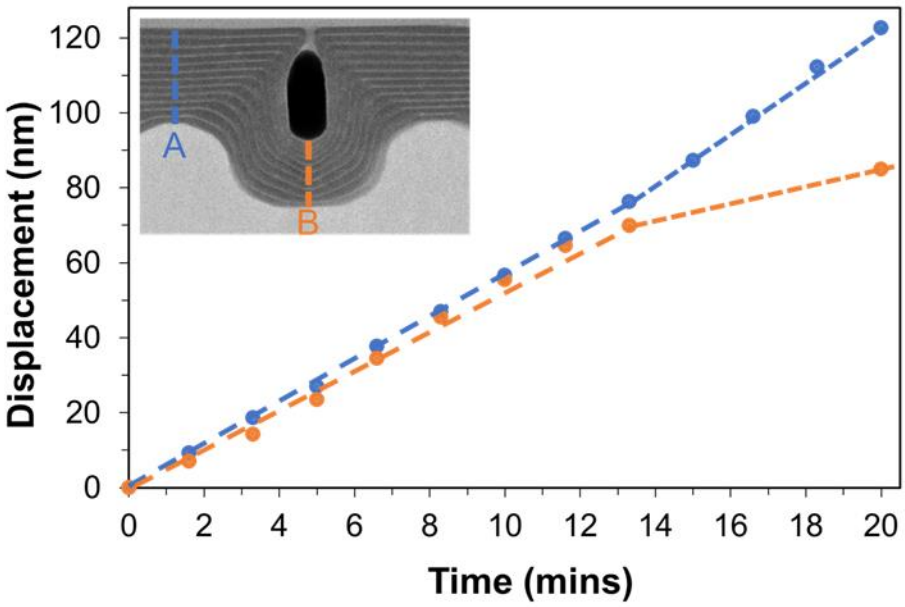

Figure 3.10. Displacement of the growth front normal to the (upper/lower) (100) (A/B) planes in Device A during the entirety of the SL infill structure. Little divergence Is observed in the effective growth rates of the upper and lower surfaces until the formation of the $\{011\}$ facets that bound the void after the seventh SL period (approximately 14 minutes). At this point the large aspect ratio of the pit aperture exacerbates natural self-shadowing effects resulting in a significant drop in the effective growth rate within the pit as the lower planes are shielded from the incident atomic flux.

inherently low surface mobility of aluminium adatoms in the system, which further supresses diffusion of material from the upper planes to the lower surfaces of the pit.

Ultimately the void is formed following the elimination of the top $\{311\}$ planes from the growth front and the merging of the (100) plane which forms overhangs at the interface with the $\{011\}$ sidewall facets. At this point, lateral growth of the (100) plane dominates over deposition within the large-aspect-ratio hole, allowing the void to be encapsulated without further reduction in diameter. We note that, in this case, the void is ultimately enclosed by the AlGaAs cladding layer, as seen in Figure 3.5.

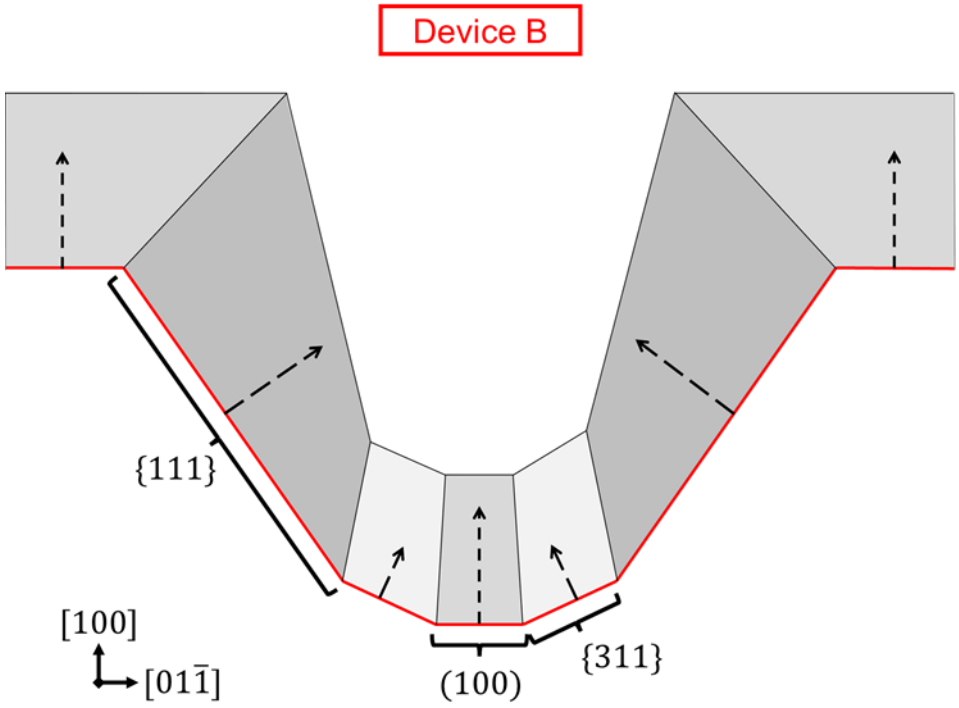

Figure 3.11. Schematic diagram showing the evolving growth front in Device B during the initial stages of grating infill. The first seven GaAs SL layers seen in the corresponding STEM image were used as a guide to the shape of the front. A single domain emanates from each crystal plane of the initial pit profile (red line); arrows point in plane direction. The growth front is characterised by a non-uniform thickness on the $\{111\}$ sidewall planes, with a larger effective growth rate at the interface with the upper (100) surface. This non-uniformity drives the lateral growth of the (100) surface that leads to the encapsulation of the void.

This is the result of enhanced growth within the hole compared to Device B, which pushes the position of the void closer to the AlAs/GaAs-AlGaAs interface.

As discussed in Section 3.4, the 50% reduction in temperature ramp time compared with Device A was successful in reducing the extent of Ga mass-transport, resulting in the retention of the $\{111\}$-like grating sidewalls defined at the etch stage. The evolution of the growth front observed in Device B is illustrated in the schematic diagram shown in Figure 3.11. Exact quantification of the sidewall SL layer thicknesses is limited because the layers appear less distinct, which we attribute to

the relative thickness of the STEM cross-section: the projection of a curved, three-dimensional structure onto a two-dimensional image. However, there is a clear non-uniformity in the overall thickness of the $\{111\}$ sidewall planes, with enhanced effective growth rate at the interface of the upper (100) surface. This effect is consistent with that seen in the regrowth of V-groove structure at lower temperatures and large V/III ratios [33], for which the mobility of the group III-species is supressed, preventing them from diffusing along $\{111\}$ planes and incorporating on the lower surfaces if the pit. In the case of Device B, it is this "bunching" of material at the upper edges of the pit drives the lateral growth of the (100) planes that results in void encapsulation, confirming the importance of suppressed adatom mobility in driving void formation during the regrowth process.

3.6. Analysis of Device Parametric Performance

The parametric performance of the devices were probed under quasi-continuous wave (CW) conditions at 20°C using a pulse width of 2 μs and a 1 % duty cycle. The LIV and spectral characteristics of both A and B are shown in Figure 3.12.

Lasing occurred for Device A at a threshold current of 440 mA (J_{Th} = 4.4 kA/cm^2) and a wavelength of 1074 nm. In addition, the device suffered from a low slope efficiency with an output power, P_{Out}, of only 64 pW recorded at 600 mA. The poor performance of the device can be attributed to the size of the PC voids. Previous simulation-based studies of square-lattice PCs consisting of circular holes have reported that local maxima in the in-plane coupling coefficient are obtained when the r/a is either 0.2 and 0.4 [9]. The sub-optimal r/a of 0.07 for the voids in Device

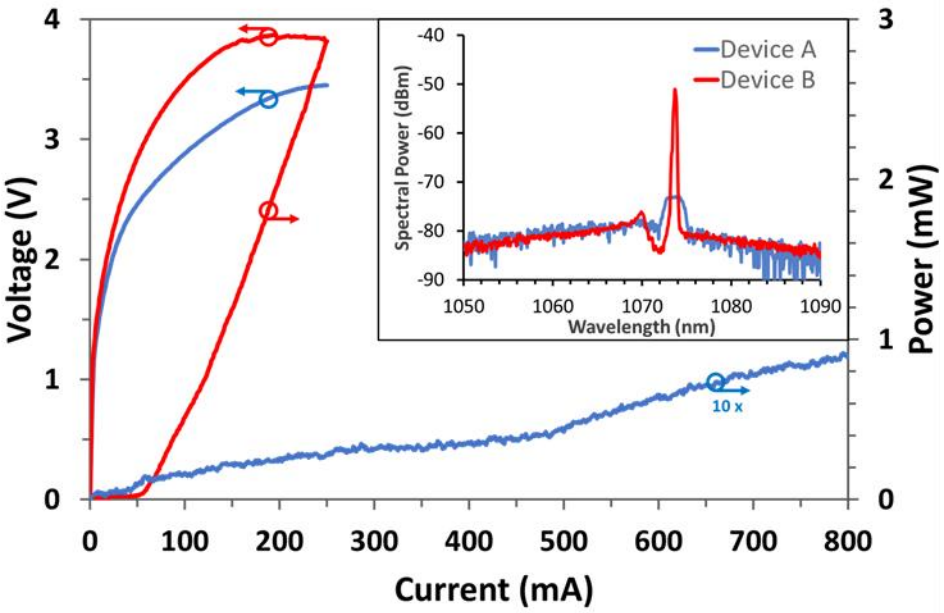

Figure 3.12. LIV and spectral characteristics (inset) of both devices, as measured under quasi-CW conditions at 20 °C (2 μs pulse width, 1 % duty cycle). Lasing occurred for both devices at 1074 nm. Device B (red trace) displayed a significantly reduced J_{Th} = 0.65 kA/cm^2 and improved P_{Out} = 2.8 mW @ 250 mA compared with Device A (red trace).

A are therefore associated with large values of in-plane loss and, in turn, large threshold current and low slope efficiency for the vertically emitted light. Similarly, it has been shown that, for a given r/a, maximum output power is achieved when the void height is equal to half of the grating period [11]. In this case the height is only 75% of the optimum value of 160 nm, and so the output power is further diminished due to destructive interference of light scattered out of plane.

Device B displayed significantly improved laser performance over A, with an order of magnitude reduction in threshold current to 65 mA (J_{Th} = 0.65 kA/cm^2) and a measured output power of 2.8 mW at 250 mA. The associated slope efficiency is

0.012 W/A, however it should be noted that light is collected from an aperture of only 28 % of the total pumped area due to absorption of light in the top gold contact. The optical spectrum of the device (Figure 3.12, inset) is characterised by a main lasing peak centred at 1074 nm, with a less intense peak at a shorter wavelength owing to the narrow splitting of bands at the Γ_2-point of the photonic band structure. The dip in the spectrum between these peaks corresponds to the position of the local band gap for this PC structure. The improvements in threshold and output power can be attributed to the reduction of parasitic in-plane loss, through an increase in grating coupling strength, and decrease in vertical destructive interference associated with improved void radius (0.17 r/a) and height (155 nm), respectively, in line with the predictions of the simulation-based studies mentioned above [9,11].

Whilst the use of an AlAs/GaAs superlattice has proved to be a useful method for highlighting the evolving growth front for STEM analysis, its presence almost certainly has a detrimental effect on the electrical characteristics of the devices, leading to an increased forward voltage compared with a device grown with a bulk infill layer. The increase in forward voltage seen for Device B compared to Device A can be, in part, attributed to the increased void size, with the decrease in effective conduction cross-section for carriers moving through the PC layer resulting in a larger effective resistance for this structure, indicating a possible trade off when attempting optimising both the electrical properties of the device and the coupling strength of the PC grating.

3.7. Discussion & Future Work

The purpose of the investigation presented in this chapter was to study the effects of mass transport on the PC grating layer and determine a condition for the pre-growth temperature ramp rate that best allowed for the retention of the as-etched pit profile. Of the conditions investigated, the faster, three-minute ramp time used for Device B proved most effective in minimizing the extent of mass transport, with the pits retaining their initial $\{111\}$ sidewall planes. Surface restructuring was not eliminated completely, however, as evidenced by the short $\{311\}$ planes that form at the bottom surface of the pit. In the context of all-semiconductor PC structures, future work should focus on fully eliminating excess diffusion in the pre-growth stage in order to prevent deviation from the designed coupling strength of the PC grating. The main process parameters that could be leveraged to achieve this are either an increase in the arsine overpressure or the use of a more aggressive temperature ramp rate. At this point, however, it is unclear whether a shorter ramp time would be effective in completely eliminating mass-transport, or whether a further reduction would have deleterious effects on the thermal cleaning of the wafer surface and the overall quality of the infill material. In addition, a shorter ramp time may result in reduced control over the stability of the reactor temperature during the initial stages of grating infill, potentially impacting the regrowth kinetics. Ultimately, attempts to minimise mass-transport in the AlAs/GaAs PC system could be limited by the high growth temperature required, and a shift away from high temperature AlAs to lower temperature AlGaAs as the infil material may be required to optimize this part of the process.

In both devices, regrowth resulted in crystallographic voids being encapsulated within the PC layer. The use of the AlAs/GaAs SL structure proved highly effective in illustrating the evolution of the growth front during grating infill and allowed for the relationship between the void geometry and the crystallography of the underlying grating pits to be understood. Whilst the void shape is dictated to a great extent by the growth and diffusion kinetics of the individual crystal planes in the pit, the key aspects driving void formation are the same in both cases. Voids are formed by the lateral growth and coalescence of the upper (100) surface over the pit opening. The lateral growth is driven by low adatom surface mobility which prevents the diffusion of material from the upper to the lower surfaces. This is compounded by self-shadowing effects which shield the lower planes from the incident atomic flux, reducing their effective growth rate.

These insights provide a number of avenues for future work when considering optimised regrowth processes for PCSELs. In the pursuit of an all-semiconductor PCSEL in the AlAs/GaAs system, growth conditions must be tuned so as to provide higher adatom mobility in the infill layer and promote greater diffusion of material into the grating pit. This could primarily be achieved through the use of a higher growth temperature, or through the reduction in the growth rate and V/III ratio, which would likely resulting in smaller voids (and potentially resulting in complete infilling in the case of Device A). In reality however, it is likely that the process window for the growth temperature in this system is limited as the increased temperatures required from higher adatom mobility (> 650 °C) would have detrimental effects on the ability to control pre-growth mass transport effects. An alternative route for achieving an all-semiconductor device would be the use of

AlGaAs as the infill material, which is known to have an inherently greater adatom surface mobility than AlAs. In the context of void-containing PCSELs, a change in infill material may also prove beneficial as the milder temperatures required for growth of AlGaAs may provide a larger process window in which the regrowth conditions and adatom surface mobility can be tuned, potentially allowing for a wider range of void geometries to be realised. The use of AlGaAs as an infill material, and the effects of increased adatom mobility on the formation of voids during PC regrowth is explored in the Chapter 4.

Finally, whilst the use of STEM imaging has been shown to be a highly effective tool in revealing the role of crystal plane and growth kinetics in the formation of voids and in dictating their geometries, it is noted that the small sampling volume of this technique (together with the method of specimen preparation used in this work) necessarily limits analysis to on-the-order-of one PC periods per lamella. Whilst the analysis of kinetic processes presented in this work is unlikely to greatly differ between adjacent PC pits, the key dimensions of voids (as well as, perhaps, some subtleties of their geometry) are expected to vary to some degree across the PC region owing to natural variations in the EBL and RIE processes over such large areas (150 x 150 μm^2, approximately 200'000 individual grating pits). Such variations are likely to affect the coherence of the PC cavity and negatively impact the performance of real devices, therefore future work regarding optimisation of fabrication processes for PCSELs should consider attempts to quantify the uniformity of voids (and, indeed, the underlying grating pits) over large areas using techniques with more suitable sampling volumes such cross-sectional scanning electron microscopy and (in the case of PC pits prior to regrowth) plan-view atomic force microscopy.

3.8. Conclusion

This chapter has presented a corelative structural and parametric study of MOVPE-regrown GaAs-based PCSELs containing void-based PC layers. The effect of pre-growth mass-transport on the grating pit profile was analysed for two devices for which the pre-growth temperature ramp time was varied. Through STEM imaging of the regrown devices, it was shown that a three-minute ramp time resulted in minimal diffusion induced restructuring of the pit and good retention of the as-etched profile with $\{111\}$ sidewall planes. In contrast to this, significant morphological changes were observed for a six-minute temperature ramp, with the introduction of high-index $\{311\}$ crystal planes as part of a free-energy minimisation scheme.

When combined with the use of an AlAs/GaAs SL structure during regrowth, STEM imaging allowed for the evolution of the growth front to be observed, and the relationship between the underlying pit profile and the resultant void geometries to be inferred. Ultimately, void formation was attributed to rapid lateral growth of the upper (100) surface driven by the limited diffusion of adatoms from the upper to lower regions of the pit. The presence of high-growth rate $\{311\}$ planes at the upper regions of the growth front resulted in the formation of small “pill” shape voids, whilst the retention of the initial $\{111\}$ sidewall planes resulted in much larger “egg” shaped voids with more desirable dimensions for use in devices. The device containing voids with a larger volume exhibited greatly improved threshold current and output power, which is attributed to increased in-plane coupling within the PC and reduced destructive interference of light scattered out-of-plane, confirming the results of previous simulation-based studies.

3.9. References

[1] A. F. McKenzie, B. C. King, K. J. Rae, S. Thoms, N. D. Gerrard, J. R. Orchard, K. Nishi, K. Takemasa, M. Sugawara, R. J. E. Taylor, D. T. D. Childs, D. A. MacLaren, and R. A. Hogg, "Void engineering in epitaxially regrown GaAs-based photonic crystal surface emitting lasers by grating profile analysis", Appl. Phys. Lett., 118, 021109 (2021)

[2] B. C. King, K. J. Rae, A. F. McKenzie, A. Boldin, D-H. Kim, N. D. Gerrard, G. Li, K. Nishi, K. Takemasa, M. Sugawara, R. J. E. Taylor, D. T. D. Childs, and R. A. Hogg, "Coherent power scaling in photonic crystal surface emitting laser arrays", AIP Advances, 11, 015017 (2021)

[3] K. Hirose, Y. Liang, Y. Kurosaka, A. Watanae, T. Sugiyama, and S. Noda, "Watt-class high-power, high-bem-quality photonic-crystal lasers", Nature Photon., 8, 406-411 (2014)

[4] M. Yoshida, M. De Zoysa, K. Ishizaki, Y. Tanaka, M. Kawasaki, R. Hatsuda, B. Song, J. Gelleta, and S. Noda, "Double-lattice photonic-crystal resonators enabling high-brightness semiconductor lasers with symmetric narrow-divergence beams", Nature Mater., 18, 121-128 (2019)

[5] D. M. Williams, K. M. Groom, B. J. Stevens, D. T. D. Childs, R. J. E. Taylor, S. Khamas, R. A. Hogg, N. Ikeda, and Y. Sugimoto, "Epitaxially regrown GaAs-based photonic crystal surface-emitting laser", IEEE Photon. Technol. Lett., 24(11), 966-968 (2012)

[6] R. J. E. Taylor, D. M. Williams, D. T. D. Childs, B. J. Stevens, L. P. Shepherd, S. Khamas, K. M. Groom, R. A. Hogg, N. Ikeda, and Y. Sugimoto, "All-

semiconductor photonic crystal surface emitting lasers based on epitaxial regrowth", IEEE J, Sel. Top. Quant. Electron., 19(4), 4900407 (2013)

[7] T. S. Lewis-Roberts, "Strain balancing of self-assembled InAs/GaAS quantum dots grown by metal-organic vapour phase epitaxy", PhD Thesis, University of Sheffield (2018)

[8] K. Ishizaki, M. De Zoysa, and S. Noda, "Progress in photonic-crystal surface-emitting lasers", Photonics, 6, 96 (2019)

[9] R. J. E. Taylor, D. M. Williams, J. R. Orchard, D. T. D. Childs, S. Khamas, and R. A. Hogg, "Band structure and waveguide modelling of epitaxially regrown photonic crystal surface-emitting lasers", J. Phys. D: Appl. Phys., 46(26) 264005 (2013)

[10] Y. Kurosaka, K. Sakai, E. Miyai, and S. Noda, "Controlling vertical optical confinement in two-dimensional surface-emitting photonic-crystal lasers by shape of air holes", Opt. Express, 16(22), 18485 (2008)

[11] S. Iwahashi, K. Sakai, Y. Kurosaka, and S. Noda, "Air-hole design in a vertical direction for high-power two-dimensional photonic-crystal surface-emitting lasers", J. Opt. Soc. Am. B, 27(6), 1204-1207 (2010)

[12] C. Peng, Y. Liang, K. Sakai, S. Iwahashi, and S. Noda, "Coupled-wave analysis for photonic crystal surface emitting lasers on air holes with arbitrary sidewalls", Opt. Express, 19(24), 24672 (2011)

[13] R. Bhat, M. A. Koza, C. E. Zah, C. Caneau, C. C. Chang, S. A. Schawrtz, A. S. Gozdz, P. S. D. Lin, and A. Yi-Yan, "A novel technique for the preservation of

gratings in InP and InGaAsP and for the simultaneous preservation of InP, InGaAs, and InGaAsPin OMCVD", J. Cryst. Growth, 107, 871-877 (1991)

[14] P. Dasté, Y. Miyake, M. Cao, Y. Miyamoto, S. Arai, Y. Suematsu, and K. Furuya, "Fabrication technique for GaInAsP/InP quantum wire structures by LP-MOVPE", J. Cryst. Growth, 93, 365-369 (1988)

[15] C. Reuterskiöld Hedlund, J. M. De Pina, A. Kalapala, Z. Liu, W. Zhou, and M. Hammer, "Buried InP/airhole photonic-crystal surface-emitting lasers", Phys. Status Solidi A, 218, 2000416 (2021)

[16] R. Bhat, E. Kapon, D. M. Hwang, M. A. Koza, and C. P. Yun, "Patterned quantum well heterostructures grown by OMCVD on non-planar substrates: applications to extremely narrow SQW lasers", *J. Cryst. Growth*, **93**, 850-856 (1998)

[17] M. Yoshida, M. Kawasaki, M. De Zoysa, K. Ishizaki, R. Hatsuda, and S. Noda, "Fabrication of photonic crystal structure by tertiary-butyl arsine-based metal-organic vapor-phase epitaxy for photonic crystal lasers", *Appl. Phys. Express*, **9**, 062702 (2016)

[18] M. De Zoysa, M. Yoshida, M. Kawasaki, K. Ishizaki, R. Hatsuda, Y. Tanaka, and S. Noda, "Photonic crystal lasers fabricated by MOVPE based on organic arsenic source", IEEE Photon. Technol. Lett., 29(20, 1739-1742 (2017)

[19] K. J. Reilly, A. Kalapala, S. Yeom, S. J. Addamane, E. Renteria, W. Zhou, and G. Balakrishnan, "Epitaxial regrowth and hole shape engineering for photonic crystal surface emitting lasers (PCSELs)", J. Cryst. Growth., 535, 125531 (2020)

[20] K. Kennedy, K. M. Groom, and R. A. Hogg, “Fabrication of v-groove gratings in InP by inductively coupled plasma etching with SiCl4/Ar”, Semicond. Sci. Technol., 21, L1-L5 (2006)

[21] M. Schaffer, B. Schaffer, and Q. Ramasse, “Sample preparation for atomic-resolution STEM and low voltages by FIB”, Ultramicroscopy, 114, 62-71 (2012)

[22] J. E. Halpin, R. W. H. Webster, H. Gardner, M. P. Moody, P. A. J. Bagot, and D. A. MacLaren, “An in-situ approach for preparing atom probe tomography specimens by xenon plasma-focussed ion beam”, *Ultramicroscopy*, **202**, 121-127 (2019)

[23] S. J. Pennycook and L. A. Boatner, “Chemically sensitive structure-imaging with a scanning electron microscope”, *Nature*, **336**(8), 565-567 (1988)

[24] E. Pelucchi, S. T. Moroni, V. Dimastrodonato, and D. D. Vvedensky, “Self-ordered nanostructure on patterned substrates”, J. Mater. Sci.: Mater. Electron., 29, 952-967 (2018)

[25] L. Hofmann, A. Knauer, I. Rechenberg, M. Weyers, and W. Stolz, “Patterned growth of (AlGa)As using metalorganic vapor-phase epitaxy”, J. Cryst. Growth, 206, 255 (1999)

[26] S. N. G. Chu, T. Tanbun-Ek, R. A. Logan, J. Vandenberg, P. F. Sciortino Jr., P. Wisk, and T. L. Pernell, “Grating overgrowth and defect structures in distributed-feedback-buried heterostructure laser diodes”. IEEE J. Select. Topics Quant. Electron., 3(3), 862-873 (1997)

[27] M. Salvalaglio, R. Backofen, A. Voigt, and F. Montalenti, “Morphological evolution of pit-patterned Si(001) substrates driven by surface-energy reduction”, Nanoscale Res. Lett., 12, 554 (2017)

[28] G. Biasiol, A. Gustafsson, K. Leifer, and E. Kapon, “Mechanisms of self-ordering in nonplanar epitaxy of semiconductor nanostructures”, Phys. Rev. B, 65 205306 (2002)

[29] V. Dimastrodonato, E. Pelucchi, and D. D. Vvedensky, “Self-limited evolution of seeded quantum wores and dots on patterned substrates”, Phys. Rev. Lett, 108(25), 256102 (2012)

[30] A. Kaluza, A. Schwartz, D. Gauer, H. Hardtdegen, N. Nastase, H. Lüth, Th. Schäpers, D. Meertens, A. Maciel, J. Ryan, E. O’Sullivan, “On the choice of precursors for the MOVPE-growth of high-quality $Al_{0.30}Ga_{0.70}As$/GaAs v-groove quantum wires with large subband spacing”, *J. Cryst. Growth*, **221**, 91-97 (2000)

[31] M-S. Kim, Y. Kim, M-S. Lee, Y. J. Park, S-I. Kim, and S.K. Min, “Growth behaviour on V-grooved high Miller index GaAs substrates by metalorganic chemical vapour deposition”, J. Cryst. Growth, 146, 482-488 (1995)

[32] L. Hofmann, A. Knauer, I. Rechenberg, U. Zeimer, and M. Wyeres, “Comparison of binary and ternary growth over trenches using MOVPE”, J. Cryst. Growth, 213(3-4), 229-234 (2000)

[33] G. Vermeire, I. Moerman, Z. Q. Yu, F. Vermaerke, P. van Daele, and P. Demeester, “Atmospheric and low pressure metalorganic vapor phase epitaxial growth of vertical quantum wells and quantum well wires on submicron gratings”, J. Electon. Mater., 23(2), 121-124 (1994)

[34] S. H. Jones, L. K. Seidel, K. M. Lau, and M. Harold, “Patterned substrate epitaxy surface shapes”, J, Cryst. Growth, 108, 73-88 (1991)

[35] L. Buydens, P. Demeester, M. van Ackere, A. Ackaert, and P. van Daele, “Thickness variations during MOVPE growth on patterned substrates”, J. Electron. Mater., 19(4), 317-321 (1990)

Chapter 4 |

Regrowth of (100) and (311)B Orientated PC Structures

This chapter presents a scanning- (SEM) and scanning transmission electron microscopy (STEM)-based investigation into the kinetic influences of infill layer composition on the formation of voids in the (Al)(Ga)As photonic crystal (PC) system. Initially, a comparison is made between the use of AlAs, AlGaAs, and GaAs as the regrowth material for nominally identical gratings on (100) orientated substrates. Of the three systems, regrowth utilizing GaAs resulted in complete infilling of the grating layer and the elimination of voids. In the case of AlAs and $Al_{0.35}Ga_{0.65}As$, voids are present in the regrown structures. Whilst the voids display a similar shape for both materials, those in AlGaAs are substantially smaller, in line with the increased adatom mobility of gallium compared to that of aluminium. In both cases, a degree of asymmetry in the void shape is observed in the plane of the PC layer, along its orthogonal axes. This is attributed to the differing polarity and incorporation rates

of high-index crystal plane in different crystal plane directions. These differences are believed to impact the evolution of the growth front in each case, leading to either stable or dynamic faceting in orthogonal cross-sections, and resulting in a more complex void shape for AlAs-regrown samples as compared with those were AlGaAs is used.

Following this, void size tuning is investigated for three AlGaAs-regrown structures in which the dimensions of the grating pits are varied. As the *r*/*a* and etch depth of the pits are reduced, so too are the height and radii of the voids that form within them. While none of the structures investigated produced voids with optimal geometries for device applications, extrapolation and interpolation of data indicates pit dimensions that should produce voids with the desired *r*/*a* and height for future device fabrication.

Finally, the use of $(311)B$ orientated substrates was explored in conjunction with an AlGaAs infill layer. As with (100) orientated samples, voids are formed within the PC structures, however their shape and geometry are changed substantially. The reduced crystal plane symmetry of this orientation compared with (100) surfaces results in asymmetric growth profiles along one of the PC axes, with domain-like growth resulting from non-equivalent $\{311\}B$ and $\{111\}B$ planes. Consequently, in addition to a greatly enhanced in-plane asymmetry, voids on $(311)B$ orientated substrates display a more complex out-of-plane asymmetry when viewed along one axis of the PC, pointing to an additional degree of freedom in future PC design.

4.1. Motivation

As discussed in Chapter 3, void formation during regrowth of the PC layer is influenced by two factors: self-shadowing of the evolving growth front as deposition proceeds, and the mobility of the group-III species involved [1,2]. Whilst the extent of self-shadowing is influenced by the geometric constraints of the PC grating design, such as pit depth and diameter (i.e. the aspect ratio of the pit), the mobility of the adatom species involved is an expression of the kinetics of the system and can be tuned to some degree through the choice of growth conditions. Previously, growth rate, temperature, and V/III ratio have all been shown to affect the mobility and diffusion lengths of adatoms during growth on patterned substrates [3,4], and are routinely used to control the formation of nanostructures such as V-groove quantum wires [5,6].

In the context of PC regrowth, to date only two studies have been published in which growth conditions have been used to influence to extent of grating infill and void formation. In the first, it was shown that voids could be eliminated and an all-semiconductor infill achieved in GaAs/InGaP PC system simply by reducing the V/III ratio during GaAs regrowth [7]. In the second, void formation in the InP PC system was explored more extensively, with a reduction in void size being associated with higher growth temperatures and reduced growth rate and V/III ratio, where greater In adatom mobility is promoted [8]. Until now, no similar study has been reported for the (Al)(Ga)As/GaAs PC system, and the extent to which void formation can be controlled by tuning group-III adatom mobility is unclear.

Irrespective of the growth conditions used, it has been demonstrated that different group-III species have fundamentally different surface mobilities owing to the inherent difference in adatom adsorption strengths. In growth of AlAs and GaAs layers on patterned substrates it has been shown that, under the same growth conditions, gallium adatoms exhibit longer diffusion lengths than the more strongly adsorbed aluminium, resulting in large difference in the local growth rates for the two layers [9]. Similar effects have also been reported during growth of V-groove quantum wires, where the larger surface mobility of gallium adatoms can lead to diffusion-driven segregation of the group-III species within the regrown $Al_xGa_{1-x}As$ layer, giving rise to vertical quantum well-like structures [10]. The extent to which void formation in the (Al)(Ga)As/GaAs PC system is affected by the differing mobilities of the group-III species is yet to be reported; however, it is expected that the dynamics and extent of grating infill during regrowth may be controlled to some degree by varying the composition of the infill layer used.

As highlighted in the results of Chapter 3, an additional factor affecting the kinetics of PC regrowth is the local crystallography of the grating pit profile. In particular, the exposure of higher-Miller index planes with larger growth rates played a significant role in driving infill dynamics and changes in void geometry [1]. In the case of regrowth on patterned substrates, the exposure of many crystal planes leads to growth rate anisotropies across the wafer surface, and it has been shown previously that these anisotropies can lead to complex faceting and asymmetric growth profiles [11,12]. In the context of PC regrowth, asymmetric growth is an interesting phenomenon to explore as it could significantly alter the dynamics of grating infill and result in additional degrees of asymmetry in the shape of any voids

that form. Whilst previous studies have looked at the impact of differing PC atom shape on void formation during regrowth [13], all structures reported thus far have been produced on (100)-orientated substrates [1,7,8,12]. An alternative approach would be to investigate the use of higher-index-orientation substrates, such as $(311)B$, which possess reduced crystal plane symmetry compared with (100) surfaces, and may offer an efficient way to introduce new facet-dependent kinetics to the PC system without significant changes in grating geometry.

This work presents a study into the kinetic effects influencing void formation during the regrowth of GaAs-based PC structures with circular grating pits. Firstly, in order to investigate the effect of group-III adatom mobility, three samples with nominally identical grating geometries were overgrown on (100) substrates using different infill layer compositions: one where AlAs is the primary constituent, another with GaAs, and, finally, one where an intermediate AlGaAs alloy is used. Following this, the effect of grating geometry on void formation is explored for AlGaAs samples where the *r*/*a* and etch depth of the unit cell are varied. Finally, a comparison is made between structures grown on axis and those grown on $(311)B$ orientated substrates. In all cases, samples were regrown using a superlattice (SL) structure to aid in structural analysis, which was performed by a combination of plan-view and cross-sectional SEM and STEM imaging, in-line with the methodology outlined in Chapter 3.

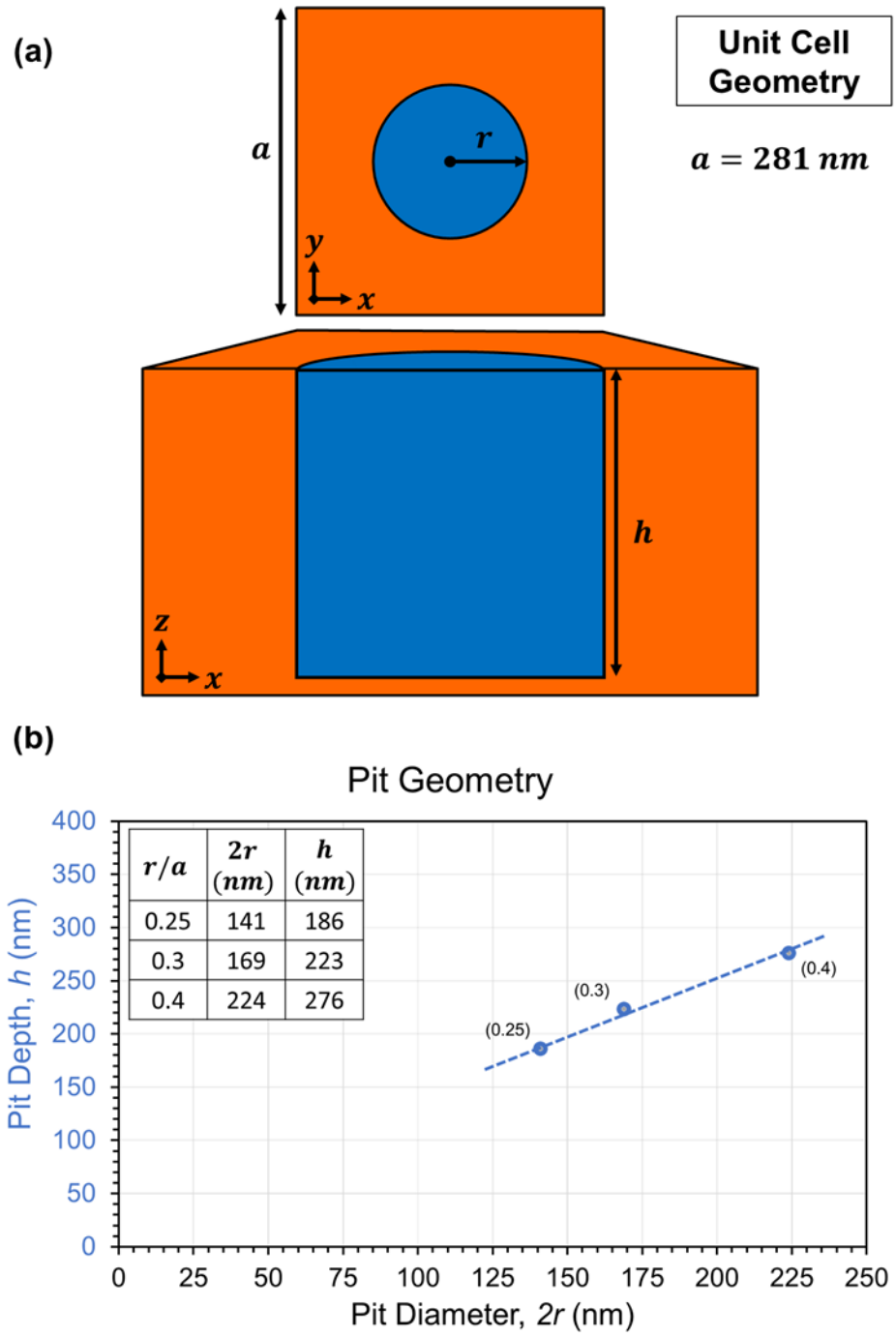

Figure 4.1. (a) Schematic diagram showing plan-view and cross-sectional PC unit cell geometries. The orange region corresponds to the matrix material (in this case, GaAs) whilst the blue region is that of the grating pit. The values *a*, *2r* and *h* correspond to the PC lattice constant, pit diameter, and pit depth, respectively. (b) Plot of pit etch depth as a function of diameter, determined via STEM analysis. The corresponding pit *r*/*a* values are indicated in brackets.

4.2. Sample Preparation

PC test structures consisting of a 1000 x 1000 square lattice of circular holes were prepared on *n*-GaAs substrates with two different surface orientations: (100) 2°-offcut towards the $< 1\bar{1}0 >$ direction, and $(311)B$. No light emitting element is included in any of the samples described here, allowing only for structural analysis in relation to grating infill and void formation. Following deposition of a 200 nm SiO_2 film and thick PMMA photoresist layer, the PC pattern was transferred to the substrates by a combination of electron beam lithography (EBL) and reactive ion etching (RIE). The period of the PC, *a,* was set to 281 nm so as to align with a theoretical emission wavelength of 940 nm, for atoms composed entirely of AlAs.

The geometry of the grating pits was varied across samples in order to assess the tuning range of void sizes. Three nominal unit cell dimensions were defined based on *r*/*a* values of 0.4, 0.3, and 0.25, and etched under the same RIE conditions. The target etch depth for the 0.4 *r*/*a* hole was 281 nm. Owing to their decreasing diameter and aperture-dependent etch rates observed during RIE etching [14], the resulting depths of the 0.3 and 0.25 *r*/*a* features were significantly shallower than that seen for *r*/a = 0.4. A schematic diagram of the PC unit cell is shown in Figure 4.1(a), with the values of grating pit diameter, *2r*, and depth, *h*, measured during STEM analysis summarised and plotted in panel (b).

Representative plan-view and cross-sectional SEM images of the as-etched PC gratings are shown in Figure 4.2. A layer of Pt was deposited on the surface of the sample to protect the etched features during focused ion beam (FIB) milling. Whilst the use of an SiO_2 hard mask for RIE etching was intended to produce holes with

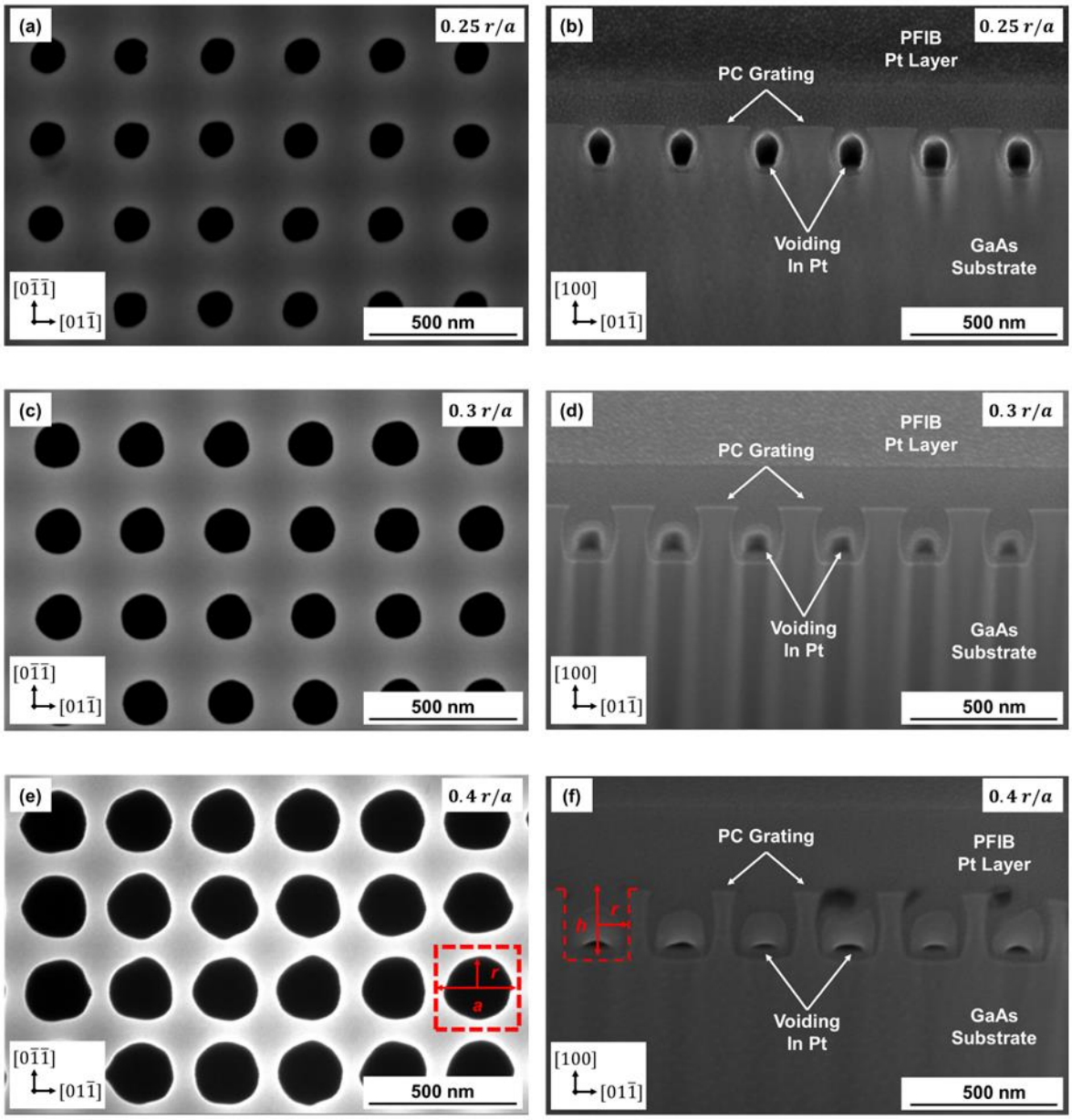

Figure 4.2. Plan-view and cross-sectional SEM images of as-etched PC gratings with *r*/*a* values of 0.25 (a,b), 0.3 (c,d), and 0.4 (e,f). A layer of Pt was deposited onto the sample surface before cross-sectional milling to protect the etched features, resulting in voids forming within the pits. The PC unit cell and pit dimensions are highlighted in panels (e) & (f).

vertical sidewalls, in reality they present with re-entrant or “barrel-shaped” profiles. This is attributed to the use of dry etch conditions which were not fully optimised for the small diameter, high-aspect ratio features required for PC gratings. In this context, previous work has shown that secondary sputtering effects within the pit result in an imbalance between physical and chemical mechanisms during etching, leading to erosion of the natural amorphous pacifying layer that forms on the pit sidewalls, and ultimately to a slight undercutting of the SiO_2 hardmask [15].

Following etch of the PC grating layer, wafers were prepared for MOVPE overgrowth by UV/ozone cleaning and a one minute etch in a 10:1 buffered HF solution to remove the residual SiO_2 mask. Regrowth was performed in a Thomas Swan close-coupled showerhead MOVPE reactor at a pressure of 100 mbar with hydrogen (H2) as the carrier gas. Trimethylaluminium (TMAl) and trimethylgallium (TMGa) were utilised as group-III precursors, with arsine (AsH3) as the group-V precursor. In line with the results of Chapter 3, the reactor was ramped to the growth temperature of 650 °C in three minutes under a constant AsH_3 flow of 100 sccm in order to minimise the extent of pre-growth mass transport [1]. The samples were then overgrown with 300 nm of a SL structure followed by a 100 nm GaAs cap; all material is undoped in this case. The SL was comprised of 30 periods with nominal layer thicknesses of 9 nm and 1 nm, and was chosen over a bulk layer to aid with structural analysis, as in the previous chapter. In order to study the effects of group-III mobility on grating infill dynamics, three different SL compositions were used: AlAs/GaAs, GaAs/AlAs, and $Al_{0.35}Ga_{0.65}As$/AlAs. Hereafter, the infill layer in each case will be referred to simply as AlAs, GaAs, and AlGaAs, respectively. Group-III source flows were balanced to give

a constant nominal growth rate of 6 nm/min on a planar (100) surface across all samples. A constant AsH_3 flow of 100 sccm was employed, giving a V/III ratio of 700.

SEM imaging, cross-sectioning milling and STEM lamellae lift-out was performed using a Thermo Fisher Helios Xe-plasma dual beam FIB system equipped with an Easy Lift micromanipulator. As described in the Chapter 3, in order to ensure that the features analysed were representative of any given unit cell, cross-sections were taken at a slight angle relative to the PC array axes, so as to cut diagonally through successive pits and ensure that the centre of some pits would be bisected. An angle of 1.9° was used in the case of large area milling. Lamella were prepared at an angle of 4.8° relative to the PC axes using a standard lift-out procedure [16]. STEM analysis was performed using a JEOL ARM200cF TEM operating at 200 kV.

4.3. Effects of Group-III Adatom Mobility

In order to investigate the effects of group-III adatom mobility on grating infill dynamics and void formation, three samples containing 0.4 *r*/a PCs were prepared on (100) -orientated substrates and overgrown with infill layers of differing compositions. Figure 4.3. shows plan-view and cross-sectional SEM images of samples following regrowth with (a,b) AlAs, (c,d) AlGaAs, and (e,f) GaAs SL structures, respectively.

Initial plan-view imaging at a conventional 5 kV accelerating voltage (not show) presented smooth, featureless surfaces in all cases, indicating good quality overgrowth with minimal defect formation. Subsequent imaging at 30 kV (as show in panels a,c,e) revealed an array of dark spots in both the AlAs and AlGaAs samples.

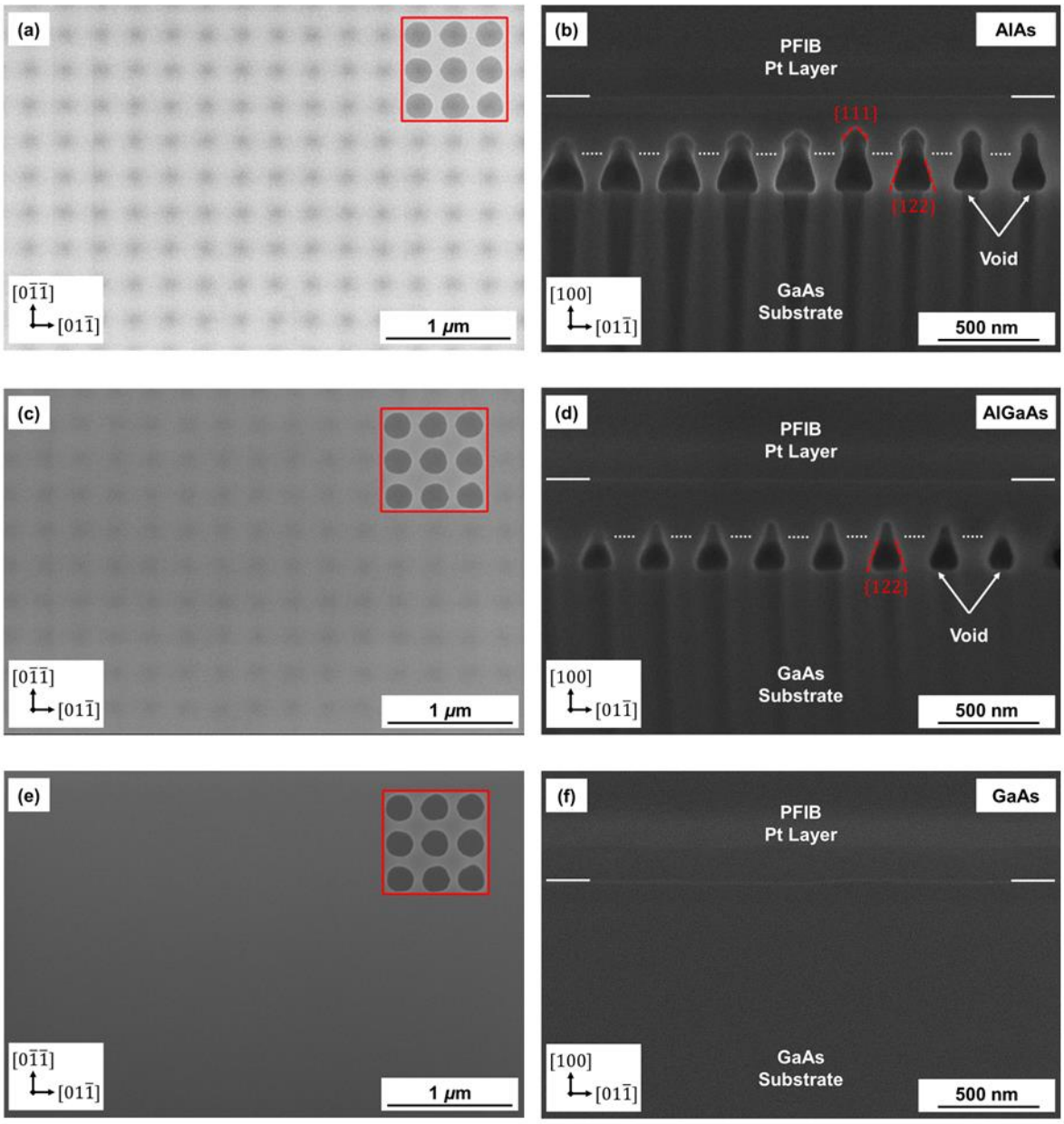

Figure 4.3. Plan-view (30 kV) and cross-sectional SEM images of 0.4 r/a PCs following regrowth with AlAs (a,b), AlGaAs (c,d), and GaAs (e,f). High kV imaging reveals an array of high-contrast subsurface features - the as-etched grating is overlain to highlight their location with respect to the PC (plan-view, inset). The presence of voids within the AlAs and AlGaAs-regrown structures is confirmed in the cross-sectional images. Solid white lines indicate the interface between the sample surface and the protective Pt layer. Dashed white lines indicate the approximate location of the original grating surface. No voids are present in the GaAs sample.

The higher beam energies associated with larger accelerating voltages results in an increased interaction volume between the electron probe and the sample material, allowing incident electrons to penetrate further into the sample [17]. When combined with the thin amount of material deposited during regrowth (400 nm), the increased penetration depth allows for high-contrast sub-surface features to be imaged. Whilst both secondary (SE) and back scattered (BSE) electrons are produced below the sample surface, typically only BSEs have sufficient energy to escape and be detected [18]. In this case, however, imaging was performed in SE detection mode. Here the contrast mechanism is thought to result from the relative intensities of additional near-surface SEs that are produced through secondary scattering events related to BSEs produced deeper within the sample. The lower intensity associated with the dark spots, in this case, is the result of a lower secondary-SE yield in these regions, indicating the presence of voids within the regrown layer. Due to the diffuse nature of the dark spots, a more detailed analysis of the buried features was not possible. However, the relative intensities of the spots decreased for the AlGaAs sample compared to AlAs indicating a reduction in void size. In the case of GaAs, no such features are observed, suggesting the absence of voids.

The presence of voids in AlAs- and AlGaAs-regrown structures is confirmed in the cross-sectional SEM images shown in Figure 4.3.(b,d,f), which are viewed along the $[0\bar{1}\bar{1}]$ crystal direction. The voids appear as a line of black features in the semiconductor matrix owing to the absence of material and, therefore, reduced SE signal emanating from these regions. In the case of AlAs-regrowth, the void profile is dominated by two main bounding sidewall orientations; a set of long sidewalls originating from the initial regrowth interface at the bottom of the pit which can be

approximated to $\{122\}$-like crystal planes; and a set of $\{111\}$-like planes which terminate the top of the void. Sidewall orientations were assigned based on STEM analysis (discussed below), given the approximate angles at which they intersect the (100) surface. Whilst the diameter of the voids at their widest point ($2r'$ = 210 nm) is marginally smaller than the diameter of the pit ($2r$ = 224 nm), their heights (h' = 390 nm) has increased significantly compared with the initial etch depth (h = 281 nm). Taken together, these observations indicate that incorporation of adatoms within the grating pit is limited, with the majority of deposition acting to drive vertical and lateral growth of the upper (100) surface. This can be attributed to the low mobility of aluminium species under the growth conditions used, combined with self-shadowing effects associated with the high-aspect ratio of the grating pit (approximately 1.25). Together, these factors are thought to limit both diffusion of adatoms into the body of the pit and also direct adsorption/deposition of gas-phase atoms within the pit during growth [1,2,3].

In the case where AlGaAs is the infill layer, void formation is again favoured. In comparison to AlAs, however, void size is reduced significantly, with h' and $2r'$ values of 315 nm and 150 nm, respectively (c.f. 390 nm and 210 nm for AlAs regrowth). This equates to a 20 % reduction in h' and 30 % reduction in $2r'$, associated with increased deposition within the grating pit during the early stages of regrowth (as confirmed by STEM imaging, below). We attribute this increased deposition to the larger surface mobility inherent in the AlGaAs alloy compared with the binary aluminium compound [9], which results in greater diffusion of species from the upper surfaces of the grating to the sidewalls and bottom planes of the pit. Whilst the voids are smaller in this case, they do share a similar profile to that seen for AlAs, being bound by the same

{122}-like sidewall plane. However, the upper {111}-like planes seen for AlAs are absent here, suggesting the role of a more complex faceting mechanism in determining void shape for this PC geometry. This concept is explored further in the sections below.

The decrease in void dimensions associated with the inclusion of gallium into the AlGaAs alloy is taken to the extreme in the case of binary GaAs regrowth where no voids are observed in the PC layer. Complete grating infill is attributed to the increased diffusion lengths of adatoms associated with the higher inherent surface mobility of gallium compared with aluminium, allowing for more diffusion to the lower surfaces of the pit [3,9]. As the pit dimensions and growth conditions are the same for both systems, the large tuning range in void dimensions that we observe here highlights the importance of group-III adatom mobility in dictating the extent of grating infill and void formation in PC regrowth.

In the context of PC design, none of the structures described here provide the optimum geometry for use in PCSELs; indeed, in the case of GaAs, complete infilling of the grating removes the refractive index contrast required for a PC. For the AlAs and AlGaAs structures, the voids exhibit effective r/a values of 0.37 and 0.26, respectively, which sit between the theoretical values for maximum grating coupling strengths of 0.2 and 0.4 [19]. Similarly, the heights of the voids are significantly larger than the approximately 140 nm (i.e. $0.5a$) required for optimum optical confinement factors [20]. However, the purpose of this study is to investigate the role of adatom mobility on void geometry, switching from low mobility aluminium to higher mobility gallium across the three samples studied. The above results indicate that the degree of infilling is strongly linked to adatom mobility, with the cases of AlAs and GaAs-

regrowth representing the extremes in the range of void geometries accessible in this PC system. This points to a strategy by which the critical void dimensions could be engineered to more optimal values simply by tuning the aluminium composition of the infill layer. This would provide a useful parameter for PCSEL design, allowing for adatom mobility to be manipulated independently of the regrowth conditions used, which tend to affect more than a single kinetic process.

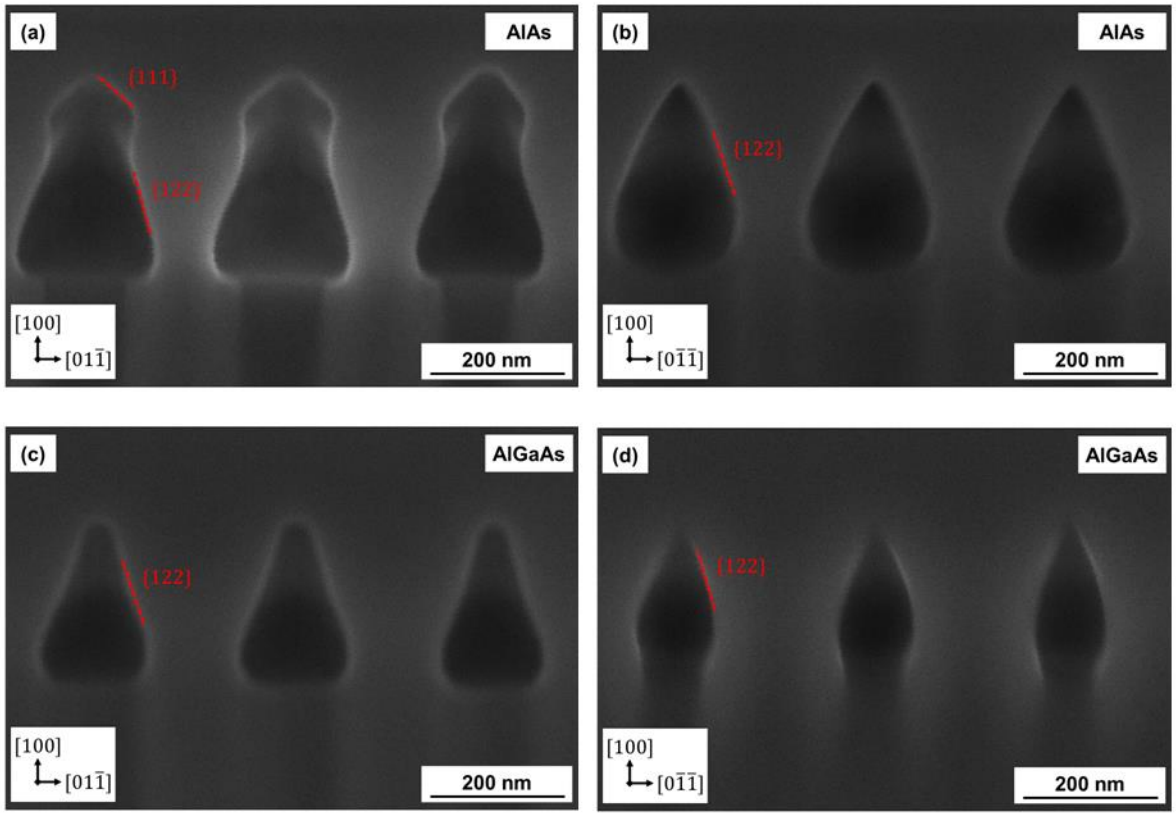

Figure 4.4. Cross-sectional SEM images of voids in 0.4 *r*/*a* PCs following regrowth with AlAs (a,b) and AlGaAs (c,d), as viewed along the orthogonal axes of the PC. Voids in the AlGaAs sample are significantly smaller than in AlAs, in line with increased adatom surface mobility. In both cases, a degree of asymmetry in void shape is observed when comparing the (a,c)$[0\bar{1}\bar{1}]$ and (b,d) $[01\bar{1}]$ cross-sections. The asymmetry is reflected in a rounding of the void profile at the bottom og the grating pit when viewed along the $[01\bar{1}]$ direction. For akk voids, the bounding sidewalls can be approximated to $\{122\}$-like planes, with additional $\{111\}$-like planes emerging in the coalescence region in the case of AlAs (a)

4.4. Origins of In-plane Asymmetry

In order to obtain a more complete understanding of the three-dimensional nature of the voids formed in AlAs and AlGaAs-regrown samples, additional cross-sections were prepared along the orthogonal PC axis, perpendicular to the $[01\bar{1}]$ crystal plane direction. Figure 4.4. shows higher magnification cross-sectional SEM images of AlAs and AlGaAs samples as viewed along (a,c) $[0\bar{1}\bar{1}]$ and (b,d) $[01\bar{1}]$ directions. For both infill layer compositions, a degree of asymmetry in void shape is evident within the plane of the grating. The lower section of the voids project an elliptical, rather than circular, profile when considered in plan-view. As viewed along the $[0\bar{1}\bar{1}]$ direction, the voids appear to be flat bottomed with abrupt intersections with the sidewall planes. In the $[01\bar{1}]$ cross-section, however, the bottom bounding surface is narrower, indicating increased incorporation of material on the void's internal surfaces and suggesting an anisotropy in adatom diffusion kinetics within the pits in the initial stages of regrowth. Further up in the voids, it is noted that both AlAs and AlGaAs cross-sections again display a pair of continuous $\{122\}$-like sidewall planes when viewed along the $[01\bar{1}]$ direction, but neither exhibit vertical or {111}-like surfaces. As a result, voids in AlAs-regrown samples display an enhanced asymmetry with respect to the PC axes compared with AlGaAs, producing an arrow-head three-dimensional volume.

The origins of the asymmetry in the initial stages of deposition were explored further by STEM analysis of AlGaAs-regrown structures. Figure 4.5. shows annular-dark field (ADF)-STEM images of a single period of the PC as viewed along the (a) $[0\bar{1}\bar{1}]$ and (b) $[01\bar{1}]$ directions. Here the black voids contrast against the grey infill

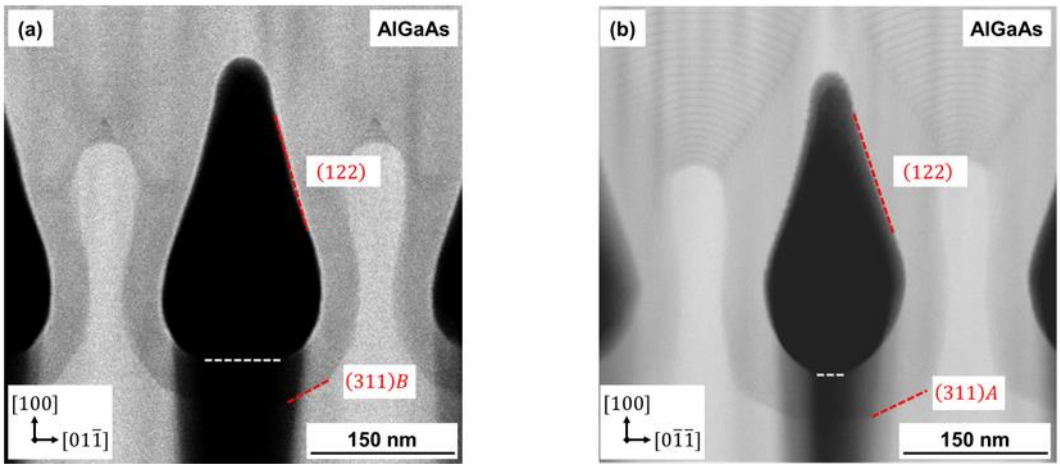

Figure 4.5. Cross-sectional ADF-STEM images of voids formed during regrowth with AlGaAs, as viewed along the (a) $[0\bar{1}\bar{1}]$, and (b) $[01\bar{1}]$ crystal direction. White dashed lines indicate the bottom of the voids, which have been obscured by streaking artifacts from FIB milling. The (122)-like void sidewalls are highlighted. Micro-faceting of the surface bounding the grating pit results in the presence of high-index crystal planes (e.g. (311), highlighted) at the regrowth interface. The differing polarities of these planes (*A* vs *B*) produces anisotropies in incorporation rates, leading to an asymmetry in void shape along orthogonal axes.

layer and white GaAs grating layer. It can be seen that the surface of the pit, and therefore the initial regrowth interface, is micro-faceted with high-index crystal planes, including (311), which is attributed to mass-transport phenomena and surface restructuring prior to deposition [1]. Along orthogonal crystal directions, high-index planes are characterised by opposite polarities determined by the nature of the dangling bonds on the surface. $(311)A$ planes (present in the $[01\bar{1}]$ cross-section) are terminated by group-III bonds, and adatoms have higher sticking probabilities, giving rise to higher incorporation rates than for their B-type (group-V) counterparts [21,22]. This growth rate anisotropy leads to increased incorporation of adatoms in the $[01\bar{1}]$ cross-section, producing thicker layers inside the pits in panel b in comparison to panel a, and causing the observed asymmetry. As diffusion from the upper regions of the pit to the lower planes is thought to be limited in the case

of void formation, the growth rate anisotropy seen here is thought to be the result of either preferential decomposition of precursors on A-type planes [23], or diffusion of adatoms from B-type planes to A-type.

When considering ideal PC structures for device applications, previous studies have reported that asymmetry in void shape with respect to the PC axes is beneficial in achieving optimum optical confinement factors [24,25]. Whilst geometrically enforced asymmetry has been realised previously though the use of triangular grating pits [13], to the best of our knowledge, this study presents the first known demonstration that in-plane asymmetry can be achieved using circular grating pits. The above results suggest that the growth rate anisotropies associated with the polar nature of high-index crystal planes in III-V materials may be exploited in order to achieve complex asymmetries even in simple PC structures, and may be engineered to some extent through careful design of pit dimensions or regrowth conditions.

Above the bottom of the pit, the void shape in the AlGaAs-regrown sample evolves in a similar manner in both cross-sections, with the accommodation of adatoms onto the internal {122} surfaces producing a tapered profile that gradually encapsulates the void as deposition proceeds. However, differences are observed in the evolution of the growth front emanating from the surface at the top of the grating. Figure 4.6. shows higher magnification ADF-STEM images of this region for the corresponding images in Figure 4.5. The evolution of the growth front during deposition is tracked by the thin AlAs layers of the SL structure. As the signal intensity in ADF imaging is approximately proportional to the average atomic number squared, AlAs layers appear as dark lines in the lighter AlGaAs matrix, providing contrast. The lower resolution of the SL layers in (a) compared with (b) is attributed to increased

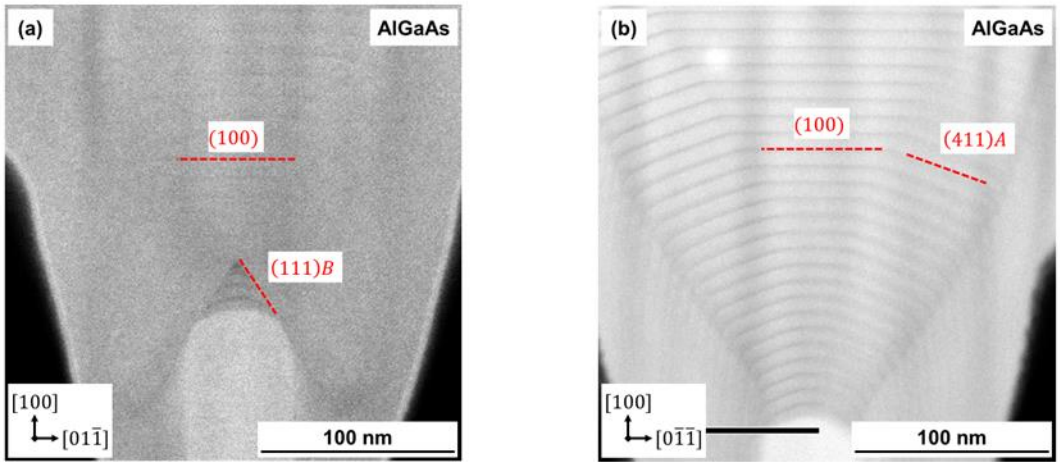

Figure 4.6. Cross-sectional ADF-STEM images of the inter-pit region in AlGaAs-regrown structures, as viewed along the (a) $[0\bar{1}\bar{1}]$, and (b) $[01\bar{1}]$ crystal direction. SL layers illustrate the evolution of the growth front as deposition proceeds. Two modes of faceting, termed *dynamic* (a) and *stable* (b), are observed along orthogonal axes. In the case of *stable* faceting, a (100) plane and vicinal $(411)A$ planes emerge in the early stages of the process and are replicated in subsequent layers as they grow laterally, stabilised by the *A*-type nature of high-index planes in this direction. Where faceting is *dynamic*, growth initially proceeds through the formation of $\{111\}$ non-growth planes (NGPs), owing to the low incorporation rates of high-index planes in this cross-section. Only sometime later does a stable (100) plane emerge, and lateral growth proceed.

lamella thickness and poorer surface quality, rather than the quality of the epilayers themselves.

Here we introduce two terms to describe the differing modes of faceting observed along each of the PC axes: "*stable*" faceting, for which the local composition of crystal planes does not significantly change with time, and "*dynamic*" faceting, which is characterised by a distinct change in the local crystallography as the growth front evolves. In the $[01\bar{1}]$ cross-section, the growth front quickly stabilises within the first three or four periods of the SL, being defined by a central (100) plane flanked on either side by vicinal $\{411\}A$ facets. This *stable* faceting profile is replicated in successive layers of the SL, with successive planes growing

laterally across the grating pit opening facilitated by simultaneous lateral growth of the pit sidewalls, presumably both by diffusion of material from the upper surface and by direct incorporation of gas-phase species. Indeed, weak and tightly-spaced vertical dark lines in Figure 5(b) indicate the SL structure to be replicated on the void sidewalls with a reduced effective deposition rate. Downward growth of these vertical SL surfaces terminates in the formation of the observed {122} planes, which are A-type and therefore stabilised by their relatively low surface energy. In contrast, the growth front in the $[0\bar{1}\bar{1}]$ cross-section is less stable, displaying *dynamic* faceting. Growth initially proceeds through the formation of $\{111\}B$ non-growth planes (NGPs) owing to the low incorporation rates on B-type planes [26,27]. Sometime later, once the sidewall planes of the void have become inclined and diffusion away from the upper region of the pit is minimised, stable (100) planes emerge, and successive layers grow laterally until they encapsulate the voids.

The same facet dynamics are also evident in AlAs-regrown samples and can be used to explain the more complex void shape seen in the $[0\bar{1}\bar{1}]$ cross-section compared with that in AlGaAs. The associated cross-sectional ADF-STEM image is shown in Figure 4.7(a). Initially, growth proceeds through the formation of the same $\{111\}B$ NGPs, however the lower mobility of adatoms in AlAs results in different diffusion dynamics, changing the rate at which the stable (100) emerges and the balance between vertical and lateral growth. As a result of a reduced rate of lateral growth compared to AlGaAs, the void profile becomes elongated and encapsulation of the voids takes more time and requires a thicker regrowth film. The voids are again bound by $\{122\}$-like sidewalls that gradually grow together in both cross-sections. The void asymmetry is accentuated in the $[0\bar{1}\bar{1}]$ cross-section by the eventual

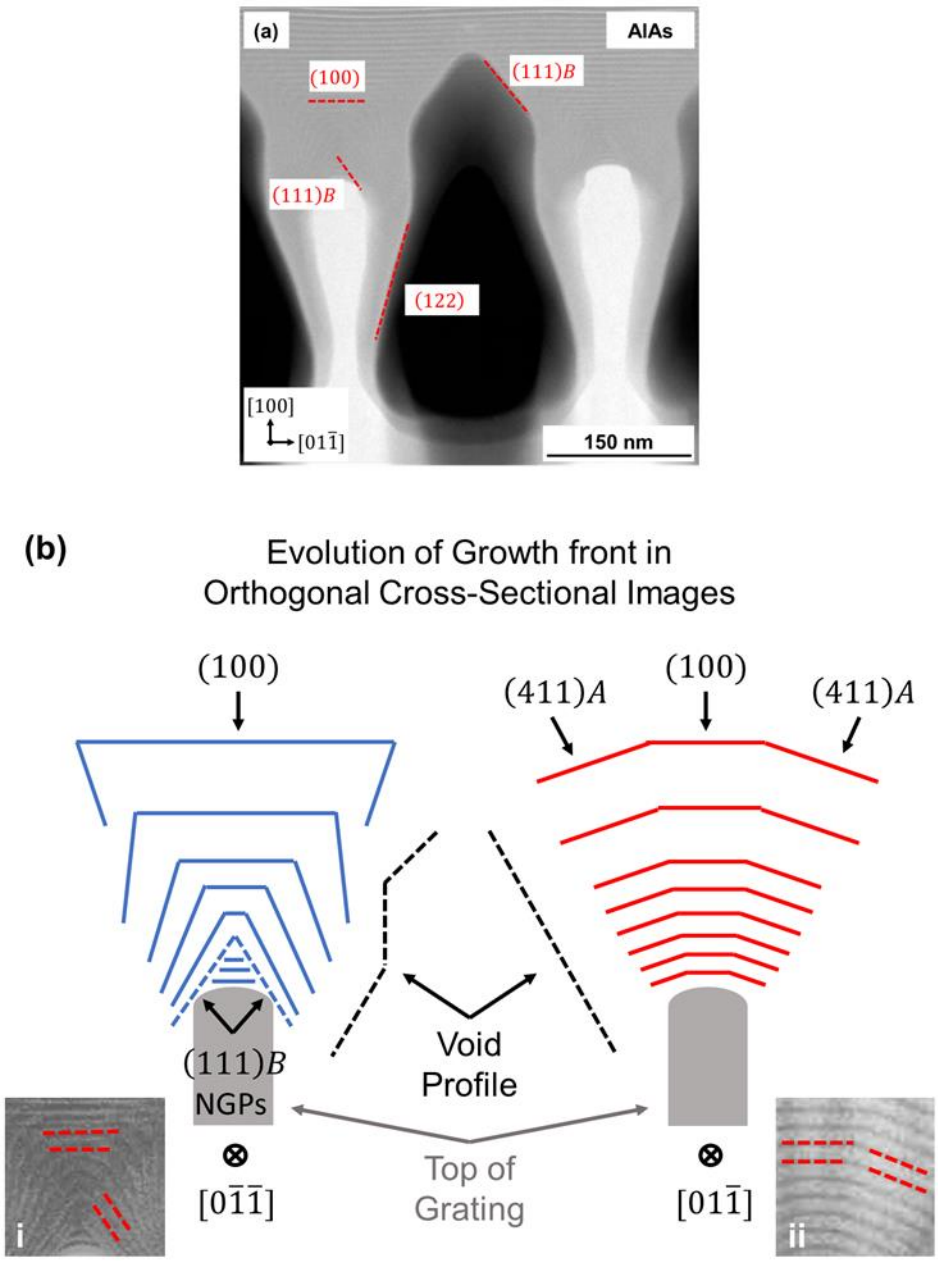

Figure 4.7. (a) Cross-sectional ADF-STEM image of voids in AlAs-regrown structures, as viewed along the $[0\bar{1}\bar{1}]$ crystal direction. In addition to the $\{122\}$-like sidewall planes, $\{111\}$-like planes emerge in the coalescence region at the top of the void. (b) Schematic diagram illustrating the role of *dynamic* and *stable* faceting in producing the enhanced void shape asymmetry seen for AlAs compared with AlGaAs. High magnification STEM images of the faceting are shown, inset. The reduced adatom mobility in the case of AlAs compounds the extent of *dynamic* faceting, resulting in a more complex profile

production of near-vertical $\{011\}$ planes, and $\{111\}$ facets which emerge at the top of the voids.

Higher magnification images of the growth front along both axes of the PC (examples of which are shown, inset) were used to create the schematic diagram shown in Figure 4.7(b), which illustrates the link between dynamic and stable faceting dynamics, the evolution of the growth front, and the resultant void sidewall profile along the orthogonal PC axes. The existence of an additional mechanism of void shape asymmetry, and its strong dependence on the mobility of the group-III species involved, points to an additional degree of freedom in design of optimal PC structures. This result suggests that complex three-dimensional void shapes may be engineered using simple pit geometries by tuning of regrowth conditions to promote lower adatom diffusion, thereby changing the relative rates of lateral and vertical growth and enhancing the natural anisotropies associated with different crystal plane polarities.

4.5. Effects of Grating Pit Geometry

In addition to the 0.4 *r*/*a* gratings described in Sections 4.3. & 4.4., two further PC geometries were investigated in order to explore the tuning range of void sizes in AlGaAs-regrown structures. Bright field (BF)-STEM images showing the corresponding $[01\bar{1}]$ cross-section for gratings with nominal *r*/*a* values of 0.3 and 0.25 are shown in Figure 4.8., along with the previously analysed 0.4 *r*/a structure. Signal intensity in BF imaging corresponds to unscattered electrons from the direct beam and is inversely proportional to the atomic mass. As a result, contrast in BF images is

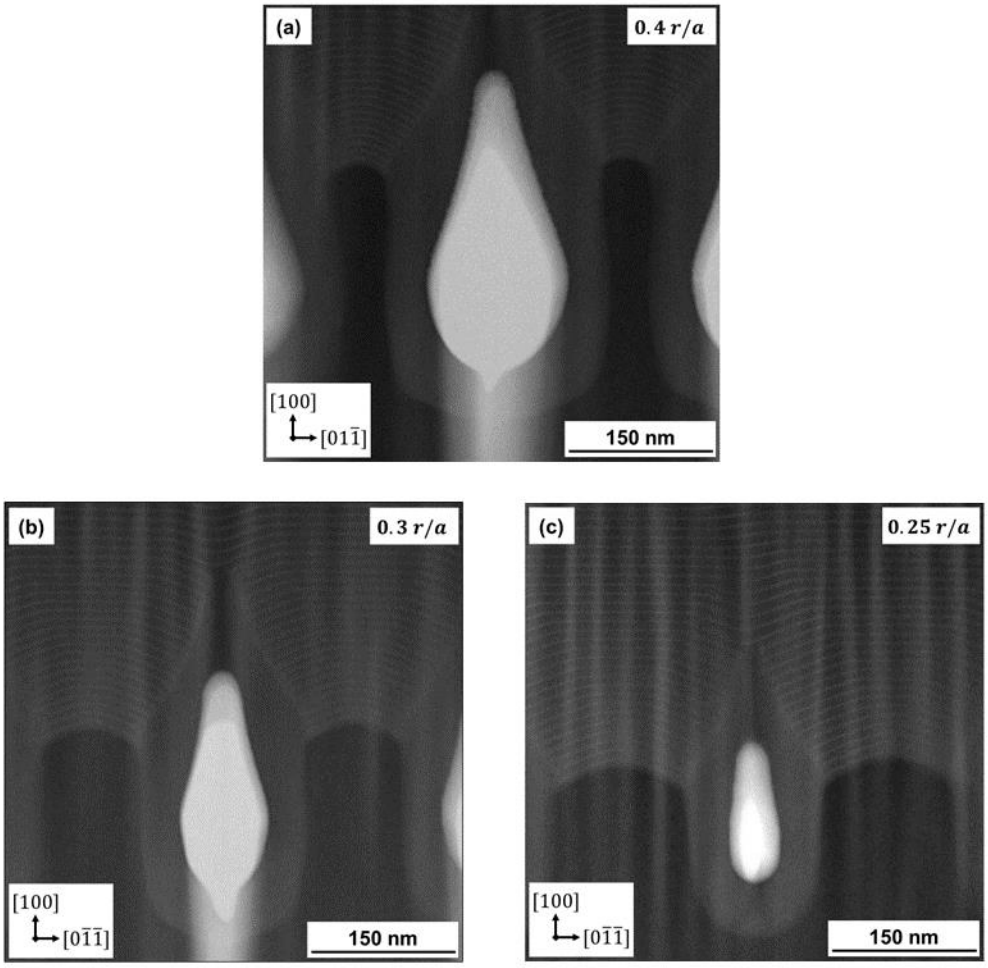

Figure 4.8. Cross-sectional BF-STEM images of voids in (a) 0.4, (b) 0.3, and (c) 0.25 *r*/*a* PC structures following regrowth with AlGaAs, as viewed along the $[01\bar{1}]$ direction. Void dimensions decrease in line with decreasing pit dimensions in each case. The nominal *r*/*a* values of the PC following regrowth are 0.26, 0.16, and 0.09, respectively.

Grating Pit				***Void***		
r/a	***2r* (nm)**	***h* (nm)**		***r/a'***	***2r'* (nm)**	***h'* (nm)**
0.4	224	276		0.26	150	315
0.3	169	223		0.16	92	234
0.25	141	186		0.09	51	146

Table 4.1. Measured diameter, 2r and height, *h* of PC grating pits and voids (‘), and corresponding *r*/*a* values

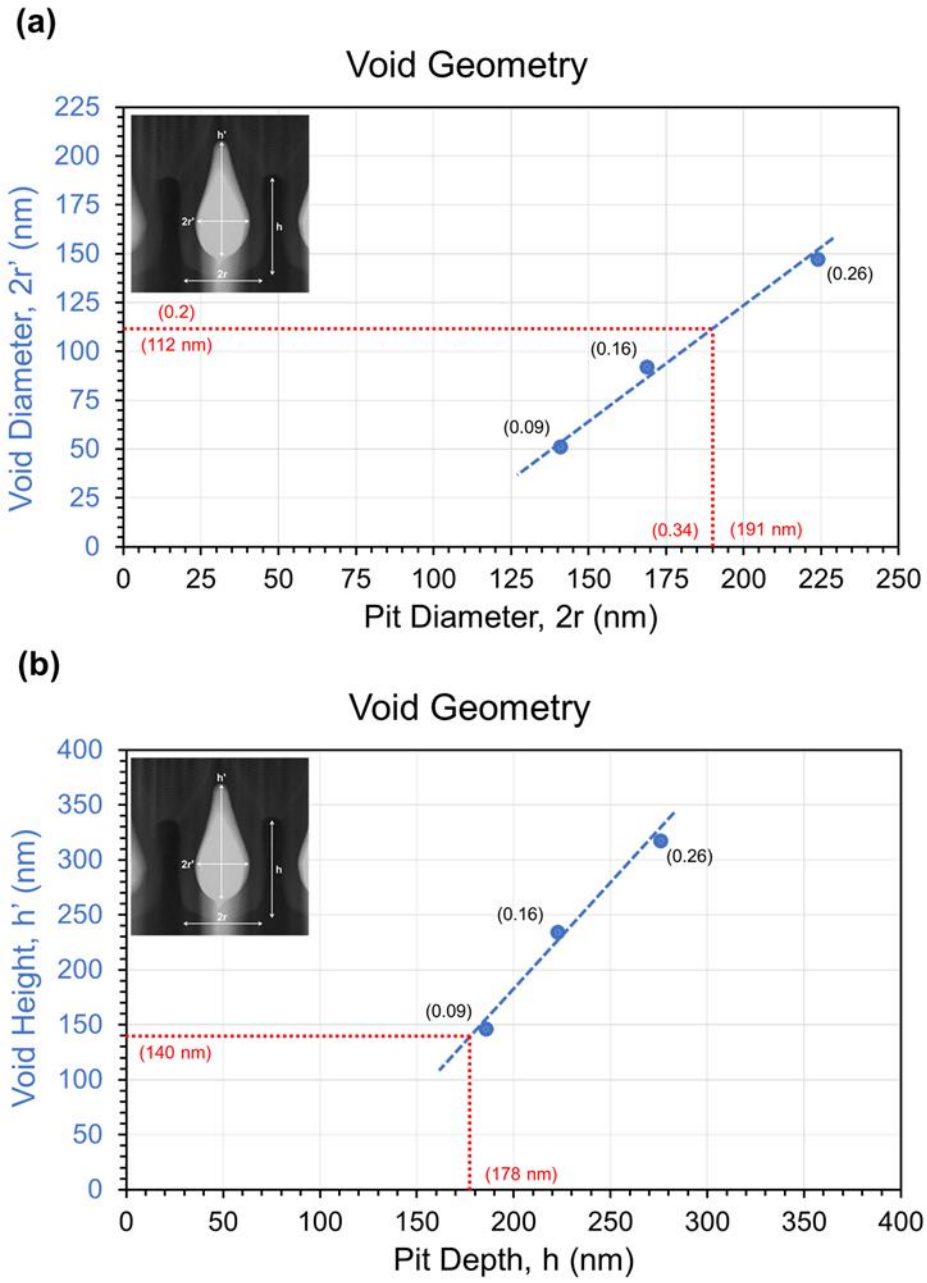

Figure 4.9. Plots showing the trends in void dimensions compared with the corresponding pit dimension. (a) Void diameter, 2r' as a function of initial pit diameter, 2r. The equivalent r/a of the void is shown in brackets. (b) Void height, h' as a function of initial pit depth, h. No void displays optimal values of 2r' and h', which are indicated in red on the y-axis their respective plots. Interpolated starting pit dimensions required to achieve these values are indicated in red on the x-axis.

inverted with respect to that seen in ADF images, with voids appearing as white, high-intensity features (as no material exists in these regions to perturb the incident electrons). In both of the additional samples, voids have again formed during regrowth. As discussed in Section 4.2., the PC structures were etched under the same RIE conditions, resulting in a pit depth that varied with the r/a of the grating. As the diameter, $2r$, and depth, h, of the initial pit decreases, so too do the diameter, $2r'$, and height, h', of the voids. The dimensions of the pits and voids are summarised in Table 4.1., and void diameter (a) and height (b) are plotted as a function of the corresponding pit dimension in Figure 4.9.

In the context of ideal void dimensions for device applications, two r/a' ($2r'$) values, 0.4 (224 nm) and 0.2 (112 nm), are of interest as configurations where the grating coupling strength is maximised [19], and a height (h') of 0.5a (141 nm) is desired for optimal vertical radiation constant [20]. Whilst no individual example presented here meets either of these criteria, a number of observations regarding the optimisation of void size by tuning of initial grating pit dimensions can be made based on the trends seen in Figure 4.9. Firstly, for the pit geometries studied, the diameter of the voids formed will always be smaller than that of the pit due to significant deposition on the sidewall planes. This effectively eliminates the possibility of achieving an r/a' value of 0.4 as this would require an initial $2r$ value of greater than 281 nm (i.e., a value larger than the PC period, a). However, an r/a' value of 0.2 appears to be accessible using an initial $2r$ (r/a) value of approximately 191 nm (0.34), allowing for potential optimisation of PC geometry around at least one of the coupling maxima. Secondly, extrapolation from the trend in void height

suggests that an optimum void height might be achieved utilizing an initial pit depth of 178 nm.

It is noted that, in this study, a grating pit with nominal diameter of 191 nm would have a corresponding depth much larger than 178 nm (according to the trend in Figure 4.1(b)) due to etch times being selected to achieve the desired depths for 0.4 *r*/*a* structures. However, in principle, an arbitrary pit depth within the range of interest for seeded regrowth of void-containing PCs (less than 500 nm) may be realised for any given diameter by optimisation of the RIE process. PC structures with the dimensions defined above represent the starting point for a future study considering the relationship between pit dimensions and void geometry. Whilst the study presented here considered grating pits for which both diameter and depth varied simultaneously, future efforts to optimise the initial pit geometry should be performed in an iterative manner in which only one parameter (pit depth) is varied at a time whilst the other (pit diameter) is held constant (or vice versa). Such a study would allow for fine-tuning of void geometries compared with the initial optimisation discussed here.

4.6. Effects of Substrate Orientation

In order to assess the effect substrate orientation on grating infill dynamics and void formation, additional 0.3 *r*/a PC structures were prepared on $(311)B$ orientated substrates. Orthogonal cross-sectional SEM images of (100) and $(311)B$ orientated samples following regrowth with AlGaAs are shown in Figure 4.10. The voids in the (100) PC (which are the same as those presented in Section 4.5) have an *h'* and *2r'*

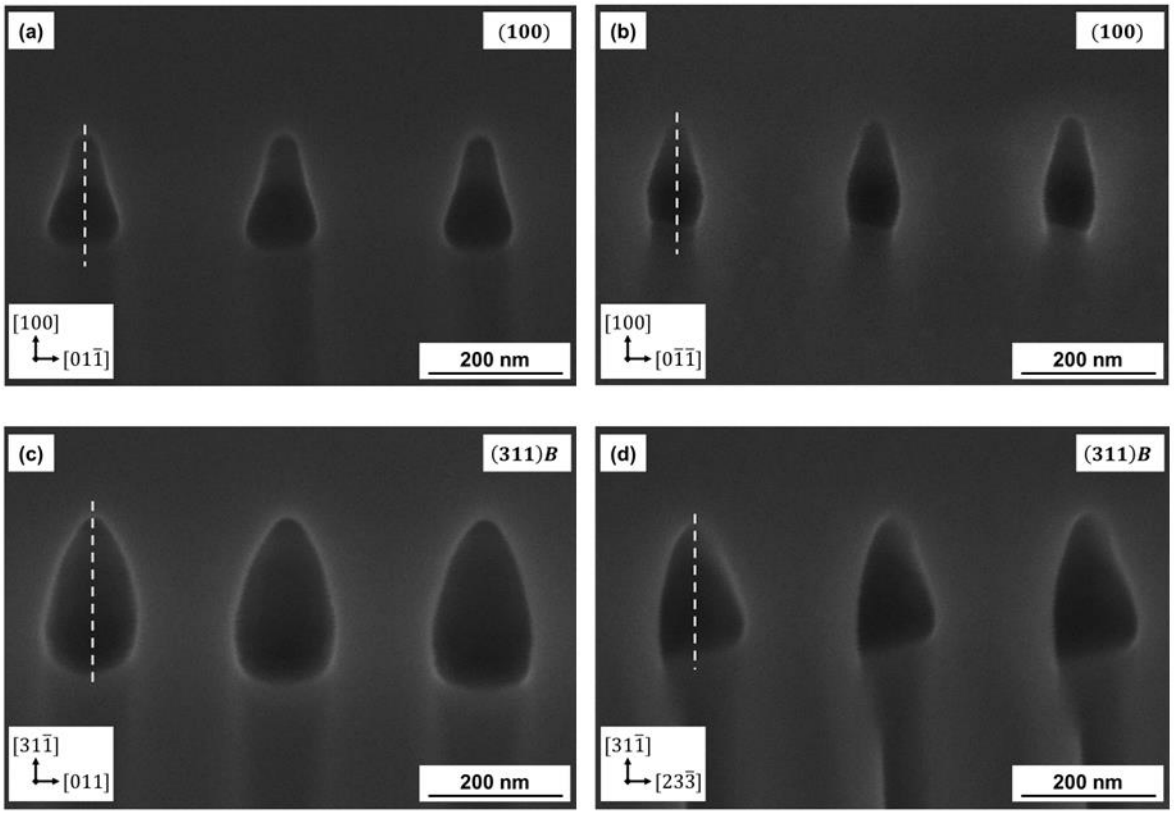

Figure 4.10. Cross-sectional SEM images of voids in 0.3 *r*/*a* PC structures on (100) (a,b) and $(311)B$ (c,d) orientated substrates following regrowth with AlGaAs, as viewed along both PC axes. Voids in the $(311)B$ sample are significantly larger than those on (100). In addition to a greatly enhanced asymmetry within the plane of the PC, voids on $(311)B$ substrates display a much more complex out-of-plane asymmetry compared with (100). Whilst voids on (100) are symmetric about a mirror plane in the z direction (as indicated by the dashed white line), the mirror symmetry is broken for voids on $(311)B$ when viewed along the $[0\bar{1}\bar{1}]$ direction (d).

of 234 nm and 92 nm, respectively. By contrast, the voids in the $(311)B$ PC are significantly larger in both dimensions, with an *h'* and *2r'* of 335 nm and 150 nm, respectively. In part, the increase in void height can be attributed to a larger initial pit depth for $(311)B$ structures (*h* = 315 nm) (as determined by STEM imaging, below) compared with those on (100) substrates (*h* = 223 nm). The extent to which the increase in pit depth is the result of sample-to-sample variations at the PC etch stage or is related to an orientation-dependent difference in etch rates for the two

substrates is unclear at this stage [11,27]. However, the differing pit dimensions are not expected to greatly alter the overall analysis presented below, which focuses on void shape rather than on the optimisation of dimensions. It is noted that in future work concerning the optimisation of void geometry or the fabrication of PCSELs on substrates with non-standard orientations, care should be taken to study the PC etch kinetics and to develop a process which allows complete comparison with those on (100) wafers.

In addition to the differences in void dimensions, Figure 4.10. reveals a significant difference in the three-dimensional shape of the voids between the two substrate orientations. Considering the orthogonal cross-sections in panels (a) and (b), voids in (100) structures display the same in-plane asymmetry as described for 0.4 *r*/*a* structures in Section 4.4. Out-of-plane, the void profile in each of the cross-sections is characterised by a plane of mirror symmetry along the $[100]$ axis (i.e., in the growth direction), as highlighted by the dashed white line. For voids on $(311)B$, the void shape seen in the $[23\bar{3}]$ cross-section (panel c) retains the same out-of-plane mirror symmetry, however the $[0\bar{1}\bar{1}]$ profile (panel d) is characterised by a high degree of asymmetry in the growth direction, resulting in a greatly enhanced in-plane asymmetry compared with (100) substrates.

The reduced symmetry of the void shape obtained for $(311)B$ substrates can be understood by considering the relative orientations of internal crystal planes for this surface compared with (100) substrates. A schematic showing the key crystal plane directions for each wafer orientation is shown in Figure 4.11(a), as viewed along both the major and minor flat directions. The $(311)B$ orientation is related to the (100) surface by a rotation of 25° around the $[0\bar{1}\bar{1}]$ axis. As a result, the axes of the PC on

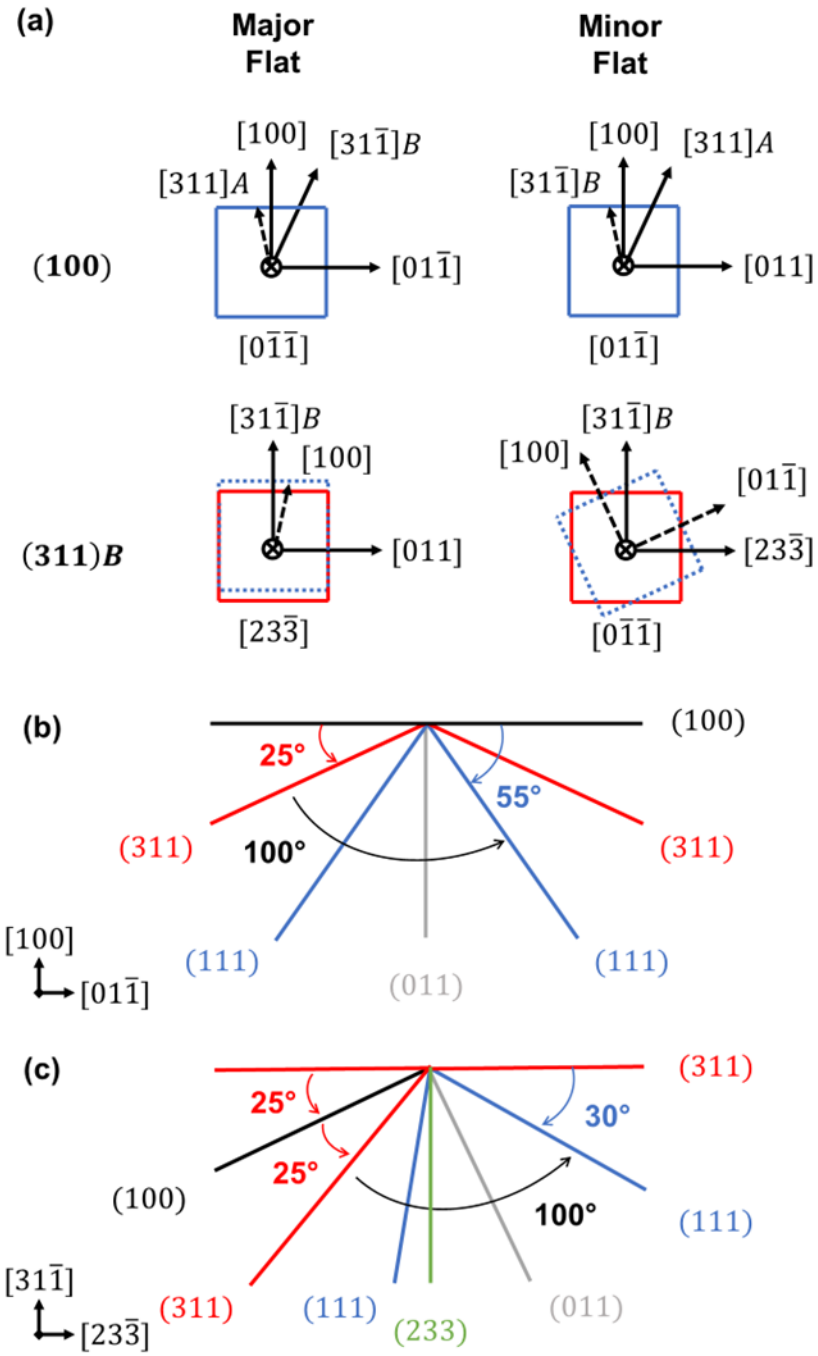

Figure 4.11. Schematic diagrams illustrating (a) the relative crystal plane directions in (100) and $(311)B$ orientated wafers, as viewed along the major and minor flat directions, and the symmetry of internal crystal planes for a (b) (100) and (c) $(311)B$ surface as viewed along the $[0\bar{1}\bar{1}]$ direction. The $(311)B$ orientation is achieved by a 25° rotation about the $[0\bar{1}\bar{1}]$ axis. In (100) orientated samples, internal planes are equivalent and have mirror symmetry about the (011) plane. For $(311)B$ orientated surfaces, the mirror symmetry is broken, and internal planes are inequivalent about the (233) axis.

this substrate are aligned along two inequivalent crystal plane directions, $[0\bar{1}\bar{1}]$ and $[23\bar{3}]$, compared with the equivalent $\{110\}$ planes for (100) wafers. In this context, the (100) major flat and $(311)B$ minor flat directions both align along the same $[0\bar{1}\bar{1}]$ axis, however the cross-sections are geometrically inequivalent due to rotation.

The inequivalence of the $[0\bar{1}\bar{1}]$ cross-sections is demonstrated in Figure 4.11(b) & (c), which show the orientation of internal planes for the respective substrate surfaces. For the (100) orientation, the internal $\{111\}$ and $\{311\}$ have mirror symmetry about the (011) plane [11]. This results in a symmetric growth front during regrowth and cross-sectional void profiles that symmetric with respect to the growth direction, as described in Figure 4.6 and Figure 4.10(a) & (b). For the $(311)B$ orientation, in contrast, the mirror symmetry is broken by the 25° rotation, with the pair of $\{111\}B$ planes becoming geometrically inequivalent about the (233)-plane. Importantly, it is now the case that there is a single internal $(311)B$ plane present in the cross-section, which forms a geometrically inequivalent pair with the surface $(311)B$ plane [11,29]. Here, the reduced symmetry of the internal crystal planes with respect to the $[311]$ axis results in an asymmetric growth front and the loss of mirror symmetry in the void profile, as seen in Figure 4.10(d). As the translation from the (100) to $(311)B$ orientation is realised by a rotation about only the $[0\bar{1}\bar{1}]$ axis, the mirror symmetry of the internal planes about the $[311]B$ axis, and hence the resulting void profile, is retained for the $[23\bar{3}]$ cross-section (Figure 4.10(c)).

The role of crystal plane symmetries in dictating the shape of the voids in $(311)B$ samples can be seen clearly in the STEM images in Figure 4.12, in which panels (c) and (d) show higher magnification images of the evolving growth front in the coalescence region above the void. In the $[23\bar{3}]$ cross-section, growth initiates from

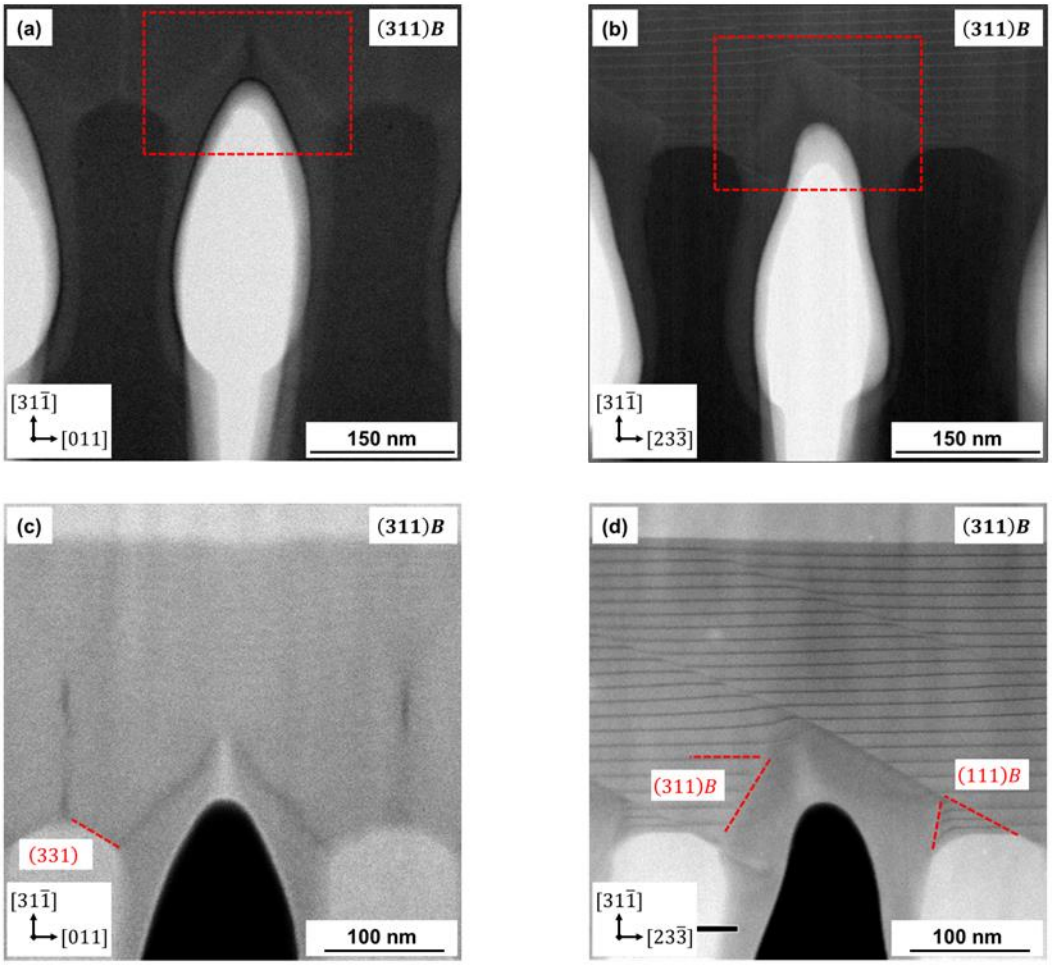

Figure 4.12. Cross-sectional BF-STEM images of voids in 0.3 r/a PC structures following regrowth with AlGaAs, as viewed along the (a) $[23\bar{3}]$ and (b) $[0\bar{1}\bar{1}]$ directions. The degree of out-of-plane symmetry in the cross-sectional void shape is a consequence of a (a) symmetric or (b) asymmetric growth profile, as seen in the coalescence region above the voids (highlighted in the red dashed boxes). Higher magnification, ADF-STEM images of these regions are shown in (c) and (d), respectively. As viewed along the $[23\bar{3}]$ direction, growth proceeds from symmetric (331) planes at the top of the grating. As viewed along the $[0\bar{1}\bar{1}]$ direction, growth proceeds vertically and laterally from geometrically inequivalent $(311)B$ planes, forming diagonally propagating domains separated by $(111)B$ non-growth planes.

a set of equivalent $\{331\}$ planes at the top of the grating [30] and proceeds laterally at equal rates towards the coalescence point, producing a void that is symmetric with respect to the $[311]B$ axis. In the $[0\bar{1}\bar{1}]$ cross-section, by contrast, growth proceeds vertically and laterally from the two geometrically inequivalent $(311)B$ planes. This leads to the formation of diagonally propagating, domain-like growth fronts that appear to terminate along a $(111)B$ boundary. As a result, the void profile is asymmetric with respect to the $[311]B$ axis.

In the context of achieving optimised PC geometries for device applications, the enhanced in-plane and out-of-plane asymmetry seen for voids in $(311)B$ samples compared with (100) is expected to be beneficial. This should allow higher output powers thorough the reduction of destructive interference of light scattered vertically from the PC layer, resulting in higher out-of-plane scattering [13, 24, 25].

4.7. Discussion & Future Work

The results of Section 4.3. suggest that the extent of grating infill and void formation during regrowth of PC structures is strongly dependent on the surface mobility of the atomic species present in the infill layer. This is in agreement with previously reported regrowth studies related to the GaAs/InGaP [7] and InP [8] PC systems in which the degree of infilling was tuned through the choice of growth condition. In this study, which is the first of its kind reported for the (Al)(Ga)As/GaAs PC system, the inherent surface mobilities associated with aluminium and gallium (and their alloys) can be considered as an analogue to the mobility promoted by choice of growth condition. The decrease in void size associated with the increasing mole

fraction of highly mobile gallium in the infill layer mirrors the effect reported where the surface mobility of species was enhanced through a relative increase in the growth temperature or decrease in the growth rate and/or V/III ratio [7,8]. Importantly, the extreme cases of infilling observed for AlAs and GaAs regrowth can be thought of as bookending the tuning range of void sizes accessible in this PC system, suggesting that optimum void geometries or complete all-semiconductor infill may be achieved when using AlGaAs.

There are two key avenues of exploration open to future work in this regard. Firstly, as suggested above, a study of void dimensions over a range of AlGaAs gallium mole fractions would be important, complementing the results presented here. Additionally, an investigation of void engineering for different regrowth conditions should be undertaken as part of efforts to realise an optimised regrowth process for the fabrication of PCSELs.

In Section 4.4. it was shown that voids formed during regrowth are asymmetric with respect to the axes of the PC grating. This is known to be an important characteristic required for achieving high-power devices [24,25], and had previously only been demonstrated where asymmetric pit geometries such as right-angled triangles were used [13]. The fact that an asymmetry arises from a nominally symmetric circular grating pit due to differences in crystal plane polarities in III-V materials suggests that more complex void shapes can be achieved in the case of AlGaAs regrowth though choice of regrowth conditions. This was demonstrated by voids in AlAs-regrown structures for which the dynamic faceting seen in the $[0\bar{1}\bar{1}]$ cross-section is compounded by the reduced adatom mobility, resulting in the enhanced in-plane asymmetry. The degree to which void shape asymmetry can be

engineered should form an important part of future regrowth studies, particularly those considering the effects of varying growth condition as this can affect the crystal plane kinetics in a system and may change the evolution of the growth front [3,4].

The work outlined in this chapter highlights the complex interplay between infill layer composition, growth conditions, and pit dimensions in determining the degree of infilling and void size. However, determining the correct combination of parameters experimentally through an iterative approach could prove to be financially costly and time consuming. The development of a computational model capable of accurately predicting void geometry from an arbitrary combination of the above parameters would be a significant next step in the development of PCSELs. Similar models already exist that can predict the formation of voids in other deposition systems [2,31], and it may be possible to adapt these to suit the needs of PC regrowth. The additional regrowth studies outlined above, together with the optimisation of initial pit dimensions proposed in Section 4.5., would allow for the quantification of kinetic parameters required for such a model, such as adatom surface mobility and vapour phase diffusion constants.

The enhanced asymmetry seen for voids on $(311)B$ substrates is expected to be useful in achieving high out-of-plane coupling from the PC layer [24,25] suggesting that $(311)B$ substrates may be a promising alternative platform for future use in achieving high output power PCSELs. In addition to exploiting the void asymmetry, use of $(311)B$ substrates would allow for the integration of more exotic, quantum dot (QD)-based gain elements, potentially opening GaAs-based devices to applications at longer emission wavelengths than are currently open to quantum well-based structures. QDs grown on $(311)B$ substrates have enhanced properties in terms

of high dot density and uniformity and low inhomogeneous linewidths [32,33], and offer a promising route to high-quality devices [34]. Future work on fabrication of PCSELs on $(311)B$ could also be extended to an InP platform for which this QD technology is more mature.

4.8. Conclusion

This chapter has presented a study of grating infill kinetics during MOVPE-regrowth of GaAs-based PCs composed of circular grating pits. Through cross-sectional SEM imaging of samples grown on (100) orientated substrates it was shown that, for nominally identical grating structures, void formation is strongly dependent on the surface mobility of the group-III species, as demonstrated by varying the composition of the infill layer. Use of high-mobility GaAs was shown to result in complete grating infill, whilst void formation was promoted by inclusion of low-mobility Al in AlGaAs and AlAs layers.

STEM analysis of the voids along both axes of the PC revealed an asymmetry in three-dimensional void shape which is attributed to the differing polarities of high-index planes along orthogonal crystal plane directions, with the higher incorporation rates of A-type planes compared to their B-type counterparts resulting in an elliptical void profile when considered in the plane of the PC. The differing polarities of these planes was also shown to affect the evolution of the growth front emanating from the top of the grating pit, with A-type planes giving rise to stable faceting, and B-type planes resulting in dynamic faceting. In the case of AlAs-regrowth, the different

faceting regimes along orthogonal axes is compounded by the low surface mobility, producing voids with a more complex shape asymmetry than those seen in AlGaAs.

For structures regrown with AlGaAs, the tuning range of void sizes was explored by varying the diameter and depth of the initial grating pit. Whilst none of the pit geometries investigated resulted in voids with the ideal height and r/a for use in devices, extrapolation from trends in plotted data suggests pit dimensions that should be used in future studies focused on achieving optimal void geometries.

Finally, it was shown that voids formed during regrowth of PC structures on $(311)B$ orientated substrates display a greatly enhanced in-plane asymmetry compared with those on conventional (100) substrates, and that they are also characterised by a significant out-of-plane asymmetry when considered along both axes of the PC. The increased asymmetry in void shape is expected to be beneficial to device performance, suggesting that $(311)B$ or other high-index surface substrates may be a promising alternative platform for use in PCSELs.

4.9. References

[1] A. F. McKenzie, B. C. King, K. J. Rae, S. Thoms, N. D. Gerrard, J. R. Orchard, K. Nishi, K. Takemasa, M. Sugawara, R. J. E. Taylor, D. T. D. Childs, D. A. MacLaren, and R. A. Hogg, "Void engineering in epitaxially regrown GaAs-based photonic crystal surface emitting lasers by grating profile design", Appl. Phys. Lett., 118, 021109 (2021)

[2] M. Salvalaglio, R. Backofen, and A. Voigt, “Thin-film dynamics with shadowing effects by a phase-field approach”, Phys. Rev. B, 94, 235432 (2016)

[3] L. Hofmann, A. Knauer, I. Rechenberg, and M. Weyers, “Overgrowth of trenched with (AlGa)As using metalorganic vapor-phase epitaxy (MOVPE)”, J. Cryst. Growth, 195, 485 (1998)

[4] L. Hofmann, A. Knauer, I. Rechenberg, M. Weyers, and W. Stolz, “Patterned growth of (AlGa)As using metalorganic vapor-phase epitaxy”, J. Cryst. Growth, 206, 255 (1999)

[5] G. Vermeire, I. Moerman, Z. Q. Yu, F. Vermaerke, P. Van Daele, and P. Demeester, “Atmospheric and low pressure metalorganic vapor phase epitaxial growth of vertical quantum wells and quantum wires on submicron gratings”, J. Electron. Mater., 23(2), 121 (1994)

[6] G. Biasiol, F. Reinhardt, A. Gustafsson, and E. Kapon, “Self-limiting growth of GaAs surfaces on nonplanar substrates”, Appl. Phys. Lett., 71, 1831 (1997)

[7] R. J. E. Taylor, D. M. Williams, D. T. D. Childs, B. J. Stevens, L. R. Shepherd, S. Khamas, K. M. Grrom, R. A. Hogg, N. Ikeda, and Y. Sugimoto, “All-semiconductor photonic crystal surface-emitting lasers based on epitaxial regrowth”, IEEE J. Select. Topics Quant. Electron., 19(4), 4900407 (2013)

[8] C. Reuterskiöld Hedlund, J. M. De Pina, A. Kalapala, Z. Liu, W. Zhou, and M. Hammer, “Buried InP/airhole photonic-crystal surface-emitting lasers”, Phys. Status Solidi A, 218, 2000416 (2021)

[9] L. Hoffman, A. Knauer, I. Bechenberg, U. Zeimer, and M. Weyers, “Comparison of binary and ternary growth over trenches using MOVPE”, J. Cryst. Growth, 213, 229 (2000)

[10] E. Kapon, F. Reinhardt, G. Biasiol, and A. Gustafsson, “Surface and interface properties of quantum nanostructures grown on nonplanar substrates”, Appl. Surf. Sci., 123, 674 (1998)

[11] M-S. Kim, Y. Kim, M-S. Lee, Y. J. Park, S-Il. Kim, S-K. Min, “The facet evolution during metalorganic vapor phase epitaxial growth on V-grooved high Miller index GaAs substrates”, J. Cryst. Growth, 139, 231 (1994)

[12] M-S. Kim, Y. Kim, M-S. Lee, Y. J. Park, S-Il. Kim, S-K. Min, “Growth behaviour on V-grooved high Miller index GaAs substrates by metalorganic chemical vapor deposition”, J. Cryst. Growth, 146, 482 (1995)

[13] M. Yoshida, M. Kawasaki, M. De Zoysa, K. Ishizaki, A. Hatsuda, and S. Noda, “Fabrication of photonic crystal structures by tertiary-butyl arsine-based metal-organic vapor-phase epitaxy for photonic crystal lasers”, Appl. Phys. Express, 9, 062702 (2016)

[14] A. Larrue, D. Belharet, P. Dubreuil, S. Bonnefont, O. Gauthier-Lafaye, A. Monmayrant, and F. Loses-Dupuy, “Inductively coupled plasma etching of high aspect ratio two-dimensional photonic crystal gratings in Al-rich AlGaAs and AlGaAsSb”, J. Vac. Sci. Technol. B, 29,021006 (2011)

[15] M. Volatier, D. Duchesne, R. Morandotti, R. Arès, and V. Aimez, “Extremely high aspect ratio GaAs and GaAs/AlGaAs nanowaveguides fabricated using chlorine ICP etching with N2-promoted passivation”, Nanotechnol., 21, 134014 (2010)

[16] M. Schaffer, B. Schaffer, and Q. Ramasse, “Sample preparation for atomic-resolution STEM at low voltages by FIB”, Ultramicroscopy, 114, 62 (2012)

[17] D. C. Joy and J. B. Pawley, “High-resolution scanning electron microscopy”, *Ultramicroscopy*, **47**, 80-100 (1992)

[18] J. I. Goldstein, D. E. Newbury, J. R. Michael, N. W. M. Ritchie, J. H. J. Scott, D. C. Joy, *Scanning Electron Microscopy and X-Ray Microanalysis*, New York, NY, USA; Springer

[19] R. J. E. Taylor, D. M. Williams, J. R. Orchard, D. T. D. Childs, S. Khamas, and R. A. Hogg, “Band structure and waveguide modelling of epitaxially regrown photonic crystal surface-emitting lasers”. J. Phys. D.: Appl. Phys., 46, 264005 (2013)

[20] S. Iwahashi, K. Sakai, Y. Kurosaka, and S. Noda, “Air-hole design in a vertical direction for high-power two-dimensional photonic-crystal surface-emitting lasers”, J. Opt. Soc. Am. B, 27(6), 2010

[21] R. Nötzel, M. Ramsteiner, J. Menniger, A. Trampert, H-P. Schönherr, L. Däweritz, and K. H. Ploog, “Patterned growth on high-index GaAs (n11) substrates: application to sidewall quantum wires”, J. Appl. Phys., 80, 4108 (1996)

[22] M. Paladugu, C. Merckling, R. Loo, O. Richard, H. Bender. J. Dekoster, W. Vandervorst, M. Caymax, and M. Heyns, “Site selective integration of III-V materials on Si for nanoscale logic and photonic devices”, Cryst. Growth Des., 12, 4696-4702 (2012)

[23] E. Pelucchi, V. Dimastrodonato, A. Rudra, K. Leifer, and E. Kapon, “Decomposition, diffusion, and growth rate anisotropies in self-limited profiles during metalorganic vapor-phase epitaxy of seeded nanostructures”, Phys. Rev. B, 83, 205409 (2011)

[24] Y. Kurosaka, K, Sakai, E. Miyai, and S. Noda, “Controlling vertical optical confinement in two-dimensional surface-emitting photonic-crystal lasers by shape of air holes”, Optics Express, 16(22), 18485 (2008)

[25] C. Peng, Y. Liang, K. Sakai, S. Iwahashi, and S. Noda, “Coupled-wave analysis for photonic-crystal surface-emitting lasers on air holed with arbitrary sidewalls”, Optics Express, 19(24), 24672 (2011)

[26] S. D. Hersee, E. Barbier, and R. Blondeau, “A Study of the orientation dependence of Ga(Al)As growth by MOVPE”, J. Cryst. Growth, 77, 310 (1986), 77, 310 (1986)

[27] A. Bakin, G. Zwinge, R. Klochenbrink, H-H. Wehmann,and A. Schlachetzki, “Simulation of the orientation-dependent growth of InGaA/InP by metalorganic vapor-phase epitaxy”, J. Appl. Phys., 76, 4906 (1994)

[28] S. Tanaka, K. Sonoda, K. Kasai, K. Kanda, T. Fujita, K. Higucho, and K. Maenaka, “Crystal orientation dependent etching in RIE and its applications”, 2011 IEEE 24th International Conference on Micro Electro Mechanical Systems, 217 (2011)

[29] Z. Niu, R. Nötzel, U. Jahn, H-P. Schönherr, J. Fricke, and K. H. Ploog, “Self-limiting MBE growth and characterisation of three-dimensionally confined nanostructures on patterned GaAs (311)A substrates”, J. Electron Mater., 28(1), 1 (1999)

[30] R. Nötzel, J. Menniger, M. Ramsteiner,A. Ruiz, H-P. Schönherr, and K. H. Ploog, “Selectivity of growth on patterend GaAs (311)A substrates”, Appl. Phys. Lett., 68, 1132 (1996)

[31] A. Barzaghi, S. Firoozabadi, M. Salvalaglio, R. Bergamaschini, A. Ballabio, A. Beyer, M. Albani, J. Valente, A. Voigt, D. J. Paul, L. Miglio, F. Montalenti, K. Volz, and G. Isella, “Self-assembly of nanovoids in Si microcrystals epitaxially grown on deeply patterned substrates”, Cryst. Growth Des., 20, 2914 (2020)

[32] K. Akahane, T. Kawamura, K. Okino, H. Koyama, S. Lan, Y. Okada, and M. Kawabe, “Highly packed InGaAs quantum dots on GaAs (311)B”, Appl. Phys. Lett., 73(23), 3411 (1998)

[33] P. Caroff, N. Bertru, A. Le Corre, O. Dehaese, T. Rohel, I. Alghoraibi, H. Folliot, and S. Loualiche, “Achievement of high density InAs quantum dots on InP (311)B substrates emitting at 1.55 μm”, Jap. J. Appl. Phys., 44(34), L1069 (2005)

[34] R. Kaneko, R. Morita, R. Katsuhara, R. Yabuki, A. Matsumoto, K. Akahane, Y. Matsushima, H. Ishikawa, and K. Utaka, “1500 nm-band InAs/InGaAlAs quantum dot distributed feedback laser grown on InP(311)B substrate with side wall gratings simultaneously fabricated with a ridge waveguide”, Phys. Status Solidi A, 219, 2100453 (2022)

Chapter 5 |

Selective Area Growth of InGaAs/GaAs MQW Active Structures

This chapter presents a study into InGaAs/GaAs multi-quantum well (MQW) structures selectively grown by metalorganic vapour phase epitaxy (MOVPE) in large, two-dimensional (2D) growth windows masked by SiO_2. The dimensions of masked areas are chosen to reflect the typical geometries of photonic crystal surface emitting lasers (PCSELs), and the purpose of the investigation is to assess the suitability of selective area growth (SAG) as a technology for achieving surface emitting laser arrays with widely tuneable wavelengths.

The growth rate enhancement (GRE), emission wavelength tuning range, and indium composition variations of the quantum well material is determined for square masked regions with feature sizes up to 300 x 300 μm^2. Through micro-photoluminescence (μ-PL) measurements at the centre point of each of the growth windows, a total wavelength tuning range of 86 nm is observed across all samples,

with a typical tuning range of 30 nm for a given window width. The thickness enhancement in each of the features is determined by optical white-light interferometry (WLI) profiling, indicating that centre point GREs of between 1.19 - 2.23 x can be achieved with respect to the nominal epi structure by varying the width of the dielectric mask. By comparing the observed emission wavelengths with those simulated using the enhanced quantum well thicknesses, a range of indium compositions between 12 – 17 % is calculated for the material at the centre of each feature.

The initial centre point analysis is extended to two-dimensions for selected features through μ-PL mapping of the entire growth window in order to determine the dimensions of the region with a uniform emission wavelength. Large areas with dimensions up to 100 x 100 μm^2 are observed in which the emission wavelength is uniform within ± 2 nm of the centre point value suggesting that, with future optimization of mask geometries and growth conditions, selective area growth may be successfully employed in the fabrication of photonic crystal surface emitting lasers.

5.1. Motivation

The potential for achieving high-power, single-mode emission across a wide range of wavelengths makes PCSELs the ideal candidate for use in surface emitting laser arrays [1,2]. Previous work in this regard has demonstrated coherent control of individual elements and power-scaling through the coupling of devices in PCSEL arrays, however the devices in these cases were limited to a single wavelength [3-5]. The ability to realise a monolithically integrated multicolour array, whereby devices fabricated on

the same substrate emit over a range of wavelengths, would signify an important step in the development of PCSEL technology, allowing use in wavelength division multiplexing and sensing applications which require a multiwavelength source.

Recently, the monolithic fabrication of PCSELs at four different wavelengths was demonstrated in InP-based materials, with room-temperature continuous-wave lasing across a 40 nm wavelength range from 1300 – 1340 nm being reported [6]. The wavelength tuning was achieved using a common active material by varying the period of the photonic crystal (PC) grating to accommodate four separate lasing modes across a single gain band. Whilst, in principle, the cavity mode of a PC can be designed to span more than 100 nm for a given PC system [7], the range of wavelengths accessible to a monolithic array realised in this manner is expected to be less than 50 nm, due to the limited gain bandwidth of MQW active regions and the deleterious effects on device performance associated with a large detuning of the lasing mode (i.e. PC mode) from the gain peak for the active region [8].

A common way of expanding the wavelength range available to multicolour laser arrays is to spatially vary the composition of the gain material on the wafer. Traditionally, this has been achieved by SAG of MQW laser structures on wafers which have been pre-patterned with a series of growth windows enclosed by areas of dielectric material [9]. The presence of an amorphous dielectric material (such as SiO_2) on the surface of the wafer acts as a mask, preventing deposition of the epi layers on those regions. As a result, there is a net diffusion of material into the adjacent growth windows leading to enhancement of the growth rate and thickness of the MQW stack, and a red-shift of the emission wavelength. The details of the growth dynamics in SAG are explored further in the following section, however the

key principle of SAG is that the degree of the GRE, wavelength shift, and uniformity of the selectively grown material can be tuned considerably by varying the relative widths of the SAG window and mask [10]. By exploiting this principle, multi-channel laser arrays with wavelength ranges spanning up to 150 nm have been successfully fabricated in the past [11,12], highlighting the potential for significantly expanding the wavelength agility of monolithic PCSEL arrays.

In the context of application of SAG to PCSELs, two key challenges can be identified: the 2D nature of the devices (i.e., the requirement for a 2D PC grating layer), and the large device area required for efficient operation, which is generally considered to be greater than 100 x 100 μm^2 [7]. To date, the development of conventional MQW SAG technology has been focused almost exclusively on devices with one dimensional (1D) geometries, such as buried-heterostructure lasers [11,13], integrated laser-modulator structures [14], or photonic integrated circuits [15]. Such devices typically require uniform gain material with a width on the order of 10 - 20 μm for successful fabrication of devices (at least one order of magnitude less than required for a PCSEL). Consequently, the SAG mask geometries reported in literature typically consist of window widths between 20 and 60 μm, with mask widths varying by up to as much as ten times the window width. In the case of the few examples where window widths exceeding 100 μm have been reported, data on the level of GRE and wavelength shift for the InGaAs/GaAs MQW system was limited to a single mask width, and no extensive study of the tuning range were reported [16-18].

Work on 2D SAG, on the other hand, has been focused on the development of nano- and micro-structures such as micro-pyramids [19], nano-pillar arrays [20], or site-selective growth of quantum dots and quantum wires [21]. In these cases, the

feature sizes used are typically on the order of a few microns or less, so they provide little insight into the growth of planar MQW structures on the 10's or 100's μm scale.

To the best of my knowledge, this work presents the first study of MQWs selectively grown in large area 2D SAG windows with dimensions up to 300 x 300 μm^2. Initially, the range of accessible thickness enhancements and emission wavelength shifts are determined by white light interferometry (WLI) profiling and μ-PL measurements, respectively, for a matrix of samples with varying window and mask widths. Then, the relative indium composition for each of the InGaAs/GaAs MQW structures is determined by comparing the observed QW emission wavelengths with those calculated using the enhanced QW thicknesses. Finally, the uniformity of the material within the SAG window is determined for selected features using 2D μ-PL mapping.

5.2. Selective Area Growth

In order to explore the origins of the GRE and emission wavelength shift in selectively grown MQW structures, consider the case of conventional 1D SAG. A schematic of the typical mask geometry used in this case is shown in Figure 5.1(a). Two dielectric stripes of length, L, and width, W, are deposited on the surface of the wafer, separated by an opening of width, Λ, which defines the SAG window. The growth dynamics in the open and masked regions of the wafer are best described in the terms used in vapour-phase diffusion models which have been developed extensively for predicting the growth profiles in the 1D systems described in section 5.1. [9,10]. A

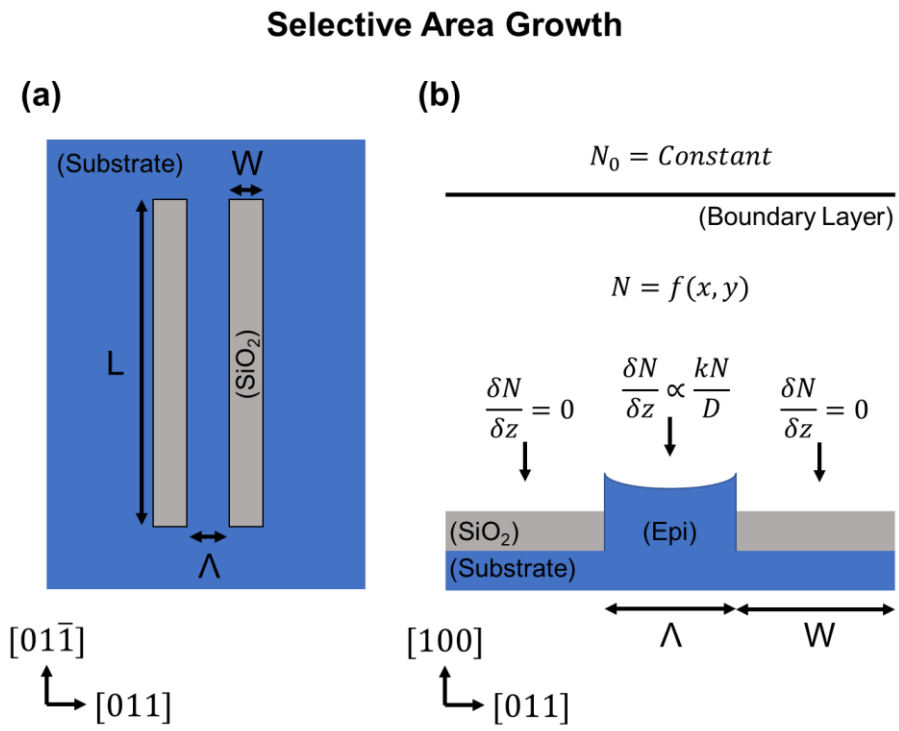

Figure 5.1. (a) Schematic plan-view diagram showing the mask layout in conventional 1D SAG. Two stripes of SiO_2 with width, W and length, L are separated by an unmasked window region with width, Λ. (b) Cross-sectional schematic describing the growth dynamics in SAG. For a reactant species with a vapour-phase concentration, N, growth in the unmasked region is determined by the effective diffusion constant, D and surface reaction rate constant, k. No deposition occurs on the SiO_2 mask due to a low surface reaction rate. The thickness profile of the epi layer is parabolic due to a lateral gradient in reactant concentration in the boundary layer above the mask.

modified version of the unit cell description used in such models is shown in Figure 5.1(b) and is introduced here as a visual aid for describing the reaction rate dynamics.

Consider the case of SAG of a binary III-V material. A reactant group-III species with concentration, N, crosses into the boundary layer and diffuses towards the wafer surface. When the species reaches the SAG window it adsorbs, decomposes, and incorporates into the epi layer as it would in conventional growth. The growth rate is then proportional to the concentration gradient, $\partial N/\partial z$ above the window and is

determined by the surface reaction rate constant, k and the effective gas-phase diffusion constant, D for the reactant species [22]. As with conventional MOVPE epitaxy, growth is mass transport-limited, and is independent of the group-V concentration, which is assumed to be in a large excess. Owing to the low sticking probability of reactant species on the SiO_2, the surface reaction rate on the dielectric is low (i.e., $k \sim 0$) and there is a low probability of nucleation on the mask [22].

The spatial variation in reaction rates creates a situation where there is a large concentration gradient in the gas phase normal to the surface of the exposed region, as reactants are consumed, and effectively zero concentration gradient normal to the mask surface. Consequently, reactants in the boundary layer above the mask preferentially diffuse laterally towards the window and deposit there, resulting in a GRE within the window compared with that in a region far from the proximity of the dielectric mask. Due to this preferential diffusion, a lateral concentration gradient is also produced above the window [23]. This results in a non-uniform GRE across the opening, with a much larger enhancement observed directly adjacent to the mask, decreasing towards the centre of the window. Because of this, selectively grown material generally exhibits a concave thickness profile [24].

For growth of MQW structures, the GRE within the SAG window results in thicker wells compared with those grown in non-masked areas, resulting in a red-shift in the QW emission to longer wavelengths than that of the nominally grown structure [25]. The emission wavelength of the QW shares the same concave distribution across the window as well thickness, with much longer wavelengths observed next to the mask. Where the QW is composed of a ternary or quaternary material, such as InGaAs or AlGaInAs, the distribution of emission wavelengths is further complicated by the

differing diffusion coefficients of the group-III species. The effective diffusion coefficient of a reactant species is inversely proportional to its molecular mass, therefore Ga-containing precursors (e.g. TMGa) exhibit much longer diffusion lengths than the equivalent In-containing precursor [15,26]. Consequently, the composition of the QW is typically anisotropic across the window where its width is greater than 10 μm, with a much larger indium mole fraction observed next to the mask, significantly enhancing the emission wavelength red-shift [22].

The extent of the GRE and emission red-shift for a given MQW structure can be tuned solely by varying the dimensions of the SAG window and dielectric mask, with an increasing ratio of masked to-exposed area producing larger reactant concentration gradients, and therefore larger enhancements [10]. In principle, this allows for a large on-wafer variations in wavelength to be achieved through careful design of the SAG mask, with tuning ranges greater than 100 nm having been demonstrated for lasers with 1D geometries [12,13].

At this point it is reiterated that the purpose of this work is not the development of a vapour-phase diffusion model describing large-area SAG in 2D features, or for empirical determination of the reaction parameters introduced above; though, this would be an important direction for future work on the development of SAG for PCSELs. To do so would require a more extensive study which included the growth of the individual binary components of the QW alloy over the same SAG features, and growth under a range of growth conditions [26]. This work seeks only to present an initial study into the GRE and emission wavelength tuning range of MQWs in features with dimensions greater than 100 x 100 μm^2, for which extensive investigations are missing from the current body of SAG literature.

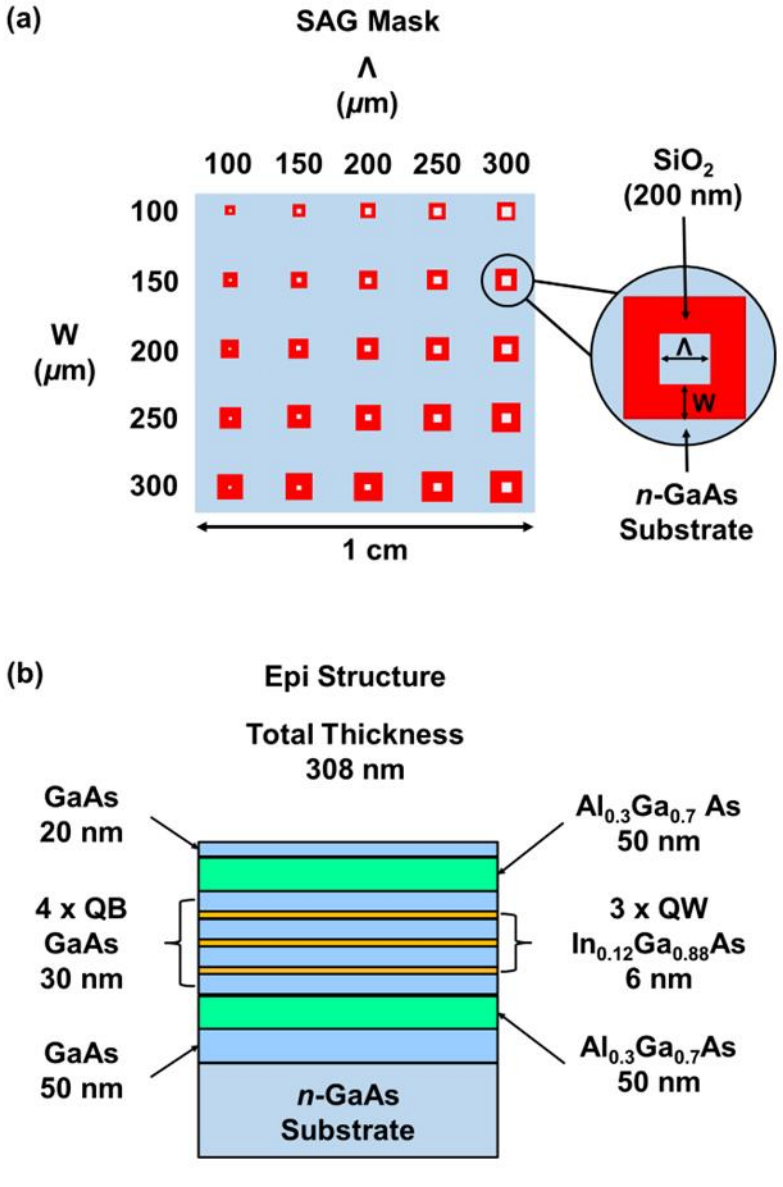

Figure 5.2. (a) Plan-view schematic showing the distribution of masked SAG regions on the wafer. Features form a 5x5 array with centre-to-centre distance of 2 mm, with the SiO_2 mask shown in red. The window width, Λ, and mask width, W, vary between 100 and 300 μm. The thickness of the SiO_2 mask is 200 nm. (b) Cross-sectional schematic of the deposited epi structure. The MQW structure consists of three 6 nm thick $In_{0.12}Ga_{0.88}As$ quantum wells (QWs), tuned to emit at 945 nm, separated by 30 nm GaAs barriers (QBs). The nominal thickness of deposited material in un-masked regions is 308 nm.

5.3. Sample Preparation and Measurement

A five-by-five array of square SAG regions were defined on bare epi-ready *n*-GaAs substrates orientated with a 2°-offcut from the (100) plane towards $(1\bar{1}0)$. Following deposition of a 200 nm-thick SiO_2 layer on the surface of the wafer, masked regions were defined by conventional photolithography and reactive ion etching such that their edges aligned along the $\{110\}$ crystal plane directions. The widths of the SiO_2 masks, W, and the open SAG windows, Λ, were varied from 100 to 300 μm, in 50 μm increments, giving 25 regions with unique W and Λ combinations. A schematic of the mask layout is shown in Figure 5.2(a). The centre-to-centre distance between SAG windows was set at 2 mm in order to prevent vapour-phase interactions between neighbouring regions [26], and the total dielectric coverage on the wafer was approximately 8.5%.

The epitaxial structure was deposited by metalorganic vapour phase epitaxy (MOVPE) in a Thomas Swan closed-coupled showerhead reactor utilising trimethylaluminium (TMAl), trimethylgallium (TMGa), trimethylindium (TMIn), and arsine (AsH3) as precursors. The undoped structure, a cross-sectional schematic is shown in Figure 5.2(b), consisted of three 6 nm-tick $In_{0.12}Ga_{0.88}As$ QWs tuned to emit at 945 nm in the field far from the SAG mask, and four 30 nm-thick GaAs barriers. The MQWs were confined between two 50 nm-thick $Al_{0.3}Ga_{0.7}As$ layers to help with carrier confinement and room-temperature PL intensity, and 50 nm and 20 nm-thick GaAs buffer and capping layers. The entire structure was grown at a temperature of 650 °C and pressure of 100 mbar, with the growth rate and V/III ratio for InGaAs growth set at 23 nm/min and 300, respectively. Growth conditions were chosen to minimise polycrystalline deposition on the large, masked areas, whilst ensuring high-

quality material in the field far from the oxide mask, in line with those reported for the same material system in the literature [17]. As it was necessary to remove the oxide mask surrounding the SAG window prior of material characterisation (as discussed below), no direct examination of the mask was carried out and it is unknown whether such polycrystalline material was present in this case. It is noted that the absence of complete selectivity should not significantly alter the analysis presented here, however it would affect the accuracy and reproducibility of VPD-based modelling developed for this system, and attempts should be made to quantify the extent of selectivity in future studies.

InGaAs QWs on GaAs were chosen as the material of interest for this initial study as they are required to access 900-1100 nm based devices. Additionally, their ternary composition significantly simplifies the analysis of the selectively grown material in comparison to GaInAsP and AlGaInAs quaternaries. In these cases, the inclusion of an additional group-V and group-III species, respectively, with yet again different diffusion characteristics, complicates the relationship between QW composition and emission wavelength across the growth window [15,26]. A low indium composition of 12% was chosen for the nominal QW structure so as to avoid the deleterious effects on material quality associated with high levels of strain in InGaAs layers containing greater than 20% In. Above this level, the strain in the layer is greater than 1.5% with respect to GaAs, and special care must be taken in choice of growth conditions or the introduction of strain compensation within the structure to prevent relaxation and the formation of defects in the grown material [27].

The shift in QW emission wavelength at the centre of each of the SAG features was determined by μ-PL measurements made at a temperature of 298 K. Excitation

was achieved using a 532 nm green laser focused to a spot on the wafer surface approximately 10 μm in diameter. The spot size, which is the smallest possible for the system used, was chosen to limit the potential spectral broadening associated with spatially varying material, and to allow for reasonable spatial resolution and sampling size during 2D mapping, for which the step size was also set at 10 μm. The resolution of the spectrometer used was 0.5 nm, giving an uncertainty in peak wavelength of ± 1nm; this value is used as the acceptance condition when defining the uniformity of material in the final stage of the 2D analysis. The thickness of the selectively grown material was determined by WLI measurements using a Bruker Contour Optical Profilometer. The vertical and lateral resolution of measurements is approximately 5 nm and 50 nm, respectively [15]. Prior to measurements, the SiO_2 mask was removed from the sample surface using a 10:1 buffered HF wet etch solution to provide access to the original wafer surface as a reference point. Whilst the composition of epitaxially grown material can usually be determined using X-ray diffraction measurements, the spot size and spatial resolution required of the analysis of selectively grown material is more than an order of magnitude smaller than that available in lab-based diffractometers [28]. In the absence of high-resolution facilities, the indium composition of the materials described here were determined by comparing the measured QW emission wavelengths with those calculated using LaserMod simulation software [29], with the measured emission wavelengths and QW thicknesses used as input parameters.

5.4. MQW Characterisation

In order to determine the range of emission wavelength shifts and GREs that can be realised using large area SAG features, point analysis was initially conducted at each of the 25 growth sites. The emission wavelengths of the selectively grown MQW material were measured at the centre point of the SAG windows at room temperature. Representative PL spectra for three features with window width, Λ = 200 μm and mask widths, W = 200, 250, and 300 μm are shown in Figure 5.3. In each case, the measured wavelength is longer than the 945 nm emission of the nominal epi structure in the field far from the SAG mask, and increases from 985 nm (orange) to 991 nm (blue) and 994 nm (green) with increasing mask width. The observed red shift in peak wavelength is in line with the enhanced quantum well thickness expected for a relative increase in mask area. As the mask width increases, a larger gradient in reactant concentration is established above the SAG window, driving a larger growth rate enhancement [30]. The spectra, which are broadly representative of those collected from all growth sites, display small full-width-half-maximum (FWHM) values between 14 – 19 nm) indicating that the material at the centre of each of the features is of good quality and suggesting that there has been little degradation of the interfaces between the layers of the MQW structure [27].

The central peak emission wavelengths from all SAG features are shown in Figure 5.4, plotted as a function of both W and Λ. In all cases, the measured wavelength is longer than 945 nm, indicating that a GRE is present even for the largest of the window widths. The red-shift is smallest for the SAG regions with Λ = 300 μm and W = 100 μm which exhibits 954 nm emission, and largest for Λ = 100 μm and W = 300 μm, where emission is at 1031 nm. This represents a total wavelength

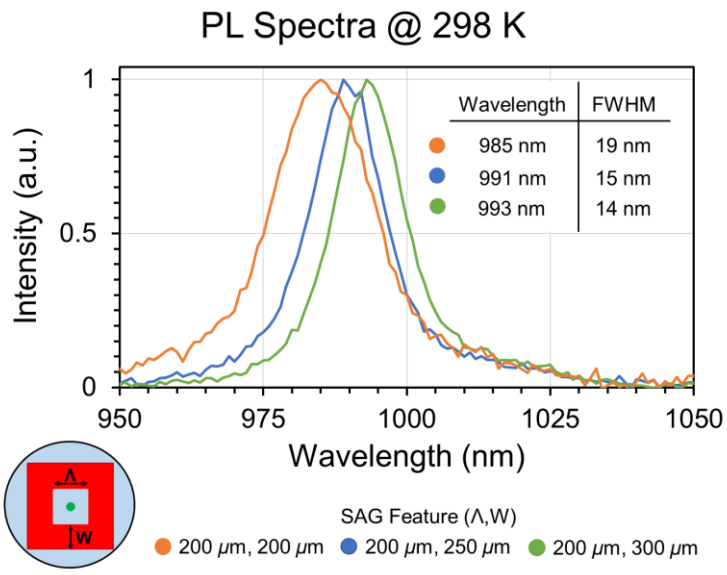

Figure 5.3. Room-temperature PL spectra from the centre point of three SAG features with a common window width, Λ = 200 μm and mask widths, W = 200 μm (orange), 250 μm (blue), 300 μm (green). A red-shift to a longer peak wavelength is observed with increasing W. The low full width max maximum (FWHM) values indicate good-quality growth was achieved in each case.

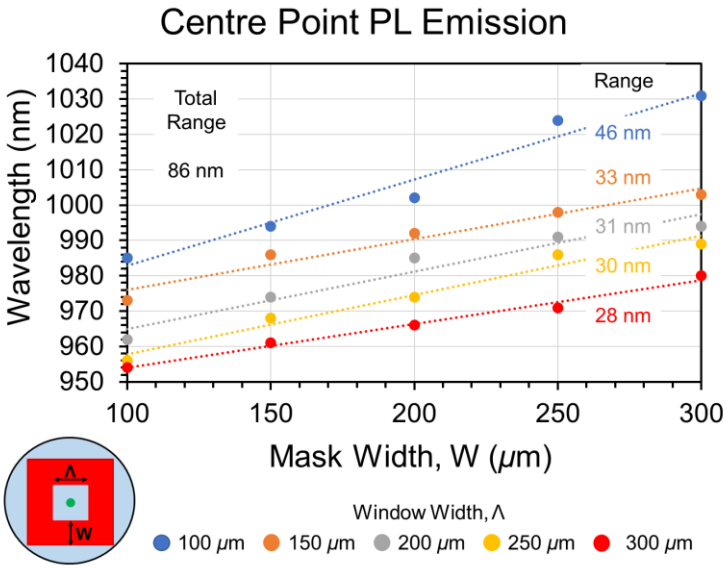

Figure 5.4. Peak room-temperature PL emission wavelength at the centre point of each SAG feature. A wavelength tuning range of 86 nm is achieved across all features relative to the nominal 945 nm emission of the material in the field far from the SAG mask. The degree of red-shifting increases as the mask-to-window area ratio increases.

tuning range of 86 nm across the wafer, relative to the nominal MQW structure in the unmasked region. Two trends are observed with regards to the extent of the shift. Firstly, for a given mask width, W, the emission wavelength increases with decreasing window width, Λ. Second, for a given window width, Λ, wavelength increases with increasing mask width, W. Both of these trends are consistent with the larger GRE expected for increasing values of mask-to-window width ratio (W/Λ), and the larger concentration gradients that result [25]. Considering the latter trend, the wavelength tuning ranges for individual mask widths lie between 26 – 46 nm. Whilst modest, tuning ranges on this order are broadly comparable with those reported in the literature for InGaAs/GaAs QW SAG when the small ratios of W/Λ used in our case ($0.33 \leq W/\Lambda \leq 3$) are considered [17,31].

In order to determine the extent of the GRE associated with the large SAG feature dimensions, the thickness profiles of the deposited material within the windows were mapped using WLI. Representative line profiles taken along the x direction of three features with window width, Λ = 200 μm and mask widths, W = 200, 250, and 300 μm are shown in Figure 5.5. The thickness values are given in terms of an enhancement factor which is simply the ratio of the measured thickness of the entire structure to the nominal 308 nm thickness for the as-grown material. The observed profiles are characteristic of those obtained during SAG, with the lateral gradients in reactant concentrations produced across the window region giving rise to a concave profile, with the GRE being largest directly adjacent to the dielectric mask and decreasing towards the centre of the window [30]. The centre point enhancement factors for these features lie between 1.5 – 1.9 x, with the value increasing with increasing mask width, in line with previously reported trends [13].

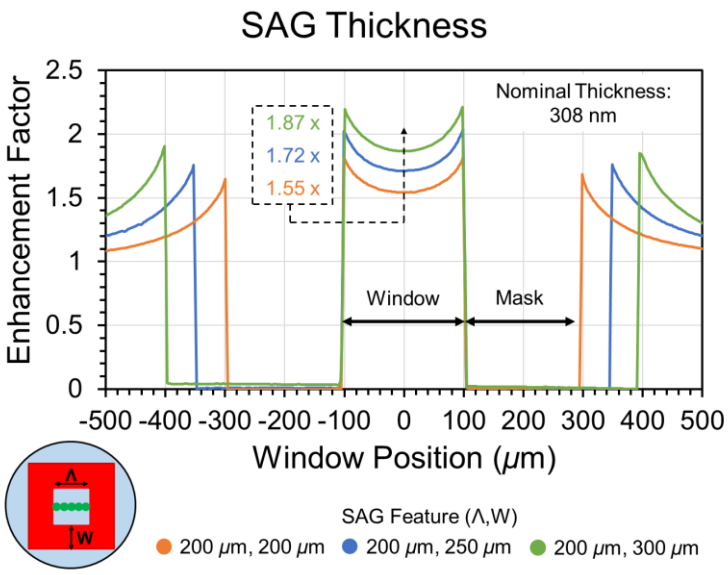

Figure 5.5. Thickness profiles of three SAG features with a common window width, Λ = 200 μm and mask widths, W = 200 μm (orange), 250 μm (blue), 300 μm (green), as determined by WLI profiling. Thickness values are presented as enhancement factors relative to the nominal epi thickness of 308 nm. The centre point thickness increases with increasing mask width.

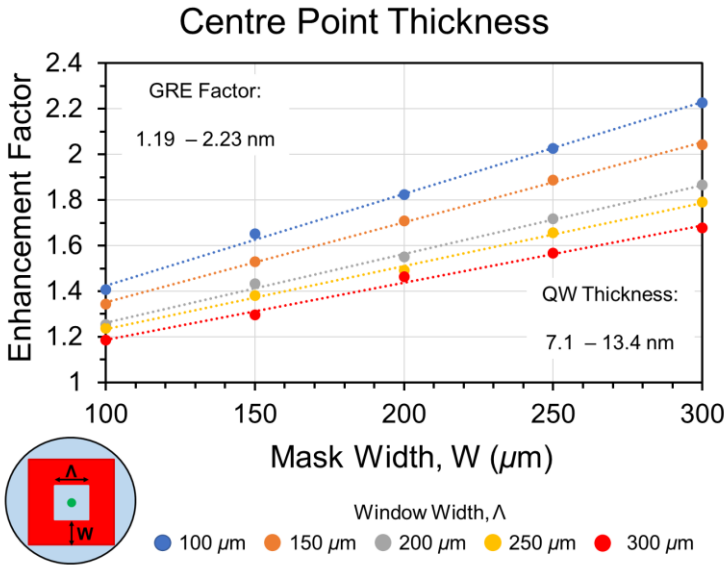

Figure 5.6. Measured growth rate enhancement factors at the centre point of each of the SAG features. A range of enhancement factors from 1.19 – 2.23 x are observed, corresponding to QW thicknesses of 7.1 – 13.4 nm. The thickness enhancement increases as the mask-to-window area ratio increases.

The thickness profile along the y direction of the windows (which, for clarity, are not shown) are essentially identical to those of the x scan in both shape and magnitude of the recorded enhancement factors, suggesting that any anisotropy in growth kinetics associated with alignment of the SAG mask along orthogonal crystal plane directions are minimal over the large distances employed here.

The centre point GRE factors from all SAG features are shown in Figure 5.6, plotted as a function of both W and Λ. As with the shift in emission wavelength described above, the thickness of the selectively grown material increases with increasing W/Λ, with enhancement factors spanning a range from 1.19 – 2.23 times the nominal thickness, values that are typical of those obtained during SAG of InGaAs/GaAs structures [13]. As GaAs is the dominant constituent component of the deposited epi layers (high Ga composition alloys $In_{0.12}Ga_{0.88}As$ and $Al_{0.3}Ga_{0.7}As$ were used), and Ga has the longest vapour phase diffusion length of the group-III species, it is assumed that the thicknesses of the individual layers are uniformly enhanced [26]. Consequently, a corresponding range of modified QW thicknesses of 7.1 nm to 13.4 nm is obtained.

In order to determine the extent to which the observed shifts in PL wavelength are driven by the GRE, simulations of emission wavelength were performed for $In_{0.12}Ga_{0.88}As$/GaAs QWs with the enhanced thicknesses determined above. The calculated wavelengths are shown in Figure 5.7. As expected, the increased QW thickness results in a lengthening of the emission wavelength relative to the nominal structure. However, the degree of red-shifting is significantly truncated compared to the measured centre point wavelengths described in Figure 5.4, with the total tuning range for the calculated values being only 32 nm, compared with the 86 nm observed

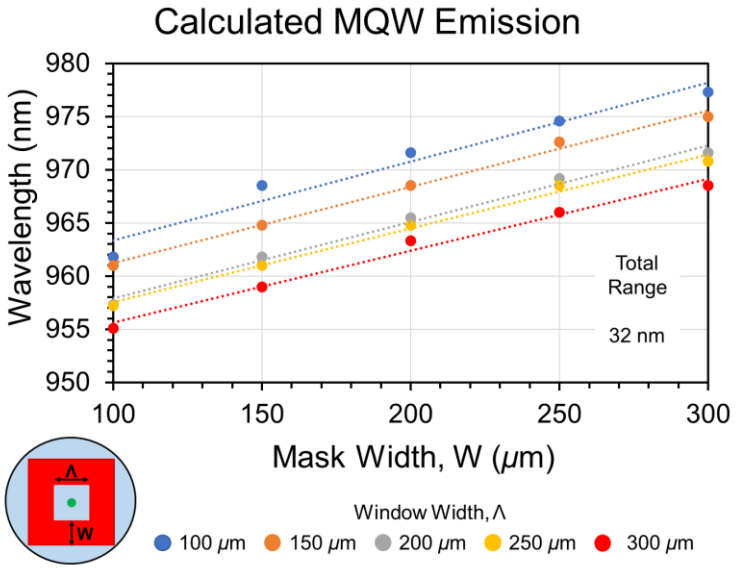

Figure 5.7. Calculated emission wavelengths of $In_{0.12}Ga_{0.88}As$ quantum wells simulated using the enhanced thickness values determined by WLI profiling. A large difference between calculated values and those observed in PL measurements of the selectively grown material, with a total tuning range of only 32 nm observed for calculated values.

in reality. The difference between the calculated and observed wavelength increased significantly as the W/Λ ratio of the features increases. For the smallest values of W/Λ (Λ = 300 μm, W = 100 μm and Λ = 250 μm, W = 100 μm) the wavelengths differ by less than 1 nm (within the error of the PL measurement), whilst for largest W/Λ features (Λ = 100 μm, W = 250, 300 μm) the enhanced QW thickness accounts for only 38 % of the observed red-shift. This result suggests that a higher indium composition is required in the QW to completely account for the measured wavelength enhancement, and that the indium mole fraction increases significantly compared to the nominal 12 % value as the W/Λ ratio of the SAG features increases.

The necessary indium compositions were determined by modifying the above simulations to allow for an indium variation such that the emission wavelengths

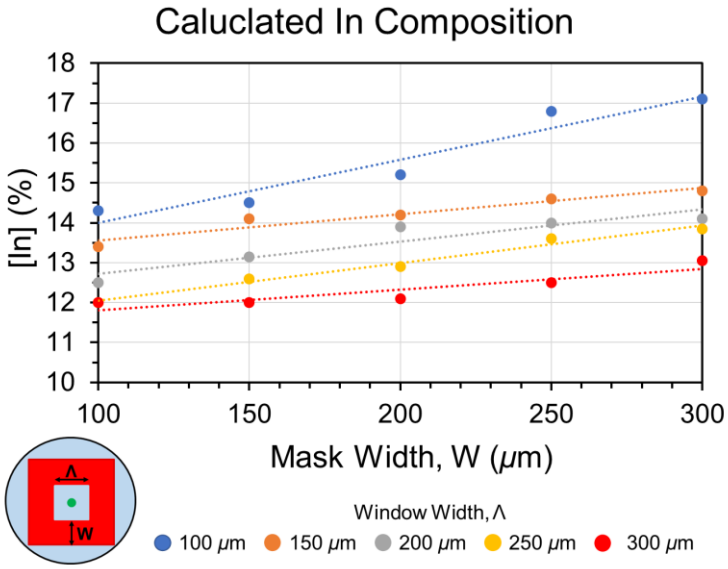

Figure 5.8. Calculated indium compositions at the centre of each SAG feature. Values were determined by simulation of InGaAs QW with enhanced thicknesses, determined above. The indium compositions are those required to obtain the same wavelength observed in centre point PL measurements. A range of compositions from 12 – 17 % are obtained, increasing with W/Λ ratio.

match those measured by PL. The calculated indium compositions are shown in Figure 5.8, plotted as a function of both W and Λ. For the features with the smallest W/Λ ratio, the composition is virtually unchanged from the nominal 12 % value, confirming that wavelength shift in this case is derived entirely from the QW thickness enhancement. As indicated by the trends in Figure 5.7, the indium percentage increases significantly up to 17% for the features with the largest W/Λ ratio, where it accounts for a larger fraction of the observed red-shift. A higher indium composition is expected for these features as the large lateral gradient in reactant concentrations between the window and mask regions enhances the diffusion of indium towards the centre of the window [10,15]. Where the values of W and Λ are both very large (and W/Λ is approximately 1), the relative concentration gradients

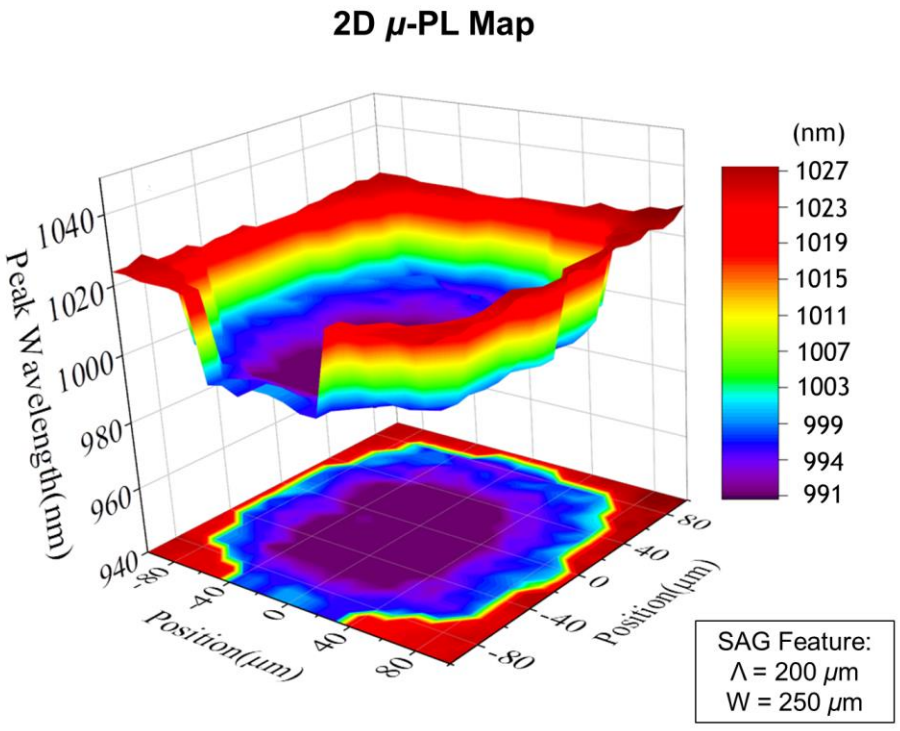

Figure 5.9. 2D μ-PL map for the SAG feature with Λ = 200 μm and W = 250 μm. The wavelength distribution across the growth window is parabolic, with the wavelength increasing concentrically from the centre point to the edge of the dielectric mask. An approximately 80 x 80 μm^2 region of material with uniform emission wavelength is observed at the centre of the window.

are smaller which, when combined with the finite diffusion length of In, results in a lower indium composition at the centre point [22].

For selected SAG features, the point analysis performed above was extended to cover the entire growth window in order to assess the uniformity of the selectively grown material. A representative 2D μ-PL map for the SAG feature with Λ = 200 μm, W = 250 μm is shown in Figure 5.9. The wavelength distribution across the window is characterised by a large central area in which the wavelength is relatively uniform, surrounded by concentric regions of material with longer wavelengths, increasing significantly towards the edge of the dielectric mask. This distribution is equivalent

to that seen for conventional 1D SAG and is explained by the lateral concentration gradients that are established above the growth window [25,30]. In addition to the concave thickness profile discussed previously, the concentration gradient gives rise to an anisotropy in the indium composition due to the limited diffusion length of reactant In-species which originate from the region directly above the mask, resulting in a greatly enhanced indium composition within a few tens of microns from the mask edge compared with the centre of the window [15,22].

The range of the wavelength and indium composition distributions across the window are visualised in the line scans shown in Figure 5.10. As before, the indium composition at each point (bottom panel) was calculate by QW simulations created using the enhance well thickness determined by WLI measurements (middle panel) and the emission wavelengths extracted from the PL map (top panel). With regard to the variation in indium composition, a value of 14.2% is calculated for the material at the centre point. The composition increases gradually within 0.5% of this value across the majority of the growth window, covering an area of approximately 160 μm (as highlighted by the orange box). Beyond this, the indium composition increases significantly, rising to 16.9% at the boundary of the dielectric mask. This result suggests that the lateral concentration gradient driving the indium variation is dominated by species arriving at the window from directly above the mask, within approximately 20 μm of its edge, and that the indium enhancement across the majority of the window is determined primarily by vapour phase diffusion of species from higher up in the boundary layer. This is in reasonable agreement with a gas phase diffusion length for indium on the order of 30 μm as determined by modelling of the AlGaInAs/InP system [15,26].

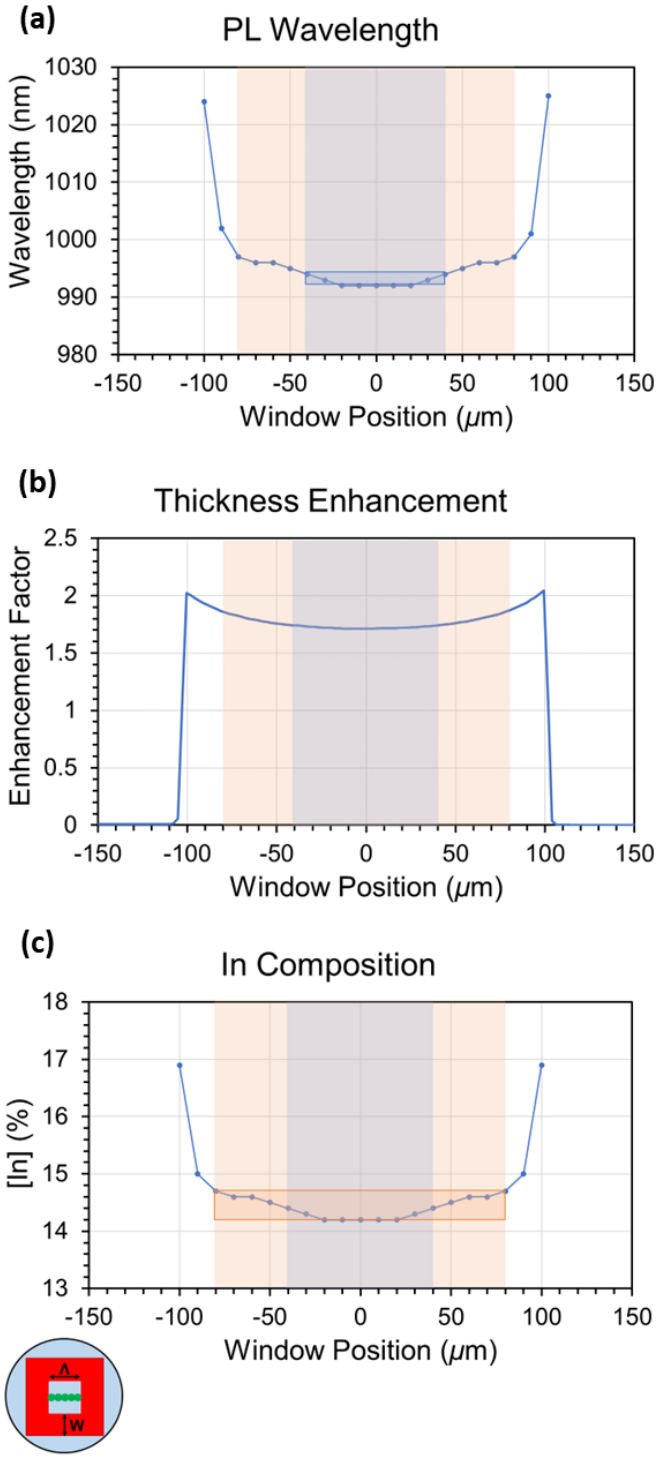

Figure 5.10. Extended 2D analysis for feature with Λ = 200 μm and W = 250 μm. Line scans of the (a) emission wavelength, (b) thickness enhancement, and (c) indium composition across the SAG window. Wavelength and indium values were determined from 2D μ-PL mapping. The area with uniform emission, within 2 nm of the centre point value, is highlighted in blue. The area in which the indium composition varies within 0.5 % is highlighted in orange.

The wavelength variation across the window follows a similar trend to that of the indium composition, with a longer wavelength of 1024 nm observed at the edge of the mask compared with the 991 nm centre point, driven by the large inhomogeneity in the indium mole fraction. In defining an area in which the emission wavelength is deemed to be uniform, a constraint of ± 2 nm relative to the centre point wavelength is used – this value is chosen to allow a conservative limit of ± 1 nm variation on top of the ± 1 nm uncertainty arising from the wavelength resolution of the PL measurement. The width of the uniform emission area (which is highlighted in blue) is determined to be approximately 80 μm, with an uncertainty of ± 5 μm originating from the choice of laser spot and step size used during PL mapping. Line scans taken along the orthogonal axis of the growth window (which, for clarity, are not shown here) show little variation in terms of measured wavelength values and calculated indium compositions, or in the width of the uniform emission region, suggesting that growth within the large 2D windows is not significantly affected by any natural anisotropies in growth kinetics. It is noted that the total wavelength variation across the 160 μm region identified above (orange box) is limited to only 6 nm, suggesting that the area of the uniform emission can be expanded by re-evaluating the growth conditions used to enhance the diffusion of species within the window and flatten the wavelength distribution.

Similar analysis was performed for five additional features, the results of which are summarised in Figure 5.11. In general, two trends are observed with regards to the width of the uniform emission area. Firstly, for a fixed W, the width of the area increases as Λ increases, whilst the wavelength decreases. Secondly, for a fixed Λ, both the width of the area and the wavelength increase with W. Significantly, two

features (Λ = 200 μm, W = 300 μm and Λ = 250 μm, W = 300 μm) are identified for which the uniform emission area exceeds 100 x 100 μm^2, approaching the minimum scale required for the fabrication of PCSELs. It is worth noting that in terms of operation, the gain bandwidth of the active element is expected to be much larger (> 30 nm) than these values of wavelength change (± 2 nm), resulting in spatially varying (de-)tuning of the laser wavelength to the gain peak. From the line-scans in 6(a) we expect lasing to be supported in the whole area of the SAG mask, with the possible exception of the approximately 20 μm wide perimeter at the boundary of the aperture and SAG mask.

Uniform Emission Area

Λ (μm)	W (μm)	λ (nm)	$W_{uniform}$ (μm)
100	250	1024	40
150	250	998	60
200	200	985	60
200	250	991	80
200	300	994	100
250	300	989	110
		[± 2 nm]	[± 5 μm]

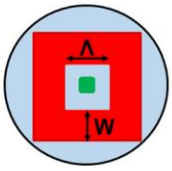

Figure 5.11. Table showing the width of the uniform emission area for selected SAG features, as determined by 2D analysis. The uniform area was defined such that the wavelength varied within ± 2 nm of the centre point wavelength. The width of the uniform area, $W_{Uniform}$, is accurate to within ± 5 μm.

5.5. Discussion & Future Work

Whilst the 2D analysis of the selectively grown material presented above is incomplete, having been extended to only six of the 25 features, the data presented allows us to make a number of conclusions about the suitability of SAG as a technique for achieving multicolour PCSEL arrays. Firstly, it is clear from the centre point μ-PL and WLI measurements that the GRE and wavelength red-shifting associated with SAG is indeed effective for features with window widths, Λ, on the order of 300 x 300 μm^2. Whilst the typical 30 nm tuning range observed for features with $\Lambda > 100$ μm is modest in comparison to those values reported for small area 1D mask geometries [17,31], it is expected that the wavelength range can be expanded by increasing the mask widths, W, employed thereby accessing features with larger W/Λ ratios [10]. Secondly, 2D analysis for two of the six features studied indicates that the uniform emission areas at the centre of the growth windows can reach 100 x 100 μm^2 or more, satisfying the lower limit for the area required by PCSELs. From these results it is reasonable to conclude that SAG does have the potential to enable multi-wavelength arrays, and that future work should be undertaken with regards to optimisation of mask geometries and process conditions in order to obtain ideal material for device fabrication.

The most immediate piece of future work in this regard would be to extend the 2D characterisation to all of the features presented in this study. Whilst this would provide a fuller picture of the dynamics of selective growth in these large features, it is noted that trends in the data in Figure 5.11. suggest that only features with $\Lambda >$ 250 μm are likely to extend the uniform emission area beyond the 100 x 100 μm^2

recorded here – and that this would require mask widths on the order of 250 μm or more.

The challenge for selectively grown PCSELs going forward will be the simultaneous optimisation of both large uniform emission areas and sufficiently wide on-wafer wavelength ranges (> 40 nm) to allow for practical arrays. Here we note that the method of PC detuning discussed in Section 5.1. would still be applicable to selectively grown material and so an on-wafer variation on the order of 100 nm may not be strictly required to achieve an array with a tuning bandwidth on this order [6]. Taking the above observations into account, a future study focusing on the optimisation of SAG mask geometry should investigate features with Λ = 200 – 400 μm and W = 300 – 500 μm using the same matrix layout described in this study. The largest of the SAG features in this case would occupy a total edge-to-edge (chip) area of 1400 μm, which represents the maximum feature size that can be accommodated whilst maintaining a 2 mm centre-to-centre separation with reasonable dielectric separation (approximately 600 μm). Ultimately, it may prove that the practicality of achieving a wide-tuning range multicolour PCSEL array may be fundamentally limited by the extremely large, mm-scale feature areas required and the limits this imposes on the density of devices on a single wafer.

An alternative approach for increasing the size of the uniform emission area in the SAG features presented in this study may be to reassess the growth conditions used [9,10,22]. In particular, the use of a higher growth temperature (up to 680 °C) or a reduction in the nominal growth rate should result in both increased vapour phase and surface diffusion lengths, and may promote a flattening of the indium composition profile across the SAG window - with reference to Figure 5.10., this

would equate to an expansion of the width of the blue region (2 nm variation) into the orange region (0.5% indium / 6 nm variation).

Ultimately, a full understanding of the growth dynamics at play in the large area 2D features discussed here, and the ability to accurately predict the wavelength and uniformity of material for a given mask geometry, will require the development of a computation model such as those available for small area 1D SAG [9,10,15,22,26]. As briefly outlined in Section 5.2., such a model requires knowledge of empirically derived reaction parameters (such as effective gas phase diffusion constants) which must be determined by studying the growth behaviour of the binary components of the InGaAs alloy, GaAs and InAs, over the same SAG features. Whilst the extension of the existing 1D models to account for the more complex 2D geometry of PCSELs appears to be a non-trivial task, a working predictive model would be invaluable in the development of multicolour arrays, allowing for a reduction in the number of experimentally expensive growth studies of optimised mask geometries and growth conditions required to achieve suitable material for device fabrication.

5.6. Conclusion

This chapter has presented a study of InGaAs/GaAs MQW structures selectively grown in large area 2D SAG features chosen to reflect the device geometries of PCSELs. It has been shown that the growth rate enhancement associated with SAG is effective in features with dimensions up to 300 x 300 μm^2, resulting in a total wavelength tuning range of 86 nm across all growth sites, with respect to the nominal epi structure. For a given window width, the degree of red-shifting increases with

dielectric mask width, producing a typical tuning range on the order of 30 nm. For features with the largest ratio of mask-to-window area, the wavelength shift is dominated by a greatly enhanced QW indium mole fraction up to 17% at the centre of the growth window, whilst the composition varies little from the nominal 12% where W/Λ is small. 2D analysis of selected features reveals that the wavelength distribution across the growth windows is characterised by a large central region in which the emission wavelength is uniform within 2 nm. Regions of isotropic gain material with areas up to 100 x 100 μm^2 have been demonstrated, indicating that SAG may be a suitable technique for the realisation of monolithic multicolour PCSEL arrays in the future.

5.7. References

[1] K. Hirose, Y. Liang, Y. Kurosaka, A. Watanabe, T. Sugiyama, and S. Noda, "Watt-class high-power, high-beam-quality photonic-crystal lasers", Nature Photon., 8, 406 (2014)

[2] Y. Itoh, N. Kono, D. Inoue, N. Fujiwara, M. Ogasawara, K. Fujjii, H. Yoshinaga, H. Yagi, M. Yanagisawa, M. Yoshida, T. Inoue, M. De Zoysa, K. Ishizaki, and S. Noda, "High-power CW oscillation of 1.3-μm wavelength InP-based photonic-crystal surface-emitting lasers", Optics Express, 30(16), 29539 (2022)

[3] R. J. E. Taylor, D. T. D. Childs, P. Ivanov, B. J. Stevens, N. Babazadeh, J. Sarma, S. Khamas, A. J. Crombie, G. Li, G. Ternent, S. Thoms, H. Zhou, and R. A. Hogg, "Coherently coupled photonic-crystal surface emitting laser array", IEEE J. Select. Topics Quant. Electron., 21(6), 4900307, (2015)

[4] R. J. E. Taylor, D. T. D. Childs, P. Ivanov, B. J. Stevens, N. Babazadeh, A. J. Crombie, G. Ternent, S. Thoms, H. Zhou, and R. A. Hogg, “Electronic control of coherence in a two-dimensional array of photonic crystal surface emitting lasers”, Sci. Rep., 5, 13203 (2015)

[5] B. C. King, K. J. Rae, A. F. McKenzie, A. Boldin, D-H. Kim, N. D. Gerrard, G. Li, K. Nishi, K Takemasa, M. Sugawara, R. J. E. Taylor, D. T. D. Childs, and R. A. Hogg, “Coherent power scaling in photonic crystal surface emitting laser arrays”, AIP Advances, 11, 015017 (2021)

[6] C. Hill, J. R. Orchard, I. Javed, C. W. Munro, D-H. Kim, Z. Bian, A. F. McKenzie, N. D. Gerrard, K. J. Rae, P. Ivanov, R. J. E. Taylor, R. A. Hogg, and D. T. D. Childs, “Monolithic all-semiconductor PCSELs emitting at 1.3 μm”, 27th International Semiconductor Laser Conference, WP3.4, Potsdam, Germany, October 2021

[7] K. Ishizaki, M. De Zoysa, and S. Noda, “Progress in photonic-crystal surface-emitting lasers”, Photonics, 6, 96 (2019)

[8] D. J. Klotzkin, Introduction to Semiconductor Lasers for Optical Communications, New York, NY, USA: Springer (2014)

[9] P. D. Dapkus, C. Y. Chi, S. J. Choi, H. J. Chu, M. Dreiske, R. Li, Y. Lin, Y. Nakajima, D. Ren, R. Stevenson, M. Yao, T. W. Yeh, and H. Zhao, “Selective area epitaxy by metalorganic chemical vapor deposition – a too for photonic integration and novel nanostructure integration”, Prog. Quant. Electron., 75, 100304 (2021)

[10] J. J. Coleman, R. M. Lammert, M. L. Osowski, and A. M. Jones, “Progress in InGaAs-GaAs selective area MOCVD towards photonic integrated circuits”, IEEE J. Select. Topics Quant. Electron., 3(3), 874 (1997)

[11] T. M. Cockerill., R. M. Lammert, D. V. Forbes, M. L. Osowski, and J. J. Colman, “Twelve-channel strained-layer InGaAs-GaAs-AlGaAs buried heterostructure quantum well laser array for WDM applications by selective-area MOCVD”, IEEE Photon. Technol., 6(7), 786 (1994)

[12] C. Besancon, D. Néel, D. Make, J. M. Ramirez, G. Cerulo, N. Vaissiere, D. Bitauld, F. Pommereau, F. Fournel, G. Dupré, H. Mehdi, F. Bassani, and J. Decobert, “AlGaInAs multi-quantum well lasers in silicon-on-insulator photonic integrated circuits based on InP-seed-bonding and epitaxial regrowth”, Appl. Sci., 12, 263 (2022)

[13] T. M. Cockerill, D. V. Forbes, J. A. Dantzig, and J. J. Coleman, “Strained-layer InGaAs-GaAs-AlGaAs buried-heterostructure quantum-well lasers by three-step selective-area metalorganic chemical vapor deposition”, IEEE J. Quant. Electron., 30(2), 441 (1994)

[14] M. Aoki, M. Suzuki, H. Sano, T. Kawano, T. Iddo, T. Taniwatarai, K. Uomi, and A. Takai, “InGaAs/InGaAsP MQW electroabsorption modulator integrated with a DFB laser fabricated by bang-gap energy control selective area MOCVD”, IEEE J. Quant. Electron., 29(6), 2088 (1993)

[15] J. Decobert, G. Binet, A. D. B. Maia, P-Y. Lagrée, and C. Kazmierski, “AlGaInAs MOVPE selective area growth for integrated circuits”, Adv. Opt, Technol., 4(2), 167 (2015)

[16] V. Shamakhov, D. Nikolaev, S. Slipchenko, E. Fomin, A. Smimov, I. Eliseyev, N. Pikhtin, and P. Kop'ev, "Surface nanostructuuting during selective area epitaxy of heterostructures with InGaAs QWs in the ultra-wide windows", Nanomaterials, 11, 11 (2021)

[17] T. M. Cockerill., D. V. Forbes, H. Han, B. A. Turkot, J. A. Dantzig, I. M. Robertson, and J. J. Colman, "Wavelength tuning in strained layer InGaAs-GaAs-AlGaAs quantum well laser by selective-area MOCVD", J. Electron. Mater., 23(2), 115 (1994)

[18] O. K. Kwon, Y. A. Leek, C. W. Lee, K. S. Kim, H. M. Park, and E. S. Nam, "Simple technique for evaluating dimensional and compositional changed in selective-area-grown MQW laser diodes", Optics Express, 22(19), 23694 (2014)

[19] K. Kumakura, K. Nakakoshi, M. Kishida, J. Motohisa, T. Fukui, and H. Hasegawa, "Dynamics of selective metalorganic vapour phase epitaxy growth for GaAs/AlGaAs micro-pyramids", J. Cryst. Growth, 145, 308 (1994)

[20] F. Schuster, J. Kapraub, G. N. Malheiros-Silveira, A. Deshpande, and C. J. Chang-Hasnain, "Site-controlled growth of monolithic InGaAs/InP quantum well nanopillar lasers on silicon", Nano Lett., 17, 2687 (2017)

[21] G. J. Bauhuis, P. Mulder, and H. van Kempen, "Tip formation of micrometer scale GaAs pyramid structures grown by MOCVD", J. Cryst. Growth., 240, 104 (2002)

[22] A. M. Jones, M. L. Osowski, R. M. Lammert, J. A. Dantzig, and J. J. Colman, "Growth, characterisation, and modelling of ternary InGaAs-GaAs quantum

weels by selective-area metalorganic chemical vapour deposition", J. Electron Mater., 26(11), 1631 (1995)

[23] B. Korgel and R. F. Hicks, "A diffusion model for selective-area epitaxy by metalorganic chemical vapor deposition", J. Cryst. Growth, 151, 204 (1995)

[24] A. R. Clawson, C. M. Hanson, and T. T. Vu, "MOVPE growth of SiO2-masked InP structures at reduced pressures", J. Cryst. Growth, 77, 334 (1986)

[25] M. Gibbon, J. P. Stagg, C. G. Cureton, E. J. Thrush, C. J. Jones, R. E. Mallard, R. E. Pritchard, N. Collis, and A. Chew, "Selective-area low-pressure MOCVD of GaInAsP and related materials on planar InP substrates", Semicond. Sci. Technol., 8, 998 (1993)

[26] N. Dupuis, J. Décobert, P-Y. Lagrée, N. Lagay, F. Poingt, C. Kazmierski, A. Ramdane, and A. Ougazaden, "Mask pattern interference in AlGaInAs selective area metal-organic vapor-phase epitaxy: experimental and modelling analysis", J. Appl. Phys., 103, 113113 (2008)

[27] J. E. Ayers, Heteroepitaxy of Semiconductors: Theory, Growth, and Characterisation. Boca Raton, FL, USA: CRC Press (2007)

[28] J. Décobert, R. Guillamet, C. Mocuta, G. Carbone, H. Guerault, "Structural characterisation of selectively grown multilayers with new high angular resolution and sub-millimeter spot-size x-ray diffractometer", J. Cryst. Growth, 370, 154 (2013)

[29] LaserMOD™ Simulation Software Webpage: https://www.synopsys.com/photonic-solutions/rsoft-photonic-device-tools/active-device-lasermod.html

[30] E. J. Thrush, J. P. Stagg, M. A. Gibbon, R. E. Mallard, B. Hamilton, J. M. Jowett, and E. M. Allen, “Selective and non-planar epitaxy of InP/GaInAs(P) by MOCVD”, Mater. Sci. Eng., 21(2), 130 (1993)

[31] T. M. Cockerill, D. V. Forbes, H. Han, and J. J. Coleman, “Monolithic Integration of a strained-layer InGaAs-GaAs-AlGaAs quantum-well laser with a passive waveguide by selective-area MOCVD”, IEEE Photon. Technol. Lett., 4(4), 448 (1993)

Chapter 6 |

Conclusion

In this thesis, a number of studies relating to the development of GaAs-based photonic crystal surface emitting lasers (PCSELs) have been presented, with a focus on furthering the understanding of metalorganic vapour phase epitaxy (MOVPE) growth processes in the context of the unique structures and geometries associated with this class of device. The most important of these processes, epitaxial regrowth of the photonic crystal (PC) grating layer, was explored in the experiments described in Chapters 3 & 4. These investigations, respectively, represent the first studies of PCSELs utilising the AlAs-GaAs PC system, and the first to probe the kinetic influences associated with grating infill and void formation in GaAs-based structures more generally. The analyses presented in these studies, which considered the effects of adatom diffusion and crystal planes kinetics, were enabled by the use of superlattice-type structures during regrowth and scanning transmission electron microscope (STEM) imaging, which allowed for the evolution of the growth front during infill to be visualised and the relationship between the underlying grating geometry and that

of the resulting crystallographic voids to be inferred. This proved to be an insightful approach, revealing information that had been unavailable in previous studies of PCSEL regrowth, and represents an important technique for future efforts to optimise void geometries.

The investigation presented in Chapter 3 considered the effects of pre-growth mass transport of material has upon the profile of the PC grating pits, and its subsequent impact on the formation of voids during regrowth. By varying the temperature ramp time prior to deposition, it was shown that the extent of mass transport and the morphology of the grating pits can be controlled, with a short ramp time necessary to retain the as-etched $\{111\}$ sidewall planes of the initial pits. Longer ramp times resulted in more extensive diffusion of material accompanied by surface restructuring and the introduction of high-Miller index $\{311\}$ planes as part of a theoretically predicted free-energy minimisation pathway. This raises the interesting possibility of *in-situ* modification of the grating as an additional degree of freedom in future PCSEL design.

The two distinct grating profiles were shown to give rise to unique void geometries, the size and shape of which were directly related to the growth kinetics of the crystal planes present in the growth front, with high growth rate $\{311\}$ planes resulting in much smaller voids than those achieved with the as-etched pit design. Ultimately, it was shown that void formation in PCSELs is the result of self-shadowing effects and the low surface mobility of adatoms in the system, which lead to a reduced growth rate on the surfaces at the bottom of the pit and rapid lateral growth of the upper (100) surface across the pit opening.

The studies described in Chapter 4 can be thought of as an extension of the analysis outlined in the previous chapter, with the focus on the factors impacting the extent of grating infill and the symmetry of voids. The role of adatom surface mobility on void formation was explored by leveraging the inherent mobility associated with different infill layer compositions, with the degree of infilling of the grating pits increasing as the composition was graded from AlAs to GaAs through an intermediate AlGaAs alloy across different samples. The range of void geometries observed suggest that there is a large tuning window in the AlGaAs/GaAs PC system, and that optimised void size engineering (including all-semiconductor infilling) may be achieved in the future by controlling adatom diffusion lengths through optimisation of regrowth conditions.

By extending STEM analysis to both axes of the PC it was shown that kinetic anisotropies associated with the *A*- or *B*-type polarity of high-Miller index crystal planes in the III-V material system resulted in in-plane asymmetry in void shape, a phenomenon that is as yet unreported for PCSELs utilising circular grating pits. Importantly, the emergence of (what can be quite complex) asymmetries in the void shape from a symmetric pit shape provides an additional route for optimised PCSEL design without the need for pits with reduced in-plane asymmetry (such as triangles). The concept of introducing void shape asymmetry was explored further by comparing PC structures fabricated on $(311)B$ orientated substrates with those on conventional (100) wafers discussed above. In addition to a greatly enhanced in-plane asymmetry, voids on the high-index substrate display a high-degree of out-of-plane asymmetry attributed to the reduced crystal symmetry of the $(311)B$ orientation, suggesting that devices on such substrates may benefit from more optimal out-coupling of light.

Finally, in addition to grating regrowth, selective area growth (SAG) of InGaAs/GaAs muti-quantum well (MQW) structures was discussed in Chapter 5. To the best of the authors knowledge, this represents the first instance of SAG being expended to large two-dimensional features with dimension up to 300 x 300 μm^2, and is the first report of SAG being applied in the context of PCSELs. Through centre point analysis of the QW thickness and emission wavelength of selectively grown material in masked regions with dimension between 100 – 300 μm, it was shown that the growth rate enhancement associated with SAG is indeed effective for these very large features. Extended two-dimensional analysis across the entire growth window for selected features revealed that large areas with uniform emission wavelengths up to 100 x 100 μm^2 can be achieved, suggesting that SAG may be a suitable technique for realising multicolour PCSEL arrays in the future.

The results and conclusions presented in this thesis highlight a number of possible directions for future work relating to the application of MOVPE-based processes to the fabrication of PCSELs. In the pursuit of optimised epitaxial regrowth and void-shape engineering for GaAs-based devices, the use of AlGaAs as an infill material represents the most promising system for achieving ideal PC void geometries. In this regard, and considering the impact of adatom surface mobility on the extent of pit infilling during regrowth, the effect of two parameters should be investigated further. Firstly, the impact of the aluminium composition of the AlGaAs layer may be explored by considering the change in key void dimensions with varying Al-mole fraction (which tunes the inherent mobility of adatoms in the system). Secondly, the effect of different growth conditions should by investigated, with particular interest being paid to the role of growth temperature in tuning the extent of infilling (for

which the usable process range is expected to be in the range of 600 – 670 °C), as well as secondary conditions such as growth rate and V/III ratio.

More broadly, additional work is required to expand understanding of void formation and void-shape asymmetry in different PC systems. To this end, the development of a computation model capable of simulating the regrowth process in PCSELs would be invaluable in designing optimised void geometries and reducing the number of costly regrowth experiments. Ideally, such a model would be able to predict void geometries obtained from grating pits of arbitrary shape and dimensions given a set of growth conditions. Initially, such models would need to be trained using data from real world data from which the necessary kinetic parameters can be derived. The experiments outlined above may potentially provide much of this information, however they should be extended to include additional pit shapes (such as triangles or one-dimensional trenches) in order to provide a more complete picture.

Finally, with regards to the optimisation of a SAG process for PCSELs, and the fabrication of devices using this approach, two further growth studies are proposed. Initially, the wavelength tuning range and material uniformity should be examined for SAG features with larger dimensions more suited for device applications (e.g. window width, Λ = 200 – 400 μm and mask width, W = 300 – 500 μm). Following this, the impact of growth conditions, particularly the use of higher growth temperatures and lower growth rate, on the selective wavelength enhancement should be examine with the aim of identifying a set of conditions for which both the wavelength tuning range and area of uniform-wavelength material is maximised for a given feature size.